ALMA MATER STUDIORUM
UNIVERSITÀ DI BOLOGNA

DOTTORATO DI RICERCA IN

INGEGNERIA ELETTRONICA, TELECOMUNICAZIONI E TECNOLOGIE DELL'INFORMAZIONE

Ciclo 37

Settore Concorsuale: 09/F1 - CAMPI ELETTROMAGNETICI

Settore Scientifico Disciplinare: ING-INF/02 - CAMPI ELETTROMAGNETICI

NONLINEAR MODELLING OF RADIOFREQUENCY DEVICES FOR RECONFIGURABLE AND SENSING APPLICATIONS

Presentata da: Simone Trovarello

Coordinatore Dottorato

Davide Dardari

Supervisore

Alessandra Costanzo

Co-supervisore

Giacomo Paolini

Esame finale anno 2025

Index

Abstract

Radiofrequency (RF) technologies have tremendously evolved in a bid to answer the ever-increasing demand for flexibility and efficiency of communication systems. In that respect, reconfigurability within a system plays the key role of dynamic adjustment to changing operation conditions: frequency bands, modulation schemes, and power levels. Reconfigurable RF systems are going to be fundamental in handling the challenges thrown up by modern communication networks, which include increasing data rate while improving spectrum efficiency and reducing energy consumption. Among the advanced materials that promise to provide RF reconfigurability are ferroelectric materials. In particular, a focus on the nonlinear modeling of Hafnium-Zirconium-Oxide-based (HfZrO) devices is presented, with particular attention to passive phase shifters. Moreover, the integration of HfZrO with complementary metal-oxide-semiconductor (CMOS) technology opens up a new generation of reconfigurable RF circuits.

In this context, a new silicon-integrated technology for antenna realization and their derivative applications, such as RF Energy Harvesting (EH), is presented, focusing on the design and implementation of different rectennas operating at multiple frequencies. The topic of EH is also discussed in the framework of the design and realization of a novel topology for a wide dynamic range of applications.

The need for stand-alone RF systems and circuits is of particular interest to microwave sensing applications. In particular, a focus on biological microwave sensing is presented. Two distinct solutions, for wood moisture content monitoring and skin hydration, are reported. Particular attention is given to a new sensing strategy that avoids the need for external instrumentation by only monitoring the steady-state regime of nonlinear circuits.

Finally, a description of the activities carried out in joint projects with industry is reported, mainly focusing on the design of a novel positioning system for railway transport systems based on Long Range (LoRa) protocol and of a three-antenna system.

List of Abbreviations

Abbreviation	Explanation
ALD	Atomic Layer Deposition
BST	Barium Strontium Titanate
CMOS	Complementary Metal-Oxide-Semiconductor
CPW	Coplanar Waveguide
CSRR	Complementary Split Ring Resonator
ERTMS	European Rail Traffic Management System
FN	False Negative
FP	False Positive
GNSS	Global Navigation Satellite System
HB	Harmonic Balance
HfO_2	Hafnium-oxide
HRSi	High-Resistivity Silicon
HfZrO	Hafnium-Zirconium-Oxide-based
IC	Integrated Circuit
IDC	Interdigitated Capacitor
I_{DS}	Drain-source current
ISM	Industrial, Scientific and Medical
ML	Machine Learning
NL	Nonlinear
LoRa	Long Range
RF	Radiofrequency

RF-EH	RF Energy Harvesting
RIE	Reactive Ion Etching
PCE	Power-Conversion Efficiency
PMU	Power Management Unit
RMSEC	Root Mean Square Error of Calibration
RMSECV	Root Mean Square Error of Cross-Validation
SIMCA	SIMulated Correlation Algorithm
SPDT	Single-Pole Double-Throw
TN	True Negative
TP	True Positive
V_{DS}	Drain-source voltage
V_{GS}	Gate-source voltage
V_{OC}	DC open-circuit voltage
VNA	Vector Network Analyzer
V2X	Vehicle-to-everything
Wi-Max	Worldwide Interoperability for Microwave Access
WSN	Wireless Sensor Network
XRR	X-Ray Reflectivity
ZrO_2	Zirconium-Oxide

Chapter 1

Introduction

In this thesis, the study of different RF circuits and devices operating at microwaves and mmWaves is reported. Given the increasing interest in tunable materials and their applications in RF circuits, the study of ferroelectric-based phase shifters is analyzed. In particular, an in-depth modeling of the HfZrO-based phase shifter is provided, focusing on the nonlinearities of the material and its power-handling capabilities. Given the low-voltage bias required from the nanoscale ferroelectric material and its CMOS compatibility, silicon-integrated rectennas are investigated, operating both in microwaves and mmWaves. For this purpose, a novel design and fabrication technology is proposed, which demonstrates how to overcome the limitations of traditional silicon-integrated antennas. The design is also validated by the realization of several rectennas adopting the novel antenna technology. Given the well-known limitations of rectifiers to operate in wide dynamic range scenarios, a novel topology for EH application is proposed. By adopting multiple rectifiers in cascade topology, the dynamic range of the rectifier is enlarged, making it possible to exploit these circuits in real scenarios, where the incoming power is not predictable. Following the need for stand-alone devices also in biological sensing, two different sensors for medical and agriculture applications are presented. In particular, a skin hydration sensor and a moisture content sensor are designed, and capable of operating in in-vivo and stand-alone conditions. An in-depth study of an external activity carried out with the industry and carried out in collaboration of the research team guided by Prof. Alessandra Costanzo, consisting of a novel system for train location and integrity is also provided. In particular, the design of a multi-antenna system is proposed, capable of connecting both the wagon between each other and intelligent poles positioned alongside the railway.

The proposed devices are validated by rigorous circuital and electromagnetic simulations, followed by the fabrication process and experimental campaign.

1.1. Nonlinear Modelling of Ferroelectric-based Phase Shifters

The widespread usage of real-time tunable RF devices has led to increasing interest in ferroelectric materials. Traditional semiconductor-based phase shifters for reconfigurable antenna arrays and filters have limitations, including high DC voltages and associated losses [1]. Devices such as phase shifters, phased arrays, and filters, achieving interesting performance, with moderate losses and good power-handling capabilities have been presented in [2-3], exploiting Barium Strontium Titanate (BST). Furthermore, the ferroelectric properties of BST-based devices are possible with micrometer thicknesses, which enable power-handling capabilities but limit device miniaturization.

Thanks to their CMOS (Complementary Metal-Oxide-Semiconductor) compatibility, HfZrO ferroelectrics have lately attracted attention as a possible candidate for next-generation tunable RF devices.

Incorporating Zirconium Oxide (ZrO_2) into Hafnium-oxide (HfO_2) results in a dielectric constant rise of up to 35.2 times [4]. In [5], a 1-mm-long coplanar interdigitated capacitor (IDC) is designed over a 6-nm-thick HfZrO ferroelectric produced directly on a High-Resistivity Silicon (HRSi) substrate and demonstrated particularly good measured performance.

However, designing and simulating nanometric layers in electromagnetic (EM) solvers can be time-consuming and produce unreliable results due to the large aspect ratio between the nanometric ferroelectric layer and the actual substrate. Despite some works about the circuit modelling of various geometries of phase shifters that have been presented in the literature [6-7], the state-of-the-art lacks appropriate modelling of ferroelectric-based passive devices. Based on the experimental results of a

ferroelectric IDC, a nonlinear model for circuit simulators is derived. Then, by means of rigorous Harmonic Balance (HB) simulation, the behavior of the modelled IDC is analyzed. Moreover, a bi-dimensional phased array, adopting the previously modelled phase shifter is presented.

This work was supported by the European Project H2020 FETPROACT- EIC-05-2019 “NANO-EH”, GA No. 951761.

1.2. Design of a Wide Dynamic Range Rectifier

RF-EH has gained significant attention recently given its low cost and simple manufacturing process. Most electronic devices normally require batteries for their functioning. However, such a setup includes additional costs for the batteries, enlarges the size of the device to accommodate the latter, and requires regular maintenance for the proper working of the device. RF energy harvesting offers the solution to these challenges by converting the RF energy received wirelessly into DC. Among the most promising candidates for the exploitation of RF-EH are Wireless Sensor Networks (WSN), which usually consist of a large number of sensors with low power consumption requirements [8]. The RF power level that reaches the receiver is usually variable and difficult to forecast in many real situations since it depends on the distance from the transmitter, its polarization, the radio channel characteristics, and the properties of the environment. That is why wide-dynamic-range rectification systems are gaining increasing interest with a view to reaching maximum RF-to-DC conversion efficiency in different environments. Usually, approaches include the use of multiple rectifiers, optimized for operation in different power ranges, depending upon the RF power available.

Several solutions have been proposed in the literature to drive power to the most appropriate rectifier, but many rely on external control units. In the approach of [9], a three-stage rectifier is proposed using a single-pole double-throw (SPDT) switch. This design has a relatively high minimum operating power, part of which is consumed by

the control system and the power monitoring unit. In particular, SPDT is driven by a monitoring system consisting of a microcontroller and a power detector, which increases power consumption, cost, and size of the EH system.

In contrast, the works in [10-12], introduce a selection method based on impedance matching. In such approaches, nonlinear optimization is used upon each rectifier branch in order to synthesize antenna-to-rectifier networks that exhibit high selectivity around a predetermined input power range. Such a model allows the power flow to be rerouted toward the most compatible rectifier, while this is minimal toward less compatible ones. Corresponding demonstrated peak efficiencies in [10],[11], and [12] are 60%, 81%, and 60%, respectively, for dynamic ranges of 29 dB, 40 dB and 40 dB, respectively. On the other hand, the minimum detected power required by those solutions to be turned on is quite high. Also, in [12], each of the rectifier branches possesses its own resistive load, and the power conversion efficiency (PCE) of the whole multi-branch system is calculated simply as the summation of all the rectified power across the branches. This scheme realizes higher efficiencies but is practically feasible only by using a multi-input Power Management Unit (PMU). Additionally, decoupling among stages is not controlled. Consequently, as the input power increases it will burn the low-power stage at the point where the breakdown voltage is reached by the diode. Another approach has been proposed in [13] where the zero-threshold enhancement-mode high-electron-mobility transistor (HEMT) is used for the rectifier circuit. An embedded circuit generates the required negative DC gate-source voltage, V_{GS}, to keep the transistor in its high-efficiency operating region.

A novel system of rectifiers to address dynamic power ranges of more than 40 dB starting from RF power levels as low as −20 dBm is proposed to overcome the forehead limitations in literature. It is proposed here that architecture is designed as the parallel connection of three rectifier branches, each optimized for a different range of input power levels. These branches are switched seamlessly and automatically based on the incoming RF power, without any external controls.

1.3. Design of Silicon-Integrated Rectennas Based on Multilayer Structure

Due to its low cost, high integration, and high reliability, silicon has been used as the ideal material for the integration of microwave circuits. However, some limitations occur in the case of silicon-based microwave circuits: narrow frequency range, material dispersion, high losses, and little power-handling capacity. Given the already mature technology of the microwave Integrated Circuit (IC), many works on monopoles, dipoles, and patch antennas are presented in the literature [14-15].

There are, however, some challenges to the integration of antennas on silicon substrates. The low resistivity of silicon, about 10-100 Ω·cm, provides a conductive path to ground and degrades antenna gain, even if HRSi wafers with a resistivity of at least 10,000 Ohm cm can be used to avoid this issue. Another major disadvantage of silicon integration is the relatively high dielectric permittivity of the substrate, which results in most of the radiation taking place within the substrate rather than in free space and greatly decreasing the radiation efficiency of the antenna. Several methods have been presented in the literature for improving the performance of RF circuits on silicon substrate antennas. For instance, these include a membrane [16] or supports that create a thick air layer beneath the radiating element [17], thus effectively suspending the antenna over an air cavity.

These structures have been shown to improve radiation efficiency. However, one major drawback associated with this technique is that drilling on the silicon substrate makes the structure very fragile and complex to be realized. In this thesis, a novel topology and fabrication technology for silicon-integrated antenna is presented. Moreover, two demonstrative designs are presented. These include two rectennas operating at 2.45 GHz and 27 GHz, compatible with modern CMOS technology, built on a multi-layer substrate based on HRSi. The synthetized low-permittivity substrate, obtained by stacking mixed layer of silicon and air, allows to obtain a high radiation efficiency for the antenna.

This work was supported by the European Project H2020 FETPROACT- EIC-05-2019 “NANO-EH”, GA No. 951761.

1.4. Biological Sensing Actuated by Non-invasive Microwave Solutions

Recently, microwave sensors have gained considerable attention due to their high accuracy, cost-effectiveness, and relatively ease of fabrication processes [18-19]. These advantages have helped their applications in many fields, such as structural monitoring [20], biomedical sensing [21], material characterization [22], and permittivity measurements [23]. Considering the continuously deteriorating climate crisis, the importance of monitoring biological parameters such as hydration can be of vital importance in both human and agricultural applications. Adequate hydration is crucial for maintaining human health since disturbances can negatively affect cognitive and physical performance. For example, changes in epidermal water content contribute to such dermatological conditions as burns, edema, inflammation, and skin cancer [24-26]. Various technologies have been used in the literature for skin hydration status assessment [27-29]. However, they are rather expensive and not widely available. Besides, these techniques cannot be put into practical use in regular screening processes due to size and non-portable devices. Most of them also lack a machine learning (ML) algorithm that may help increase the accuracy of such a system considerably. In this thesis, a resonator-based skin hydration sensor based on a low-cost complementary split-ring resonator (CSRR) operating in the frequency band of 2-3 GHz, is presented. Also, the implementation of a classification algorithm together with a low-cost, non-invasive, portable, and wearable microwave sensor based on a CSRR is developed.

The topic of hydration monitoring is gaining increasing interest not only in medical applications but also in agriculture. Due to climate change, tree moisture assessment cannot be overemphasized because it highly contributes to maintaining

their vitality by facilitating cellular processes, ensuring leaf turgor, and enhancing general plant development [30].

Oscillator-based microwave sensors are widely adopted for deep penetration measurements due to the output power they can provide. They also have been utilized for material characterization [31-33], where changes in oscillation frequency and output power are measured using a vector network analyzer (VNA) and/or a spectrum analyzer [34-35]. To overcome these issues, a lightweight stand-alone system for moisture content detection, based on a self-oscillating antenna operating in the 2.4 GHz band, was designed, fabricated, and tested. The principle of its operation is based on the nonlinear relationship between the oscillator steady-state regimes under different loading conditions and its DC operating points. By monitoring the power consumption of the self-oscillating antenna, it is possible to retrieve the correct moisture content of the wood sample with a simple microcontroller, avoiding the need for any bulky and expensive RF instrumentation.

1.5 Microwave Antenna System for Train Positioning and Signaling

Security and monitoring have always been some of the most challenging issues in the railway transportation field. Nowadays, innovative solutions based on wireless technologies are being explored in order to provide flexible and secure approaches for train integrity and localization. Recent applications involve testing the Global Navigation Satellite System (GNSS) for the detection of virtual balises [36] in view and have become part of the European Rail Traffic Management System (ERTMS), which makes possible the continuous and reliable self-monitoring of trains by broadcast of data about their integrity and their positioning in real time [37-38]. A new application of GNSS combines satellite communication with real-time data from kinematic sensors such as current train speed [39-40]. More enhancements in the train localization system based on GNSS have also been developed by fusing localization data from GNSS with those from the inertial navigation systems, further enhancing

redundancy and accuracy of positioning while detecting faults in GNSS signals. In addition to communications via satellites, vehicle-to-everything (V2X) technologies introduce the following options regarding railway localization and the integrity of trains. Various wireless communication technologies such as LoRa, Zigbee, Worldwide Interoperability for Microwave Access (Wi-Max) , and 4G are under study to develop robust V2X communication architecture. The fact that LoRa has a very long-range distance with low power (up to -20 dB below the noise floor) makes it highlighted as a promising technology in intelligent transportation systems analysis [41]. Despite the interest in V2X scenarios, LoRa performance is still not well exploited for train integrity. This paper develops simulations to show different LoRa configurations that can meet the demands of extended range and connectivity in vehicular networks. Complementary to simulations, real-world evaluations have proposed low-power and reliable architectures using LoRa in moving vehicles and in different ambient conditions [42-44].

The first attempts toward applying the LoRa protocol in the railway sector focus on creating high-speed communication channels between moving LoRa gateways on trains and sensors along the track. The performance of LoRa has been widely studied within a series of challenging conditions, including device mobility. Besides, LoRa has been reported in application to several V2X communications with the capability of traffic safety, vehicle networking, and area network control. Moreover, its cost is economical enough for widespread applications.

The primary objective of the project is to propose a network architecture that can correctly track the trains running on secondary lines, able to ensure their integrity. The proposed scenario foresees, for each wagon of every train, low-power, low-cost sensor nodes spread along the intelligent poles on single-track railway lines at every 250 meters. In this scenario, the train convoy may have between one and four wagons. The main motivation is to allow the operation of two or more trains at the same time on the same secondary railway. Such would suppress the bottleneck situation whereby only

one can operate at any given time, due to lack of adequate information on the exact location of these.

Chapter 2

Nonlinear Modelling of Integrated and Reconfigurable Passive Phase Shifters Based on Nanoscale-Ferroelectrics

This chapter is based on the following publications:

S. Trovarello, A. Di Florio Di Renzo, M. Aldrigo, D. Masotti, M. Dragoman and A. Costanzo, "Nonlinear circuit model of IDCs on ferroelectric nanomaterial for reconfigurable applications," 2022 52nd European Microwave Conference (EuMC), Milan, Italy, 2022, pp. 175-178,

S. Trovarello, A. D. F. D. Renzo, M. Aldrigo, D. Masotti, M. Dragoman and A. Costanzo, "Nonlinear Modelling of Steerable Antenna Array by Ferroelectric Capacitors Based on Nanoscale Layers of HfZrO," 2023 53rd European Microwave Conference (EuMC), Berlin, Germany, 2023, pp. 524-527,

2.1 Introduction of the Chapter

In this chapter, a nonlinear model of voltage-controlled IDC using ferroelectric nanomaterials for tunable RF circuits is reported. In particular, the voltage nonlinearity of HfZrO from nanoscale thickness is exploited for the implementation of an IDC on high-resistivity silicon substrates. These devices are foreseen to play a crucial role in those applications that require real-time reconfigurability, such as in the case of intelligent reconfigurable surfaces, which are currently gaining tremendous interest in the framework of 5G technology and beyond. It is demonstrated that ferroelectrics based on doped HfO_2 offer remarkable tunability for microwave circuits. This tunability is essential for developing wireless communication systems that need to meet requirements such as miniaturization and low energy consumption. Achieving these qualities has been challenging with traditional ferroelectrics, previously used in tunable

microwave applications, because they are not fully compatible with CMOS technology and require high voltages to produce a significative phase shift in the microwave range. In contrast, HfO_2-based ferroelectrics are fully CMOS-compatible and can be scaled down to a thickness of just 2–3 nm, nearly at the atomic level. This allows for significant tunability in various circuits, especially in components like filters or phase shifters, at much lower voltages. The main goal of this activity is to overcome the limitation of traditional EM solvers, which cannot consider the nonlinearity of the ferroelectric material, and moreover cannot predict the performance of the device under different excitation levels. The proposed nonlinear model is general-purpose, derived from experimental data obtained under varying frequency and biasing conditions, hence valid for both low-power and high-power regimes. Preliminary HB analyses demonstrate the model's robust convergence, handling input power levels up to 40 dBm effectively. For demonstrative purposes, the design of a novel integrated into silicon, 2-D reconfigurable 2x2 antenna array operating at 2.45 GHz, is reported.

This work was supported by the European Project H2020 FETPROACT- EIC-05-2019 “NANO-EH”, GA No. 951761.

2.2 General-purpose Nonlinear Models of HfZrO-based IDCs

Figure 2.1 illustrates the layout of the measured two-port and 15-finger IDC [45]. The substrate used is a 6-nm-thick HfO_2 thin film, which is grown using the atomic layer deposition (ALD) technique on a 4-inch, 525-μm-thick high-resistivity silicon (HRSi) wafer. The ferroelectric HfO_2 film is prepared through successive incorporation of two metal-organic precursors of hafnium and zirconium in the 2:1 ratio on the silicon wafer, followed by the oxidation process to produce a homogeneous binary oxide. X-Ray Reflectivity (XRR) measurement identified the thickness of the film at approximately 6 nm. The metallization is deposited using electron beam evaporation. The final structures are defined photolithographically using a standard lift-off process

on the 6-nm-thick HfZrO substrate in coplanar waveguide technology. Table 2.1 report the geometrical dimensions of the measured HfZrO-based IDC.

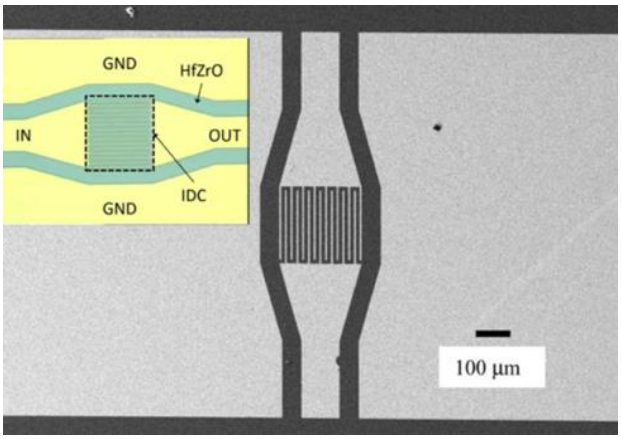

Fig. 2.1. Scanning electron microscope image of the IDC based on HfZrO realized in [5] and modelled in this work © 2022 EuMA.

Table 2.1
Geometry and dimensions (mm) of the measured IDC

Length	**Width**	**Finger length**	**Finger width**	**Finger gap**	**n° fingers**
1	0.3	0.191	0.005	0.010	15

Figure 2.2 shows the equivalent circuit model, comprising five lumped elements, out of which only C_i, representing the interdigitated capacitor, is modeled as nonlinear and dependent on the applied DC voltage.

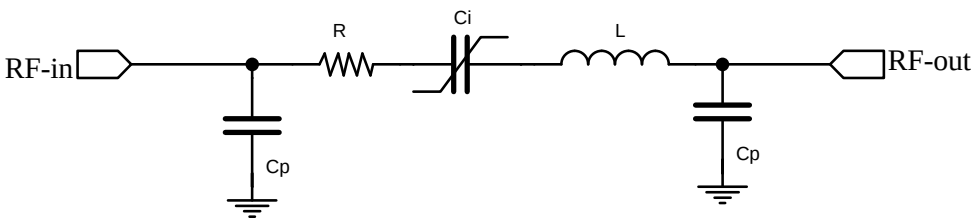

Fig. 2.2. IDC equivalent circuit model [45] © 2022 EuMA.

From the measured S-parameters, a fitting over the whole frequency range from 1 GHz to 10 GHz, considering a polarization equal to 0.2 V, is performed in order to

identify the values of the equivalent circuit model components that are voltage-independent. Resistance and inductance values are considered constant for each polarization because they are not affected by the externally applied DC voltage and therefore the changes in terms of the permittivity of the substrate are negligible for these components. Moreover, the nonlinear parasitic capacitances are considered equal, constant, and linear for simplicity, since it is verified that by changing the polarization their variation is small and negligible with respect to the series finger nonlinear capacitance. Circuit simulations are carried out using Keysight advanced design system (ADS) circuit simulator, to extract the values of the voltage-independent equivalent circuit components. The minimization of the S-parameters errors S_{err} and φS_{err} are defined, to perform an accurate extrapolation:

$$\min S_{err} = \left|S_{ijsim} - S_{ijmeas}\right| \; \forall \; i,j \neq 0 \tag{2.1}$$

$$\min \varphi S_{err} = \varphi\left(S_{ijsim}\right) - \varphi(S_{ijmeas}) \; \forall i,j \neq 0 \tag{2.2}$$

From circuit optimizations, the values of the linear parameters extracted are R = 80 Ω, L = 10^{-4} nH, C_p = 0.08 pF, and C_i 1.2 pF. Maintaining these achieved values fixed in the equivalent circuit, eleven fitting simulations are performed, for dc polarization values from -1V to 1V, in a limited frequency range from 2.4 GHz to 2.6 GHz centered around the frequency of interest 2.45 GHz, to extrapolate the values of the series non-linear finger capacitance of the equivalent circuit of the IDC as a function of the polarization. Figures 2.3 and 2.4 compare the simulated and measured S_{11} parameters and the phase of the transmission coefficient as a function of frequency for selected DC bias levels: -1 V, -0.6 V, 0 V, 0.6 V, and 1 V. In fact, good agreement between the measurements and simulations is observed over the specified bias and frequency ranges. The discrepancies between the simulated and measured S_{11} are in the worst case about 5% and 13% at the fundamental and second harmonic frequencies,

respectively. For the phase, S_{21} simulations show differences of 3% at 2.55 GHz and 11% at 5.1 GHz.

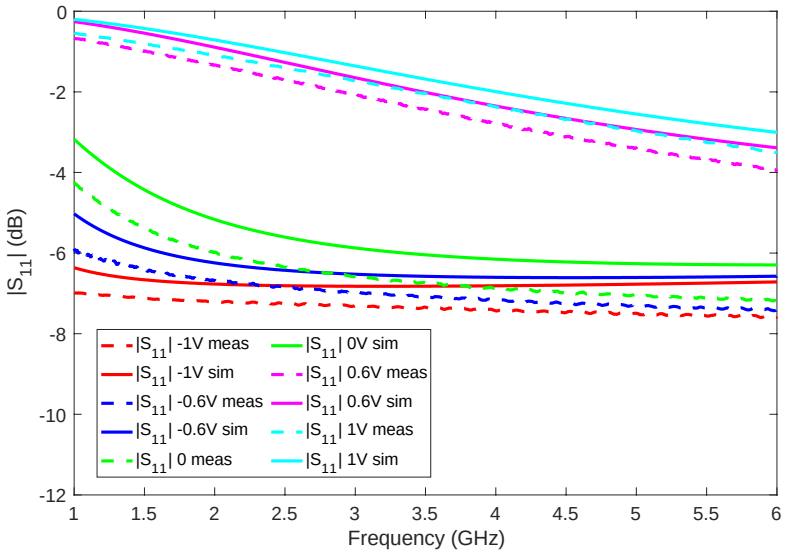

Fig. 2.3. Measured and simulated reflection coefficient from 1 to 6 GHz, for DC bias ranging from -1 V to 1 V [45]. © 2022 EuMA.

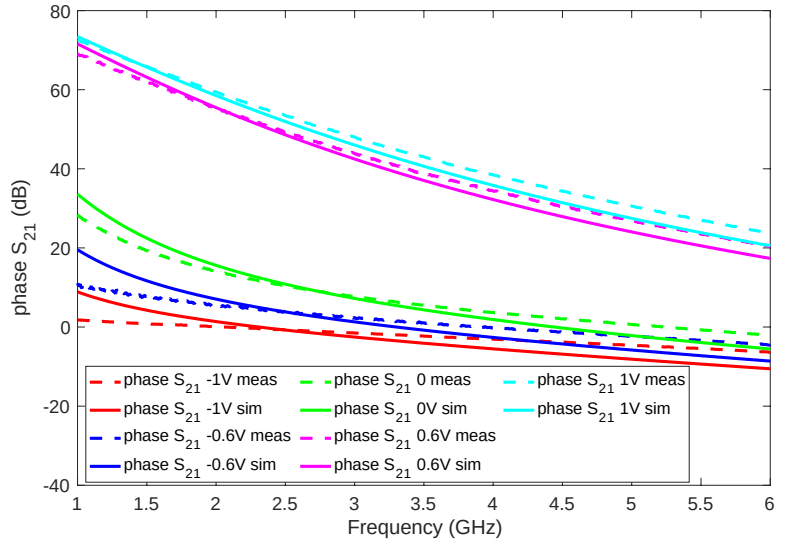

Fig. 2.4. Measured and simulated transmission coefficient from 1 to 6 GHz, for DC bias ranging from -1 V to 1 V [45]. © 2022 EuMA.

The capacitance values for each bias point are derived over the interval -1 to 1 V. These are identified by means of a closed-form expression in analytic form as follows:

$$C_i(v_{bias}) = [a \bullet \tanh(b \bullet e^{-c \bullet v_{bias}}) + d] \quad (2.3)$$

The parameter values for the optimal fit are determined as follows: a = $5.03 \cdot 10^{-12}$, b = 0.15, c = -2.18, and d = 0.03. As shown in Figure 2.5, the capacitance $C_i(v_{bias})$ closely matches the experimental measurements within the specified polarization range. The chosen closed-form expression provides a numerically stable expression when the I_{DC} is excited with large-signal excitations, which drives the time-dependent bias of the I_{DC} beyond the range measured experimentally. The model is continuous and differentiable across the entire domain; thus, it allows robustness for high-power analysis. A user-defined model in ADS Keysight is used to simulate the I_{DC} behavior in circuit simulations. In particular, a nodal coding of the NETLIST is adopted.

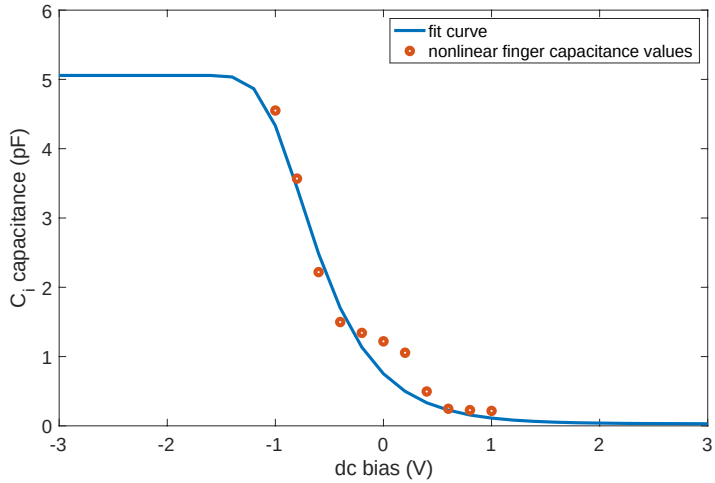

Fig. 2.5. Comparison between modeled and measurements extracted I_{DC} nonlinear capacitance versus dc bias [45]. © 2022 EuMA

Figure 2.6 compares the $|S_{11}|$ and $|S_{21}|$ parameters for HB simulations performed with small-signal excitation and measurements at both the fundamental frequency and second harmonic, where the agreement is good in both harmonics.

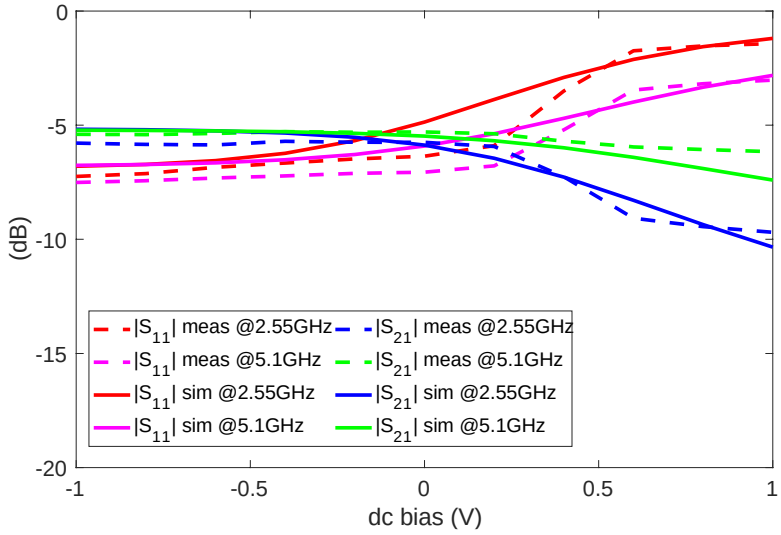

Fig. 2.6. Modelled and measured $|S_{11}|$ and $|S_{21}|$ parameters at 2.55 and 5.1 GHz of the proposed IDC [45] © 2022 EuMA.

To verify the power handling capabilities of the I_{DC} model, an HB simulation is performed from small-signal to large-signal excitation within an input power range of 60 dB, from -20 dBm up to 40 dBm. Figure 2.7 illustrates the simulated results when an RF signal is superimposed on the I_{DC} DC bias. Above 10 dBm of input power level, the performance degrades, while for the highest power considered, it can be noticed a negligible variation in phase, as the DC bias varies.

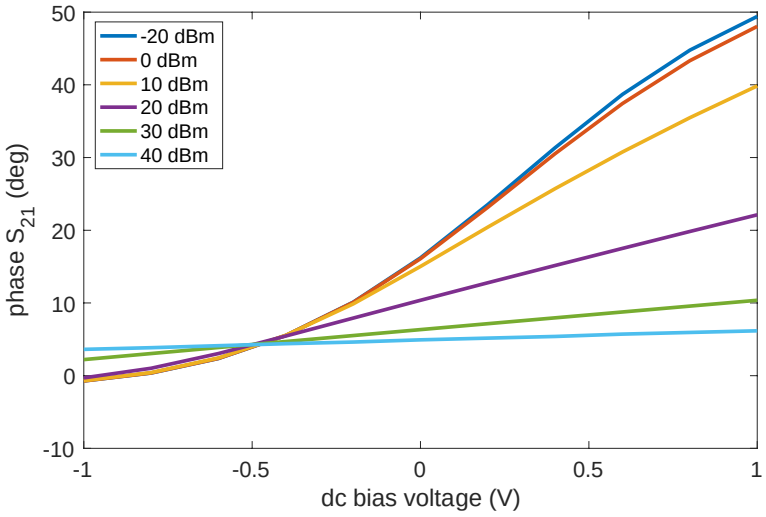

Fig. 2.7. Simulated phase of the transmission coefficients parameters at 2.45 of the proposed I_{DC}, for different input power levels [45] © 2022 EuMA.

The nonlinearity of the device is also verified by monitoring the output power spectra for different input power levels (-20 dBm, 0 dBm, and 20 dBm) as shown in Figures 2.8(a-c). In particular, an increase in the higher harmonic terms and in the DC component can be observed, as the power increases.

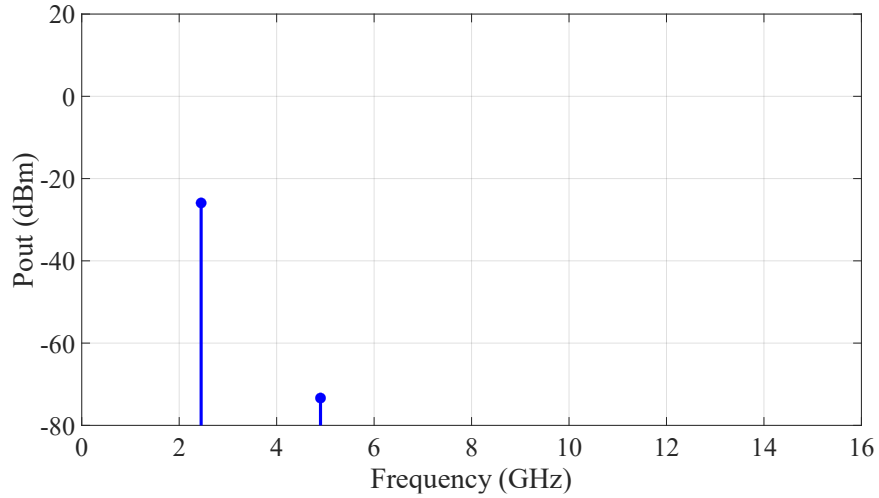

(a)

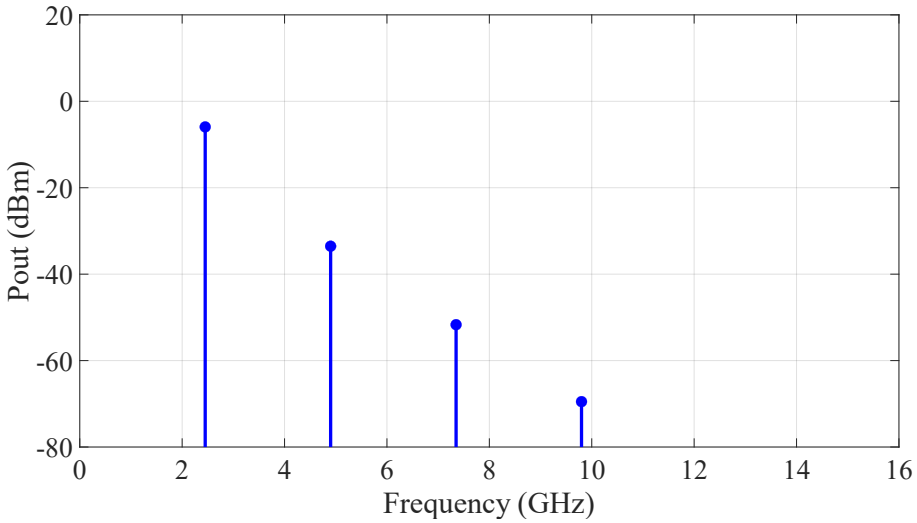

(b)

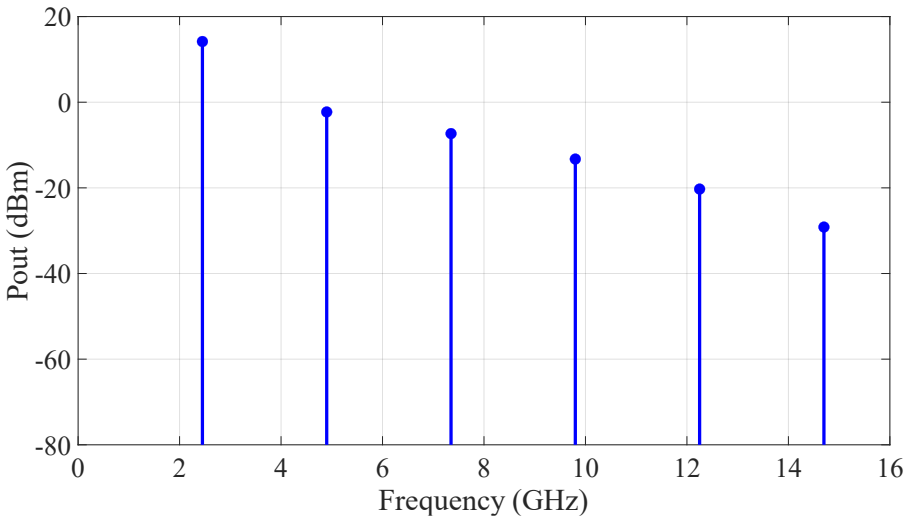

(c)

Fig. 2.8. Simulated output power spectrum for input power equal to (a) -20 dBm, (b) 0 dBm, and (c) 20 dBm for a fixed DC bias of 0 V.

Furthermore, due to nonlinear distortion, the non-sinusoidal output is a nonlinear function of the IDC bias conditions, at any input power level. As a reference, 10 dBm at the input port are considered. Figure 2.9 shows the simulated time-domain voltage across the IDC.

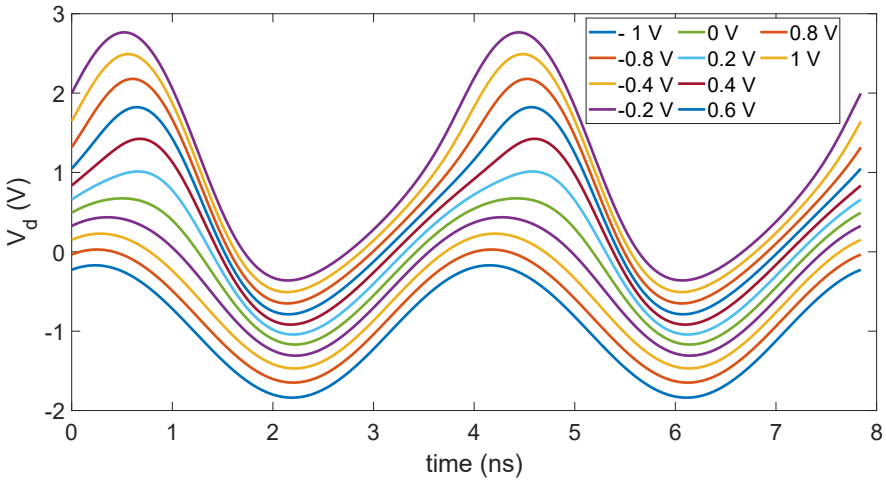

Fig. 2.9 Simulated time-domain voltage across the nonlinear IDC, obtain for an input power of 10 dBm by means of Harmonic Balance simulations and by varying the applied DC bias between -1 V and 1 V.

In the first version of the general-purpose nonlinear model of HfZrO-based IDC, only the ferroelectric capacitance between the fingers is modeled as nonlinear. Anyway, due to the fabrication process of the device, which consists of depositing ferroelectric material all over the IDC area, it is important to consider the nonlinear behavior of all the structures, which includes nonlinear losses of substrate and nonlinear matching of the coplanar waveguide (CPW) transmission line concerning the applied DC bias. For this reason, a second, and more complex, model is derived from measurements.

Based on the approach in [46], from small-signal measurements at 2.45 GHz, a complete equivalent circuit model of the IDC, suitable for both small- and large-signal applications, is derived. Given the symmetrical layout of the IDC reported in Figure 1, a pi-network is adopted for the equivalent circuit, as shown in Figure 2.10 (a). Y_a models the series branch of the IDC, which consists of the ferroelectric capacitance between the fingers and the associated losses, while Y_b and Y_c represent the losses and parasitic capacitances of the lateral and bottom ground planes. It is noteworthy to mention that, given the symmetry of the fabricated device, Y_b=Y_c. The selected circuit equivalent model is shown in Figure 2.10 (b) together with the schematics of the RF and DC feeding networks. In this figure, the voltage across the IDC fingers, denoted as v_{IDC}, is also depicted, which is utilized as the state variable for the IDC in HB simulations. This agrees with the concept suggested in [45], according to which the through-branch of the model contains two nonlinear elements, C_s and R_s, representing respectively the nonlinear capacitive interactions between the IDC fingers and the losses, in a parallel arrangement. Given the symmetry of the fabricated device, the Y_a branch is biased with v_{IDC}, while the other two branches with the halved state variable, to maintain the consistency and the symmetry of the circuit.

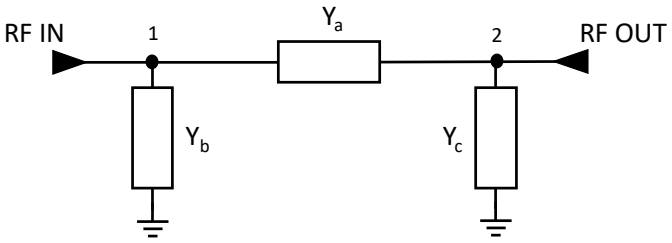

(a)

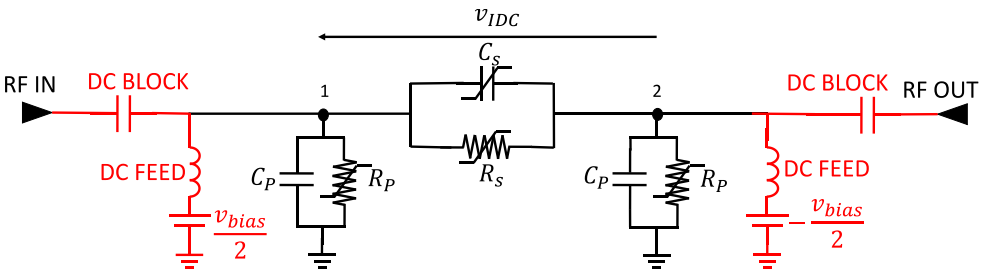

(b)

Fig. 2.10. The six-lumped elements equivalent circuit adopted the proposed IDC-based phase shifter [47] © 2023 EuMA.

Through the pi-network shown in Figure 2.10(b) and its admittance matrix, it is possible to extract the circuit parameters at each frequency of interest, as shown below:

$$Y = \begin{bmatrix} Y_{11} & Y_{12} \\ Y_{21} & Y_{22} \end{bmatrix} = \begin{bmatrix} Y_a + Y_b & -Y_a \\ -Y_a & Y_a + Y_b \end{bmatrix} = \begin{bmatrix} \frac{1}{R_p} + j\omega C_p + \frac{1}{R_s} + j\omega C_s & -\frac{1}{R_s} - j\omega C_s \\ -\frac{1}{R_s} - j\omega C_s & \frac{1}{R_p} + j\omega C_p + \frac{1}{R_s} + j\omega C_s \end{bmatrix} \quad (2.4)$$

$$R_p = \frac{1}{Real\{Y_{11}\}+Real\{Y_{21}\}} \quad (2.5)$$

$$R_s = -\frac{1}{Real\{Y_{21}\}} \quad (2.6)$$

$$C_s = -\frac{Im\{Y_{21}\}}{\omega} \quad (2.7)$$

$$C_p = \frac{Im\{Y_{11}\}+Im\{Y_{21}\}}{\omega} \quad (2.8)$$

The extracted nonlinear lumped elements from Equation (2.5-2.8), are composed of two parts: a nonlinear function of the voltage across the ferroelectric material and a

constant contribution given by the HRSi silicon. The expression of C_s as a function of v_{IDC} is reported in Equation 2.9, where C_0 denotes the HRSi constant behavior:

$$C_s(v_{IDC}) = a \cdot e^{\frac{-(v_{IDC}-\mu)^2}{\sigma}} + C_0 \quad (F) \tag{2.9}$$

Similarly, R_s incorporates a constant term (R_{s0}) that accounts for the losses associated with the multilayer substrate, as well as a nonlinear function of v_{IDC}:

$$R_s(v_{IDC}) = b \cdot \tanh(c \cdot v_{IDC} + d) + R_{s_0} \quad (\Omega) \tag{2.10}$$

While the branches are parallel and symmetrical, each of them consists of a linear capacitance C_p, modeling the capacitive coupling between the CPW signal line and the lateral ground planes, and nonlinear resistance R_p whose value depends on half the state variable: this configuration describes the ferroelectric behavior of the nanometric material.

$$R_p(v_{IDC}/2) = f \cdot \tanh\left(g \cdot \frac{v_{IDC}}{2} + h\right) + R_{p_0} \ (\Omega) \tag{2.11}$$

Note that R_p in the left and right branches above is a function of $v_{IDC}/2$ and $-v_{IDC}/2$, respectively, to maintain consistency with the voltage across the R_s-C_s branch. All the parameters adopted in the closed-form equations are given in Table 2.2.

Table 2.2
Parameters of the closed-form equations (2) – (4) [47] © 2023 EuMA.

a	**b**	**c**	**d**	**f**	**μ**	**σ**
2.55e-13	730.8	4.946	-2.75	-280.5	0.15	0.6
C_0 (pF)	**Rp_0 (Ω)**	**Rs_0 (Ω)**	**C_p (pF)**	**g**	**f**	**h**
0.155	1827	818.2	0.95	-2.35	-280.5	1

For any bias point within the measured range of ±1 V, and across the measured frequency range, the parameters of the nonlinear functions are extracted from the measured Y-matrix. These derived closed-form functions are further numerically extrapolated beyond the available measured bias points to avoid numerical overflow when large signals are applied to the RF input port.

Figure 2.11 compares the magnitudes and phases of the reflection and transmission coefficients from modeled and measured values using HB simulations with small-signal excitations at the fundamental frequency of 2.45 GHz. The simulation is in good agreement with the measurements over the range observed. The mean discrepancies between the measured and simulated values of $|S_{11}|$, $|S_{21}|$, the phase of S_{11} and the phase of S_{21} are 0.18 dB, 0.21 dB, 0.74°, and 1.23°, respectively.

Figure 2.12 shows the model behavior in the 1-11 GHz range, for a representative polarization case, which is set to 1 V. Regarding the return loss, the comparison between measurements and simulations shows good performance in the 1-6 GHz band for both the magnitude and phase. For what concerns, the simulated transmission coefficient, a higher precision is observed, where the maximum discrepancies are 3 dB and 4°, for the magnitude and phase of the S_{21} coefficient, respectively. Similar performances are observed, for the other DC bias points, which are not shown for brevity's sake.

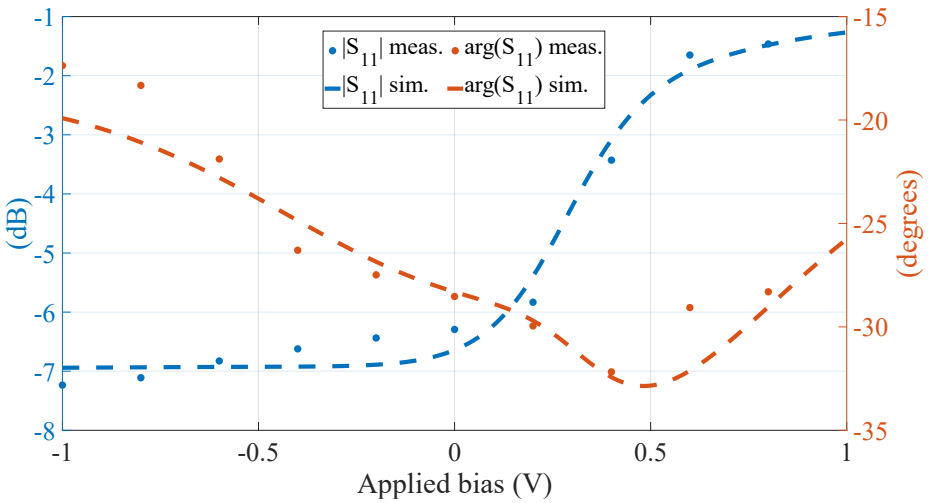

(a)

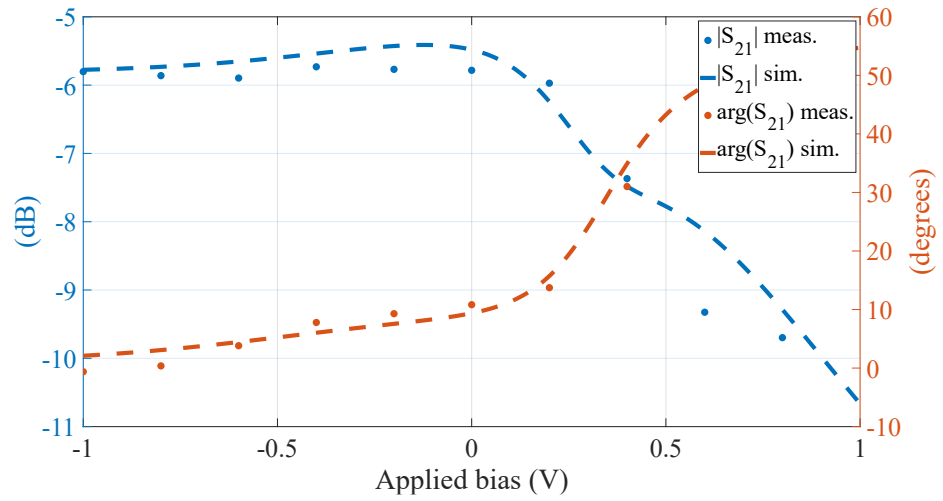

(b)

Fig. 2.11. Comparison between measured and simulated (a) reflection coefficient, and (b) transmission coefficient in terms of magnitude and phase at 2.45 GHz, as the applied DC bias varies in the ±1 V range [47] © 2023 EuMA.

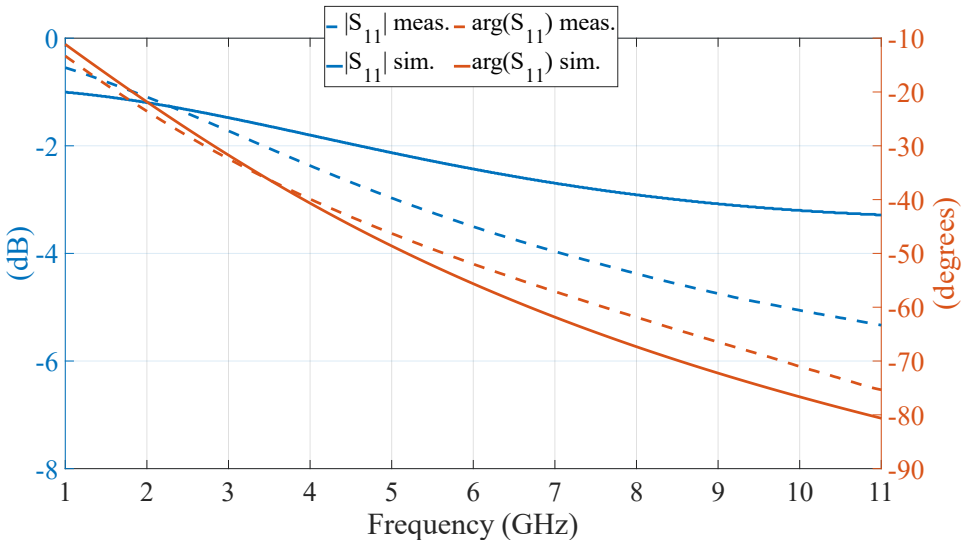

(a)

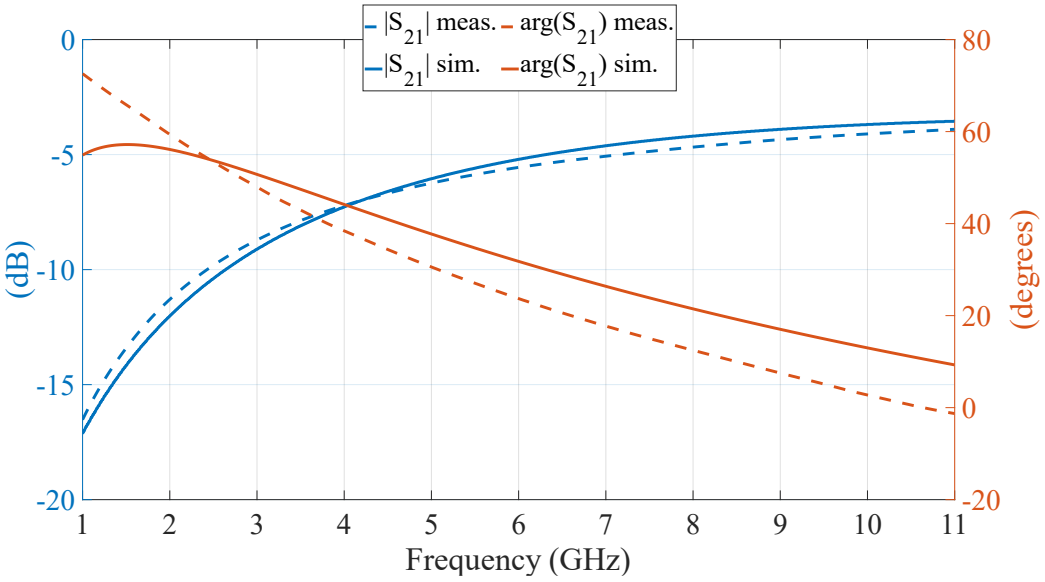

(b)

Fig. 2.12. Comparison between measured and simulated (a) reflection coefficient, and (b) transmission coefficient in terms of magnitude and phase from 1 GHz to 11 GHz, for an applied DC bias equal to 1V.

2.3 NL-EM Co-Simulation of a Four-Element HfZrO-based Phased Array

For demonstrative purposes, the NL/EM co-design of a 2-D 4-element integrated phased array operating at 2.45 GHz is carried out. The proposed design of a 2D 2x2 coaxial-fed patch antenna array is realized on a 1.52 mm thickness ROGERS RO3003 substrate having $\varepsilon_r = 3$ and $\tan\delta = 0.001$, as shown in Figure 2.13 (a). The array design utilizes a high-performance commercial substrate to mitigate the challenges arising from surface wave excitation and subsequently poor radiation efficiency of antennas that are directly deposited on silicon. In this respect, the stacked antenna array is placed on layer L1, whereas the four IDCs, fabricated using coplanar waveguide technology on layer L2, are connected to the coaxial feeds of antennas through wire bonding. Besides, the model also includes four biasing via-holes to bring the required DC bias to previously modelled capacitors.

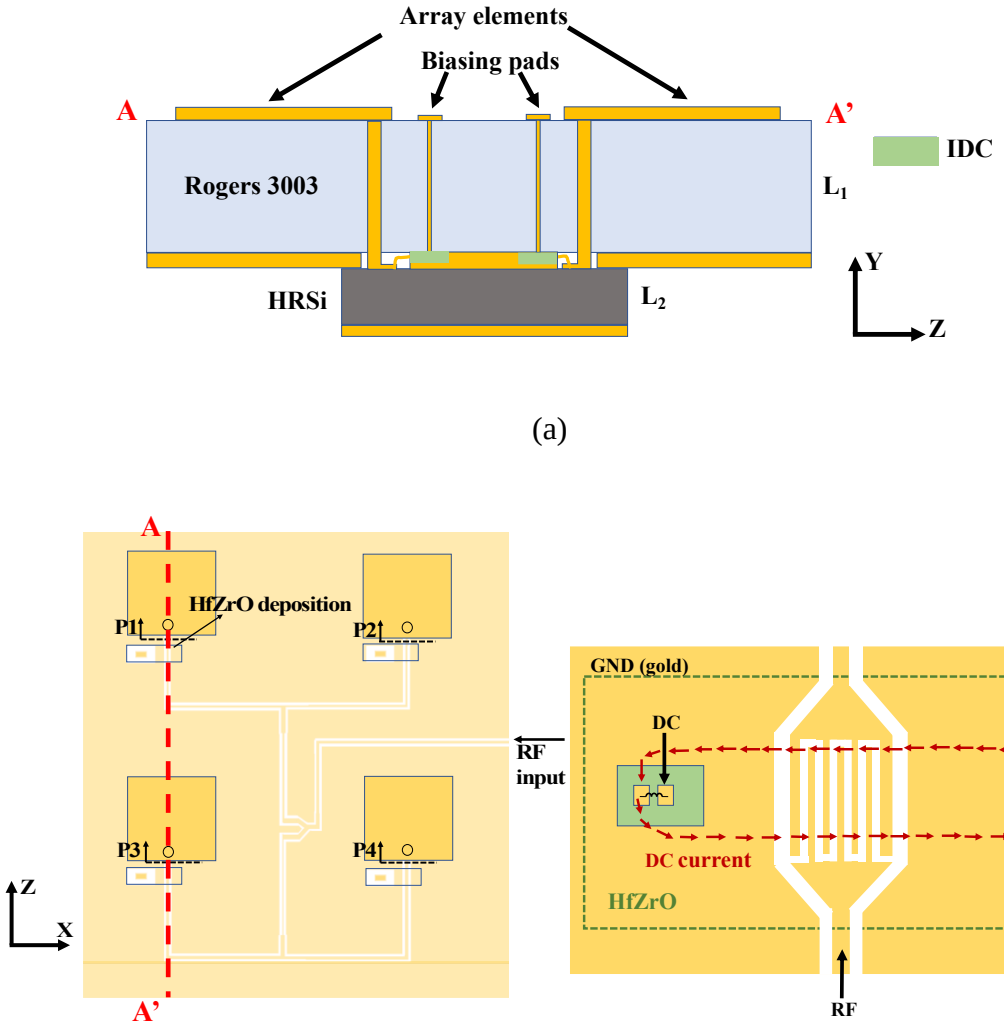

Fig. 2.13. (a) YZ-cross section of the stacked array integrated on silicon, (b) top view of the 2D array (with the antenna substrate removed for clarity), and (c) top view of the IDC embedded within the CPW array feeding network, where the dotted green area indicates the HfZrO deposition region. Dimensions are not in scale [47] © 2023 EuMA.

The feeding network of the array was designed on HRSi because of integration with the ferroelectric capacitors. The layout is shown in Figure 2.13(b). A corporate feeding network with quarter-wavelength transformers is employed for proper impedance matching at the input port. The input T-junction uses a power divider in such a way that the two main arms of the array are decoupled to minimize reflected power from the IDCs, especially in positive bias conditions. Figure 2.13(c) shows a top

view of the biasing pads where a hole is etched into the lateral ground plane. An insulating material is placed beneath the bias pads, which prevents RF currents from flowing into the biasing circuit, and an inductor such as an RF choke is used. In such a configuration, vertical polarization can be applied between the top and bottom contacts of the ferroelectric layer. To avoid any detuning of the antennas and feeding network for different values of bias, only the area around the phase shifters is covered with HfZrO. From the stacked configuration in Figure 2.13(a), the overall dimensions of the four-element array are 130x130 mm² while the area occupied by the HRSi is limited to 61x61 mm². First, the four-port network made of patches fabricated with CPW technology is electromagnetically simulated, and S-parameters as well as far-field performance under reference excitations are calculated. Then, obtained radiating linear four-port network data are exploited into a nonlinear circuit simulator as the load network for the reconfigurable nonlinear array's CPW feeding. That nonlinear-electromagnetic co-simulation approach enables us to predict the array radiation pattern as a function of the DC bias of the I_{DC}s with a negligible computation time, while electromagnetic simulations would take for this number of unknowns several hours and cannot account for nonlinearities in the I_{DC}s.

Table 2.3
IDC bias distinct set up for the numerical simulations of Fig. 2.13.

	P1	**P2**	**P3**	**P4**	**Set n.**
Elevation	-0.8 V	-0.8 V	0.8 V	0.8 V	1
	0.8 V	0.8 V	-0.8 V	-0.8 V	2
Azimuth	-0.8 V	0.8 V	-0.8 V	0.8 V	3
	0.8 V	-0.8 V	0.8 V	-0.8 V	4

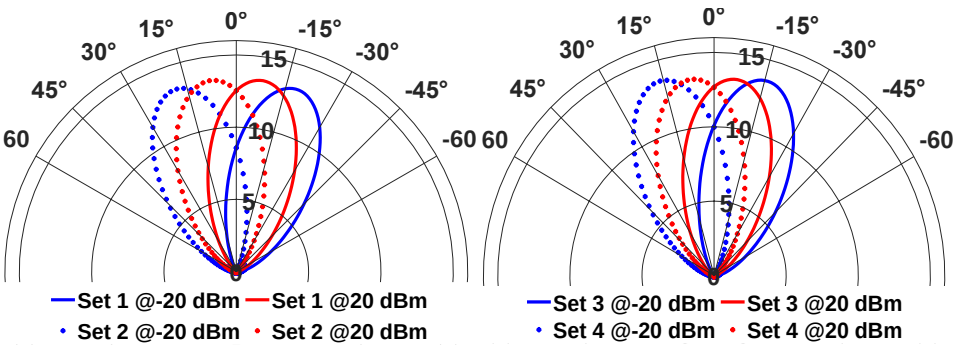

(a) (b)

Fig. 2.14. Simulated normalized radiation pattern on the azimuthal (a) and elevation (b) plane, obtained from NL/EM co-simulations of two different input power levels at RF port of the array (-20 dBm and +20 dBm), for the set of DC bias reported in Table 3 [47] © 2023 EuMA.

Subsequently, the behavior of the reconfigurable array performance has been investigated under different levels of the RF excitations, to investigate its power handling capabilities. This approach easily allows foreseen the array behavior not only under varying bias conditions applied to the HfZrO ferroelectric material of the I_{DC}s but also as a function of the nonlinear RF regime of the array. Figure 2.14 presents the NL/EM co-simulation predicted steering performance in the case of -20 dBm and +20 dBm power for the I_{DC} bias listed in Table 2.3 for 2D-beam steering. From the plots, it can be seen that, in the small-signal regime, the array can scan up to ±16° in elevation and ±18° in the azimuth plane. However, NL/EM co-simulations highlight that nonlinearities of the I_{DC}s at large-signal excitations reduce the array's steering capability. The obtained behavior agrees with the results in Figure 2.7, showing phase compression of the IDC output current for input power levels higher than 10 dBm.

2.4 Conclusions of the Chapter

In this chapter two nonlinear equivalent circuits for ferroelectric-based IDCs are presented. The first, simpler, offers a fast and easy approach to preliminary evaluate the nonlinear behavior of HfZrO and in general ferroelectric-based passive phase shifter. The model consisting of only one nonlinear lumped element, offers a good precision concerning experimental measurements. The second model proposed in the thesis offers a higher precision at the expense of a more complex equivalent circuit, where 4 nonlinear lumped elements are included. In particular, the capacitance between the IDC finger, the parasitic effects, and losses are characterized as nonlinear, given the HfZrO layer. The equivalent circuit is verified using HB simulations, from which the power-handling capabilities are retrieved. The phase-shifting properties of the material and the device itself have been tested by designing a 2x2 phased array, where the power-dependent behavior of the device is analyzed. In particular, a multilayer and stacked solution is proposed, to allow the use of both commercial RF substrate and silicon substrate. The proposed array shows a maximum beam steering of ±16° in the elevation and ±18° in the azimuth plane. The proposed equivalent circuits can be easily integrated into any HB simulators and adapted to different geometries of the IDC and different ferroelectric materials, by changing the model parameters.

Chapter 3

RF Energy-Harvester for Wide Dynamic Range Applications

This chapter is based on the following publications:

S. Trovarello, G. Paolini, D. Masotti and A. Costanzo, "A Modular System of Rectifiers for Energy Harvesting with Wide Dynamic Input-Range," 2021 6th International Conference on Smart and Sustainable Technologies (SpliTech), Bol and Split, Croatia, 2021, pp. 1-4,

S. Trovarello, G. Paolini, D. Masotti and A. Costanzo, "Cascaded Rectifiers for Energy Harvesting With a Wide Dynamic Power Range," in IEEE Journal of Radio Frequency Identification, vol. 7, pp. 64-73, 2023,

3.1 Introduction to the Chapter

In this chapter, an innovative RF-to-DC rectification system operating at 2.45 GHz with a wide dynamic range is presented. The main goal of the activity is to design a modular system, capable of being extended if needed, where the input power is automatically routed in the most suitable branch. The system is built from three rectifiers, each one optimized for a specific range of input power. These rectifiers work together using an adaptive distribution mechanism, ensuring that the input power is routed along the most efficient path for maximum RF-to-DC conversion across the entire power spectrum. The rectifiers' nonlinear behavior allows their RF input impedance to change based on the power level, which enables their alternating operation. Enhancement-mode HEMTs are used as passive switches in the RF path for the second and third rectifiers. These switches, relying on self-biasing, turn on and off automatically based on the incoming power. This design almost completely isolates the three branches, activating only one rectification path for any given power level. As the

input power increases, a portion flows through the HEMTs to the appropriate rectifier, while a DC switching network shorts the outputs of the inactive rectifiers. The rectifier circuit is described and validated in the following sections, with a comprehensive description of the design criteria and performance of the RF switches and power-selective matching network, the core of the presented activity. The rectifier is then fabricated and validated by an experimental campaign of measurements.

3.2 Design of the Cascade Rectifier

The architecture of the proposed wide dynamic range rectifier is implemented with three parallel rectifier branches, optimized for different power ranges. They are called Low-Power (LPR), Medium-Power (MPR), and High-Power Rectifier (HPR). All the rectifiers are switched on and off in an automated way according to the incoming RF power only, with no external control. This is achieved by a selective matching of three branches and the adoption of floating-gate unbiased HEMTs. Enhanced-mode HEMTs have been adopted because they can guarantee port isolation, and can operate without negative gate-source voltages [48], which makes the implementation easier with rectifiers.

The selected modular topology is easily expandable if more branches are needed to increase the dynamic range. A preliminary approach is presented in [49], where the simulated device is shown. Then an updated version of the prototype is designed, with an expanded overall dynamic range of the system to 45 dB and the performance of the device is experimentally verified.

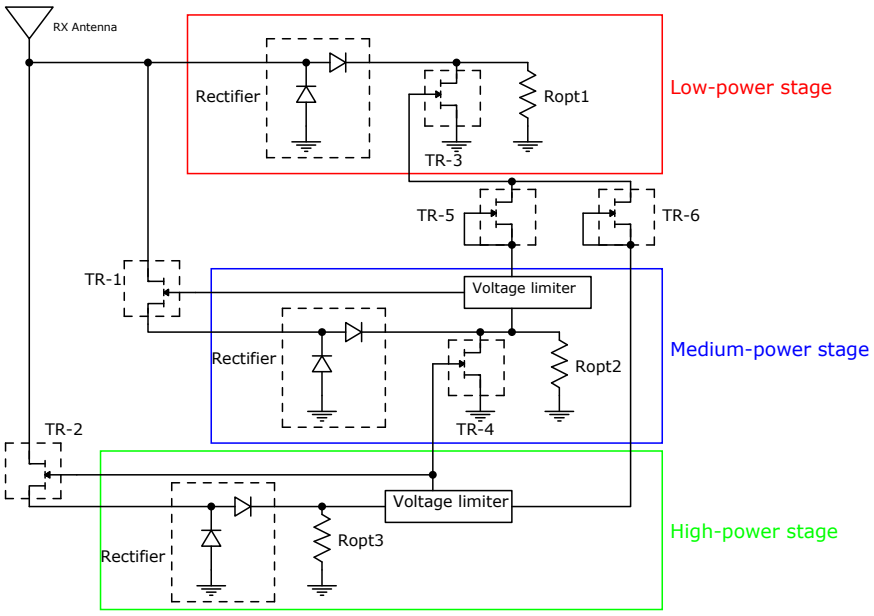

Fig. 3.1. Schematic of the proposed three-stage rectifiers: three distinct rectifiers are optimized for each input power operating region. Two RF switches are adopted to enable the correct RF path, while four DC switches provide the necessary de-coupling between the three rectifiers [50] © 2023 IEEE.

Figure 3.1 shows the architecture of the 45-dB wide dynamic range rectifier. The LPR is optimized to operate in the range from -20 to 0 dBm, the MPR from 0 to 9 dBm, and the HPR from 9 to 24 dBm. Seamless activation of the appropriate rectifier and deactivation of the others is based on synchronized operation of switch-based components driven in pairs. In particular, when an RF switch is adopted to turn on an RF path, a DC switch is exploited to decouple the other branches.

For input power levels higher than 0 dBm, two switches turn on: one in the RF signal path and the other in the DC path. The latter, shorting the LPR load to ground, creates a strong mismatch between the LPR load and the RF source, allowing all the power to go through only the MPR.

Two main phenomena were considered in the design of the proposed system: the self-biasing of the HEMTs and the nonlinear power-selective design of the RF matching networks in the three rectification branches. Indeed, the self-biasing mechanism allows a branch to be turned on without any external biasing. The power-selective matching network executes complementary functions from the self-biasing

mechanism: instead of feeding RF into one branch, it does this by optimizing the input matching within a specified range of power and inducing a mismatch outside that range. This is achieved whereby the key advance over the prior state-of-the-art solutions is an automatic switching approach, incoming RF power-controlled switching with no external control logic and thus no significant associated energy costs. The HEMTs in the RF signal paths are normally off, isolating their respective branches from the rest of the system when the received power in that branch is unsuitable. When the appropriate power level is approaching, the HEMTs create a conductive path to the rectification circuit. DC switches, on the other hand, perform a complementary function: they are connected in parallel with the DC outputs of the first and second branches. If the input power is appropriate to those branches, these switches remain off. When they are turned on, they short-circuit the DC loads, providing a strong mismatch for the rectifier, which reflects the incoming RF power to other branches.

The HB simulation of the HEMT in floating-gate conditions is carried out for different RF excitation levels, namely: -10, 0, and 10 dBm, to accurately predict the nonlinear behavior of the switches together with their harmonic generation. Figure 3.2 shows the static I-V curve of HEMT, where superimposed are the dynamic I-V curves under floating-gate conditions for each RF excitation level.

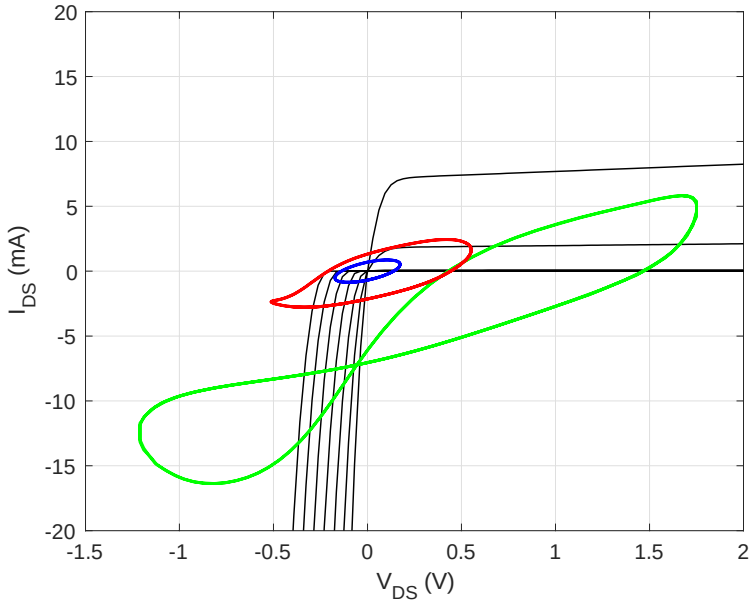

Fig. 3.2. Static $I_{DS}(V_{DS})$ curve (black) and dynamic load curves of the drain-source current for different input power levels injected at the drain terminal: -10 dBm (blue), 0 dBm (red) and 10 dBm (green) [50] © 2023 IEEE.

From Figure 3.2, it can be clearly seen that as the RF power increases, the self-polarization effects determine a significant deviation from the corresponding static value of the drain-source current (I_{DS}) dynamic behavior. To achieve high performance of the system, each rectifier is optimized together with its load. To do so, while one of the rectifier branches works, others have to be disconnected. For this purpose, two switches, TR-3 and TR-4, are connected in parallel with the DC outputs of the first and second rectifiers, respectively, as shown in Figure 3.1. Above the threshold, the gate-source voltage (V_{GS}) produces a short circuit to the ground, resulting in a strong mismatch for the rectifier.

To protect both the DC and RF switches for high input power, feedback networks have been added to the outputs of the second and third rectifiers. These networks include voltage limiters in such a way that constant and limited voltage is provided at the gate terminals of the switches. Three cascaded diodes and a parallel resistor are adopted for the limiter network. The MPR limiter is implemented using Skyworks SMS7621-079LF diodes, and the Skyworks SMS7630-079LF is chosen for the HPR limiter.

Given the design specifications, when the input power reaches 9 dBm, the HPR begins its operation, and the MPR stage turns off. However, in this condition, it could also turn off TR-3 and thus re-enable the LPR branch. The accidental on-state of the LPR will cause its failure for too high power and decrease the overall power conversion efficiency. To avoid this problem, a novel branch decoupler is adopted and its schematic is reported in Figure 3.3. It is formed by two HEMTs, TR-5 and TR-6, whose gate and drain terminals are short-circuited and driven by the outputs of the first and second limiters V_{lim1} and V_{lim2}.

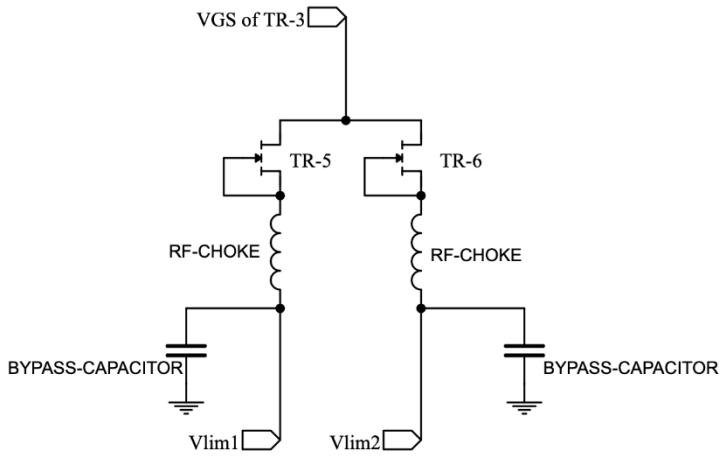

Fig. 3.3. Scheme of the proposed diverter: the gate terminals are shorted to the drain ones to create an input-voltage-controlled HEMT device [50]. © 2023 IEEE

It ensures that for an input RF power above 9 dBm, the HPR is turned on while the LPR and MPR are switched off simultaneously through the diverter. The controlled polarization at the HEMT gate terminals, which is controlled by voltage limiters, ensures that during the on state of the HPR, the MPR is turned off by forward biasing the gate of TR-4, which in turn also turns off TR-3 by short-circuiting the DC output of the MPR.

A T-topology matching network has been chosen for the LPR stage, while a double-stub structure has been adopted for the MPR and HPR stages. The overall power range is selected considering industrial or civil environments where one or more RF sources, either spontaneous or dedicated, are present because of the wireless power

supply of sensors. This choice was dictated by the aim of flattening as much as possible the RF-to-DC conversion efficiency of the rectifiers. Since the latter are nonlinear circuits, every stage is capable of ensuring an optimum performance only for a limited excitation range. Schottky diodes from Skyworks Inc. are selected for the distinct stages: SMS7630, SMS7621, and HSMS282K diodes are used for the LPR, MPR, and HPR stages, respectively. Different diodes are adopted for their different breakdown voltage, depending on the power range of the rectifying branches. In particular, the breakdown voltages are 2V, 3V, and 15 V, for the SMS7630, SMS7621, and HSMS282K, respectively. Firstly, nonlinear HB simulations of the separate three branches are carried out for the appropriate range of power of interest. This was then followed by a thorough analysis of the full system.
The power conversion efficiency (PCE) of each stage is calculated as follows:

$$PCE_{\%} = \frac{P_{out}}{P_{available}} * 100 \tag{3.1}$$

where

$$P_{out} = \frac{V_{out}^2}{R_{load}} \tag{3.2}$$

$$P_{available} = \frac{V_{av} I_{av}^*}{2} \tag{3.3}$$

and V_{out}, R_{load}, V_{av}, and I_{av} are the DC output voltage of each rectifier, the resistive load, the input voltage, and the current phasor at the fundamental frequency, respectively. Both the reflection coefficient and PCE of each branch are optimized by HB simulations to present appropriate performance only in the correct operating region, in such a way that the branches exhibit satisfactory performance only in their power range of interest. The final dimensions of the system are reported in Figure 3.4(a). The prototype, which is realized on a Rogers RO3003 substrate (thickness: 0.762 mm, ε_r = 3.00) is shown in Figure 3.4 (b). The overall dimensions of the prototype are 57 mm x 108 mm.

3.3 Validation of the Proposed Wide Dynamic Range Rectifier

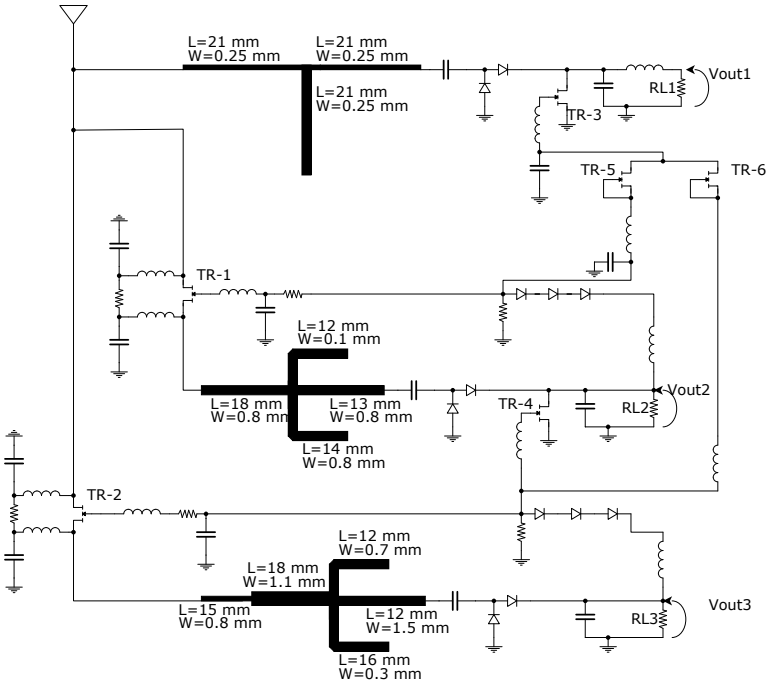

(a)

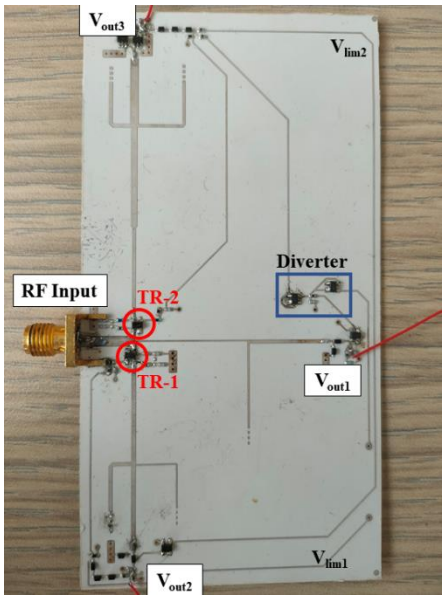

(b)

Fig. 3.4. Circuit schematic of the three-branch rectifier and (b) photograph of the fabricated prototype [50]. © 2023 IEEE

Through a VNA, the reflection coefficient observed at the input port of the system (S_{sys}) is measured for input power levels ranging from -20 dBm up to 10 dBm

(instrument upper limit); results are shown in Figure 3.5 together with the simulation carried out by HB algorithm. The reflection coefficient is below -10 dB for the most part of the measured power range. When the second branch is turned on, the S_{sys} parameter increases, but then it settles well below -10 dB after the transition between stages.

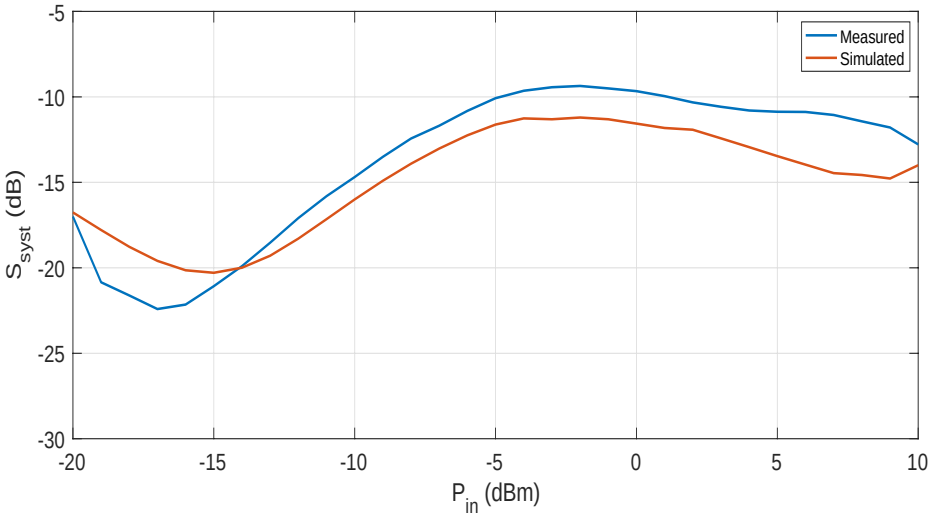

Fig. 3.5. Simulated and measured reflection coefficient of the entire system in the measured power range [50] © 2023 IEEE.

Each stage of a rectifier is characterized by measuring DC output under open-circuit voltage conditions. This was necessary for a general overview of the system and to check if conditions of optimal loading correspond to half of the open-circuit voltage. Figure 3.6 reports the measured DC open-circuit voltage (V_{OC}) at the output of each rectifier. It is important to note that even under these loading conditions, where the loads are disconnected, switching between the three rectifiers still occurs, even if a superimposition of the medium-power and high-power branches can be noticed. As the values of the embedded network lumped elements values is strongly related to the rectifiers optimization, the adoption of the open circuit load, can modify the system performance, thus enabling the third stage during the second stage operating range.

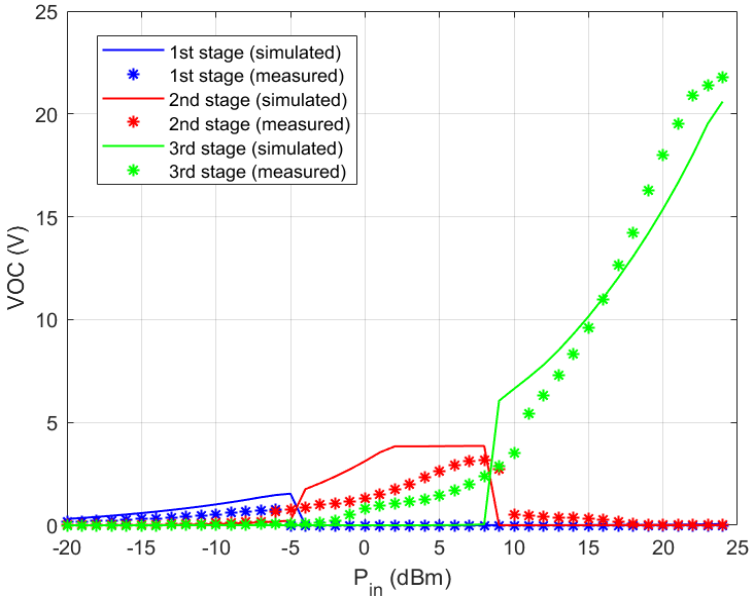

Fig. 3.6. Measured and simulated V_{OC} for each branch from -20 to 24 dBm [50] © 2023 IEEE.

Moreover, a set of measurements is performed by tuning the DC load of the LPR and MPR starting from the optimum load value identified in the optimization procedure for -10 dBm input power into the LPR and 5 dBm input power into the MPR. From measurements, it emerged that the PCE is maximum for some load values, which are R_{L1} = 4.06 kΩ for the first stage and R_{L2} = 1.48 kΩ for the second stage. The tests were conducted with input powers of -10 dBm for the LPR branch and 5 dBm for the MPR branch, obtaining PCEs of 26.5% and 38.9%, respectively. For the third stage, load tuning analysis was also performed and the optimum load value was found to be RL3 = 1.73 kΩ, which is in excellent agreement with HB-based simulations. This kind of procedure emulates the operation of a maximum power point tracker, MPPT, a baseband sub-system that is commonly included in most PMUs found in the literature.

The use of several load values for the proposed multistage rectifier is adopted in order to optimize RF-to-DC conversion efficiency with respect to single-load solutions. Moreover, this solution is the only one efficiently operating over a wide power range, starting from ultra-low power levels. In particular, 20% power conversion efficiency for -20 dBm input power was achieved, thus providing a DC output power of about 2 µW. In real IoT scenarios, the system can be closer and farther from the RF source

over time, and the seamless switching capabilities should be tested in both increasing and decreasing the available power. To this purpose, in order to verify the on/off switching capabilities of the proposed system, measurements are performed with the optimal loads mimicking a PMU placed downstream of the circuit.

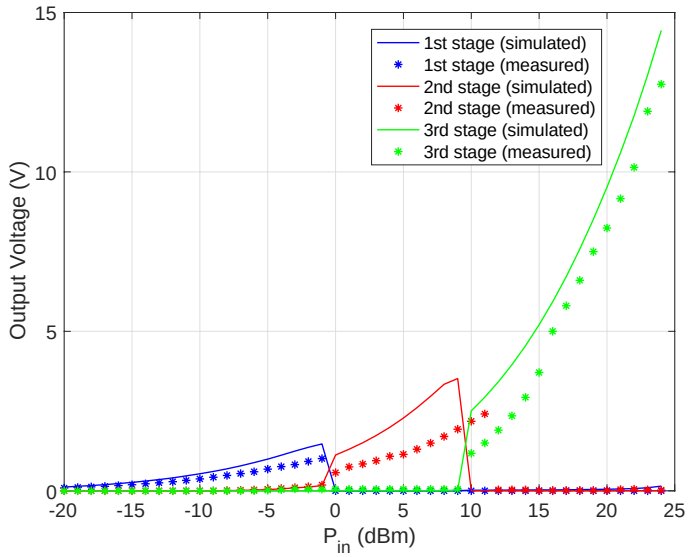

(a)

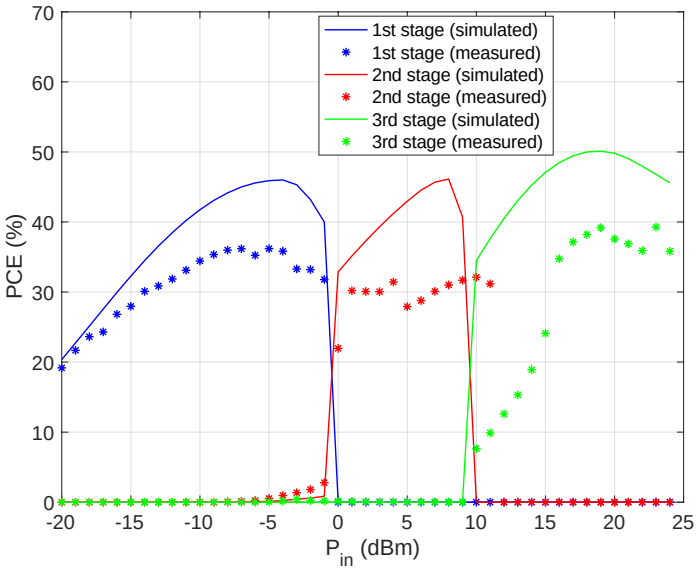

(b)

Fig. 3.7. Simulated (solid lines) and measured (dots) of the (a) output voltage V_{OUT} and (b) PCE for the three stages for input power levels ranging from -20 dBm to 24 dBm at 2.26 GHz (forward P_{in} sweep) [50] © 2023 IEEE.

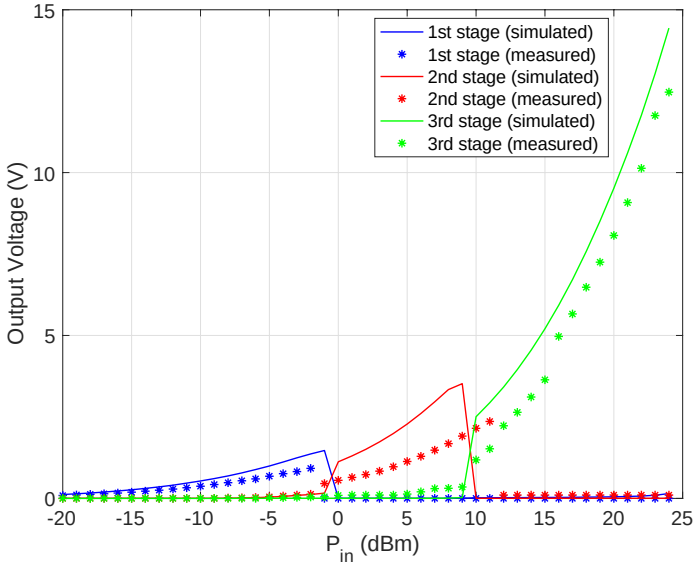

(a)

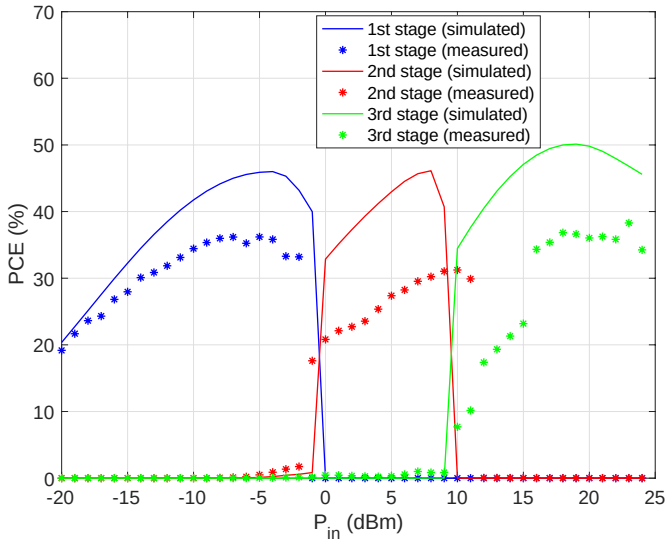

(b)

Fig. 3.8. Simulated (solid lines) and measured (dots) of the (a) output voltage V_{OUT} and (b) PCE for the three stages for input power levels ranging from -20 dBm to 24 dBm at 2.26 GHz (backward P_{in} sweep) [50] © 2023 IEEE.

Figures 3.7 and 3.8 report the measured results both in the case of increasing and decreasing available power, respectively. Both the DC voltage and the PCE are reported. Measured and simulated curve trends are in good agreement especially as

regards the switching mechanisms among rectifiers and the behaviors of both the DC voltage and the PCE%.

Some quantitative differences are found between the measured and simulated values: in particular, a frequency shift of about 200 MHz is observed, and consequently, an efficiency offset of about 10% is obtained. Such dissimilarities could be motivated by inaccuracies of the components' models available for the simulations, in particular, the models for the HEMT-based switches whose measured insertion loss resulted to be higher than the predicted one. A thorough characterization of the decoupling network subsystem is carried out and leads to excellent agreement with simulations. This is indirectly confirmed in Figure 3.7 and Figure 3.8 by observing that input power levels driving the first stage turn-off-and turn-on of the second stage is 0 dBm, while a 2-dB shift is noticed in the deactivation/activation phase of the second/third stage. On the whole, it can be claimed that this solution is a suitable candidate to become an energy harvester in IoT scenarios when a battery-less sensor node faces any occurrence of unknown available RF power. Table 3.1 summarizes a comparison among the solutions available in the literature and the outcome of this work: operating frequency, power range, power distribution techniques, and the major performance indicators are reported. The proposed solution spans a 45-dB power range that is among the largest ones for RF-to-DC converters available in the literature, especially when power levels as low as -20 dBm are addressed.

Table 3.1
Comparison of Wide Dynamic Range EH Solutions [50] © 2023 IEEE.

Work	Frequency [GHz]	RF Power Input (dBm)	Dynamic Range (dB)	20% PCE @ (dBm)	Power Distribution Technique	Need for external control
[9]	2.3-2.45	5 to 45	40	9	SPDT switches with controller and power monitor	Yes
[10]	0.9	- 4 to 25	29	-7	Adaptive matching design	No
[11]	2.4	- 10 to 30	40	-10	Adaptive matching design	No
[12]	2.4	-10 to 30	40	-10	Adaptive matching design	No
[13]	2.27	-20 to 25	45	-16	Power divider and HEMT rectifiers	No
[50]	**2.26**	**-20 to 24**	**44**	**-20**	**Adaptive matching design and passive HEMT switches**	**No**

3.4 Conclusions of the Chapter

In this chapter, a novel modular topology for wide dynamic range energy harvesting applications is presented. The system, consisting of three different branches, each optimized for a specific power range, is connected together by HEMT switches in a floating configuration. By the adoption of the concurrent use of the self-biasing effect of the RF switches and the power-selective matching network, it is possible to turn on only one branch for a specific input power level. Moreover, the design of a novel diverter for automatic decoupling is proposed. The adoption of the latter is necessary to offer a strong decoupling between the stages given the quite different input power levels of the circuit, and as a consequence to avoid the breakage of the diodes. The proposed rectifier is then fabricated and tested by a vast experimental campaign to demonstrate the functioning of the rectifier. A small deviation from the simulated performance is observed, mainly due to the nonlinear model of the HEMT switches,

which are not fully characterized, especially for high input power levels. In general, the proposed topology demonstrated its ability to work in a wide dynamic range and to be the first rectifier to offer both such a large operating power range and to work efficiently at low-input power levels.

Chapter 4

Silicon-Integrated Antennas for Energy Harvesting Applications

This chapter is based on the following publications:

S. Trovarello, M. Aldrigo, D. Masotti, M. Dragoman and A. Costanzo, "Design of an Integrated Rectenna on Multi-layer High-Resistivity Silicon Substrate," 2023 XXXVth General Assembly and Scientific Symposium of the International Union of Radio Science (URSI GASS), Sapporo, Japan, 2023,

S. Trovarello, D. Masotti, M. Aldrigo, M. Modreanu and A. Costanzo, "Design of a 24-GHz dual-polarized rectenna integrated on silicon," 2021 51st European Microwave Conference (EuMC), London, United Kingdom, 2022, pp. 684-687,

4.1 Introduction of the Chapter

The desire for low cost, elevated level of integration, and reliability have made silicon a promising substrate to implement microwave and millimeter-wave circuits. However, the silicon-based microwave circuit is plagued with its limited frequency of operation, material dispersion, high signal loss, and limited power handling capability. In this section, a novel design and fabrication technique is reported to address the limitations of common silicon integration techniques for antenna applications.

HRSi is chosen as a substrate for the antennas and circuitry thanks to CMOS compatibility. HRSi presents high bulk resistivity (>1 kΩ·cm) and high permittivity (11.7), which enhances RF circuit performance but strongly affects the radiation properties of antennas. To be compatible with circuitry and to enhance the radiation

performance of the antenna, a multilayer structure is introduced. The key idea is based on the fabrication of an inner air cavity inside the HRSi substrate, which can substantially reduce the effective dielectric permittivity of the substrate and avoid the excitation of surface waves. The antennas are first simulated using EM simulation and then fabricated. To test the performance of the designed multilayer topology, two rectennas, operating at 2.45 and 27 GHz are fabricated and tested.

This work was supported by the European Project H2020 FETPROACT- EIC-05-2019 “NANO-EH”, GA No. 951761.

4.2 Silicon-based Multilayer Substrate for Antenna Realization

For the proposed antenna-on-chip solutions, patch antennas are adopted for their radiation properties and low-profile characteristics [51]. Four-inch HRSi wafers fabricated from TOPSIL [52] are adopted for the design and realization of the prototypes.

The designed multilayer substrate is first validated by designing and fabricating a 24 GHz patch antenna. The lower layer, on which the ground metallization is deposited, is composed of a 0.525-mm-thick silicon wafer. Above this layer, two pillars made of HRSi are positioned, forming an air cavity. Finally, a silicon layer, onto which the patch's metallization is deposited, is placed on top of the pillars. An extensive simulation campaign in CST Studio Suite is carried out to obtain the optimal dimension of the pillars and the upper layer, to guarantee high performance both in terms of gain pattern and radiation efficiency. The simulation found that optimal dimensions are obtained for pillars of 100 µm, and an upper layer also of 100 µm. With these dimensions, a patch with 75% radiation efficiency was achieved. It is noteworthy to mention that concerning the only-HRSi substrate with the same height (0.725 mm), a patch antenna designed to operate at the same frequency (24 GHz) presented a maximum radiation efficiency of only 18%. This allows us to say that the proposed multilayer solution led to a 316.67% increase in terms of radiation efficiency

concerning the same antenna deposited on only-HRSi substrate, for the designed patch antenna at 24 GHz.

Figure 4.1 shows the cross-section of the proposed multi-layer silicon substrate. The layout of the patch antenna is reported in Figure 4.2 in which the CPW feeding can be observed. This design choice is dictated by the instrumentation setup at such high frequencies. In particular, for the measurement of the antenna S_{11}, the coaxial probe is needed.

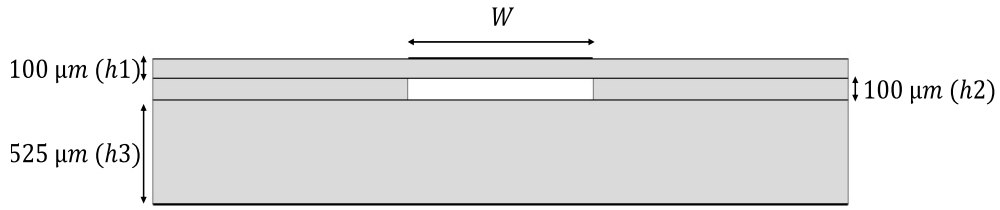

Fig. 4.1 Cross-section of the multilayer HRSi substrate adopted in the simulations (h1=h2= 0.1 mm, h3= 0.525 mm) [53] © 2021 EuMA.

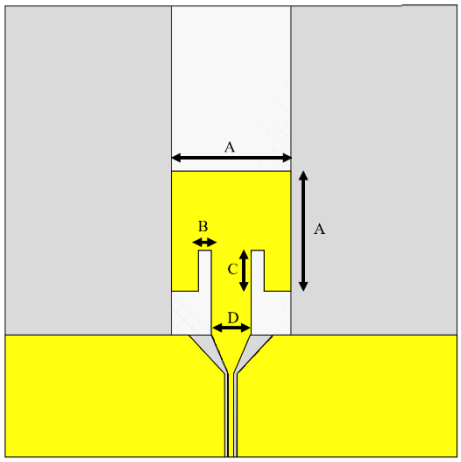

Fig. 4.2 Top view of the design antenna operating at 24 GHz and realized on the HRSi multilayer substrate. Grey area delimits the no-cavity regions, while the white one presents the 0.1 mm air-cavity. Dimensions are: A= 2.12 mm, B=0.23 mm, C=0.7 mm and D=0.68 mm. A 50-Ω CPW line is adopted for the probe mounting.

Figure 4.3 and Figure 4.4 shows the predicted reflection coefficient and gain pattern on both E- and H-plane, respectively. Simulation reported promising results. In

particular, -56 dB of S_{11} is observed at 24 GHz while for the gain pattern, a maximum of 4.82 dBi is observed from simulations. The area of the patch is about 4.58 mm^2, which assures both a miniaturized structure and good radiating performance.

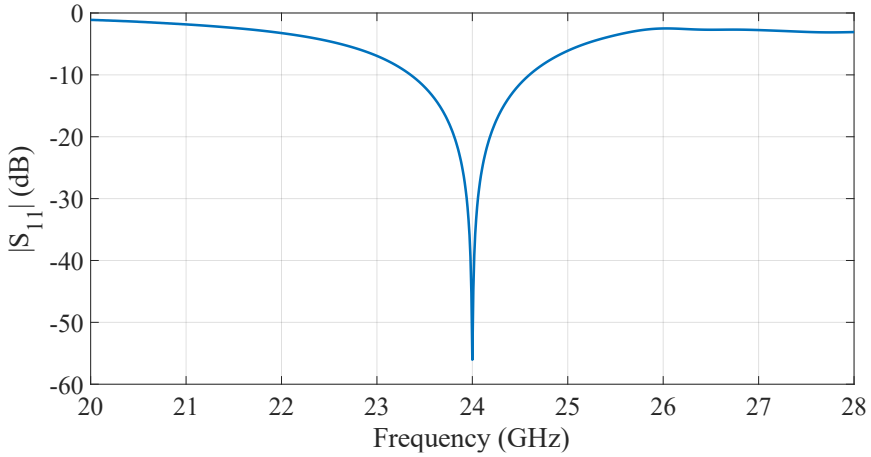

Fig. 4.3. Simulated reflection coefficient of the 24-GHz antenna. A peak of -56 dB can be observed.

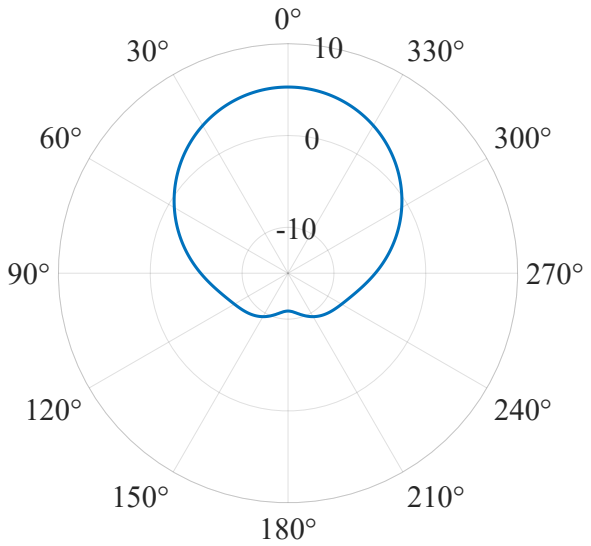

Fig. 4.4. Predicted gain pattern on the E-plane of the 24 GHz on-chip antenna.

For the etching process of the 24 GHz antenna, the goal is to etch a sufficiently deep cavity in each wafer such that after they are bonded together, a cavity of 100 μm depth remains between them. The dry etching was performed in fluorine-based plasmas with the Plasmalab System 100- ICP Deep Reactive Ion Etching (RIE) System from

Oxford Instruments, UK, where the plasma density and the ion flux to the substrate are independently controlled. A 2-µm-thick photoresist, as well as a 1.5-µm-thick layer of thermal SiO_2 in the case of the ≈525 µm Si wafer and 1-µm-thick thermal SiO_2 in the case of the ≈200 µm Si wafer, is used as masking layers. The two samples are predominantly etched with a Bosch process, which consists of two separate steps (etching and passivation) which are cycled for a set number of loops. The thickness of the Si wafers and the SiO_2 layers are measured with a TESA® DIGICO® 10 micrometer and a NanoCalc-XR refractometer, respectively, between the etching processes. Figure 4.5 shows the fabricated samples of the 24 GHz antenna and the probe connection for the experimental campaign.

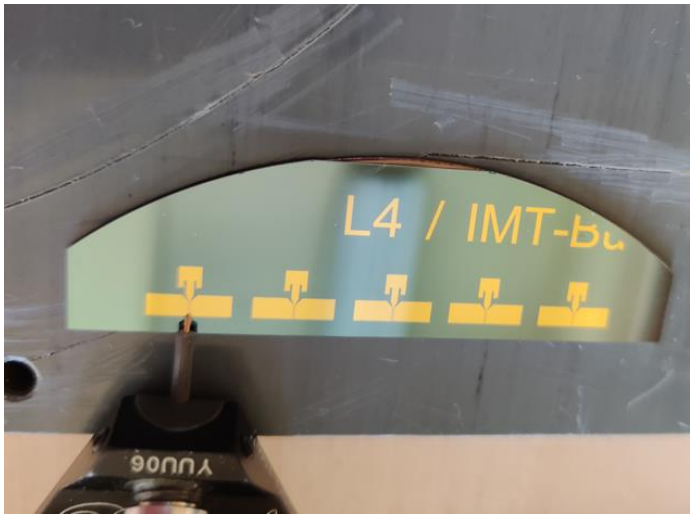

Fig. 4.5. Photo of the fabricated prototypes of the on-chip 24 GHz patch antenna.

The first measurement evaluation is dedicated to the return loss of the fabricated antennas. Figure 4.6 shows the measured patch reflection coefficient. Measurements show a large 10-dB bandwidth (from about 23 GHz to 24.6 GHz) and a 400 MHz detuning of the S_{11} peak. Figure 4.7 shows the gain pattern as a function of the frequency of the measured patch antenna. The gain values are evaluated by the Friis formula and report a maximum value of 4.05 dBi at 0° of inclination on the E-plane. Measurements report a good agreement with simulations, considering the high-

frequency measurements and the adoption of CPW probes that can provide unwanted reflections and mismatches if not perfectly aligned to the antenna CPW-input port.

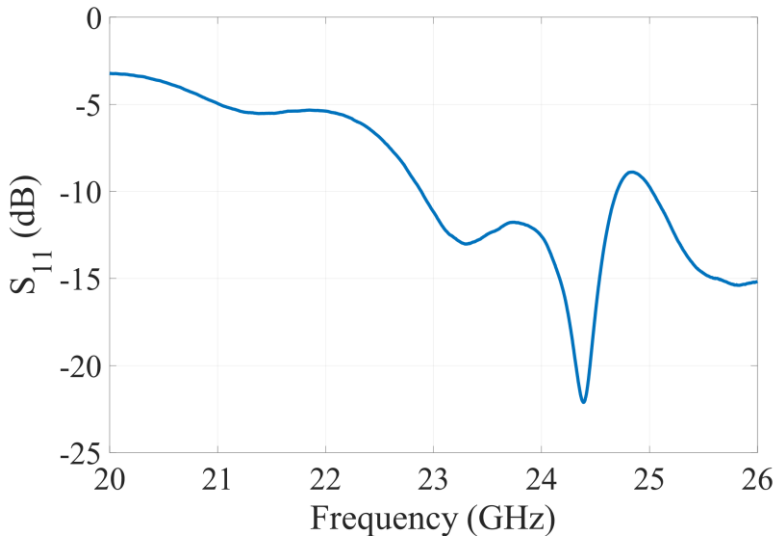

Fig. 4.6. Measured reflection coefficient of the 24 GHz antenna. A 400 MHz detuning from simulations is observed.

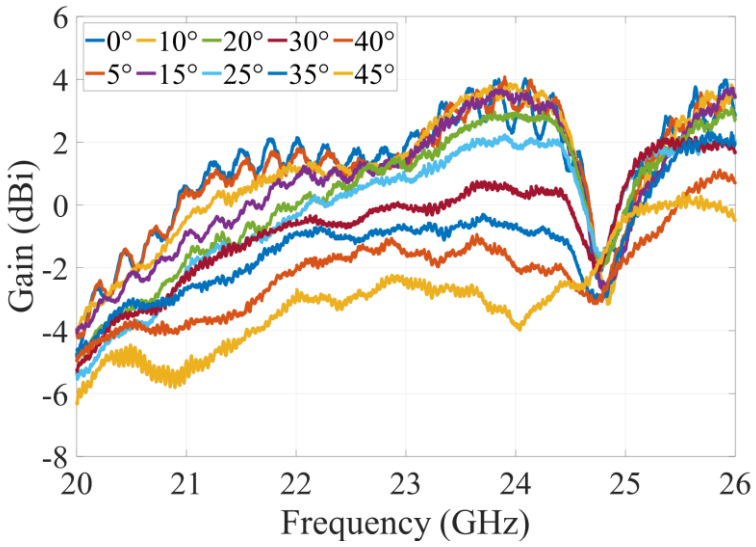

Fig. 4.7. Measured gain pattern of the 24 GHz antenna from 20 to 26 GHz. A maximum of 4.05 dBi is observed at 0° of inclination.

4.3 Design and Fabrication of Rectennas Operating at Microwaves and MmWaves Exploiting On-chip Antennas

The presented synthesized low-permittivity substrate based on HRSi is further exploited to design and realize two rectennas, operating at 2.45 GHz and 27 GHz, respectively. A preliminary study on the feasibility of the integration of the multilayer antenna and a rectifier is carried out in [54-55]. The design of the rectenna operating at 2.45 GHz is carried out by the concurrent use of an electromagnetic and a circuit simulator, where the antenna and the nonlinear circuit are simulated, respectively. For the proposed harvester, an intensive campaign of electromagnetic simulations is conducted to predict the optimal dimension of the multi-layer HRSi substrate, keeping in mind the trade-off between the radiating performance of the antenna and mechanical constraints. In particular, for the 2.45 GHz solution, two distinct wafers of 525 µm and 200 µm are exploited. The latter, etched with different thicknesses, creates a 525-µm cavity on the overall 725 µm HRSi substrate. In this way, the high radiation losses caused by silicon permittivity can be significantly reduced. Figure 4.8 shows the cross-section of the adopted HRSi multi-layer substrate.

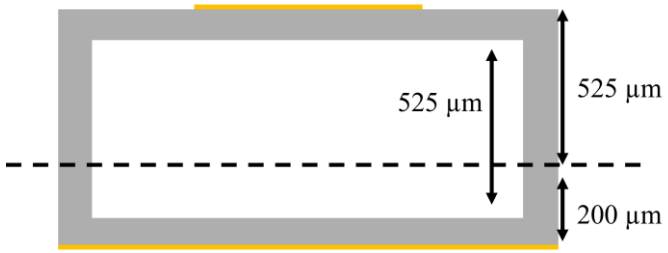

Fig. 4.8. 2.45 GHz antenna substrate cross-section.

A patch antenna is chosen for the design of the rectenna since it is widely used for this application, for being low profile, low cost, and showing high efficiency. The antenna is fed by a 50 Ω microstrip line (width: 2.5 mm) which shares the same multi-

layer substrate, and inset feeds are used for matching purposes. Electromagnetic simulations predict a good reflection coefficient at the operating frequency of -23 dB, with a maximum gain of 5.4 dBi in the broadside direction. Moreover, the synthesized low-permittivity substrate assures a high radiation efficiency of 76% for the antenna, with a 51%-increase concerning the 725 μm HRSi-substrate with no air-cavity in the center of the structure.

To achieve higher performance of the rectifying circuits, the cavity is etched only in proximity to the patch antenna, whereas for the rectifying circuit, the multilayer HRSi is left untouched. For the proposed rectenna, a voltage-doubler configuration is adopted for the rectifier. Skyworks SMS7630-079LF Schottky diodes are used for the design of the rectifier for their well-known superior performance at microwaves and low cost. To achieve the conjugate matching between the antenna and the rectifier, a microstrip matching network with an open stub is adopted.

The rectifier is designed and simulated through the HB simulator with Keysight ADS. The EM-simulated antenna is first imported in the circuit simulator (as a Touchstone file) considering also higher harmonics of the fundamental frequency. Then, nonlinear simulations are performed, and the dimensions of the matching network are optimized to achieve conjugate matching, and consequently the maximum power transfer between the antenna and the DC load. Figure 4.9 shows the predicted PCE, calculated as in Equation 12 of the 2.45 GHz RF harvester for input power levels ranging from -30 dBm to 20 dBm. A maximum efficiency of 53% is achieved for 9 dBm at the antenna.

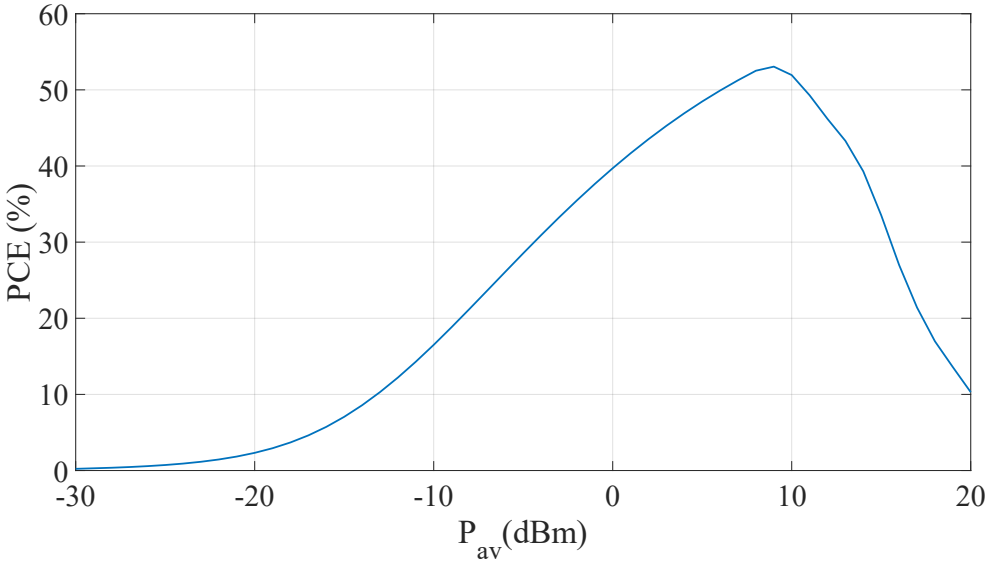

Fig. 4.9. Simulated PCE of the 2.45 GHz rectenna.

Following the procedure adopted for the 24 GHz on-chip patch antenna, the 2.45 GHz is fabricated by selectively etching two distinct wafers of 0.525 mm and 0.2 mm, respectively. The final layout of the fabricated rectenna is shown in Figure 4.10. Due to the fragility of the substrate, no via holes can be drilled. As a consequence, ground connections are realized through wire bonds between the top layer and ground layer, deposited on the entire wafer, as shown in Figure 4.11. The total area of the proposed rectenna is 7850 mm^2.

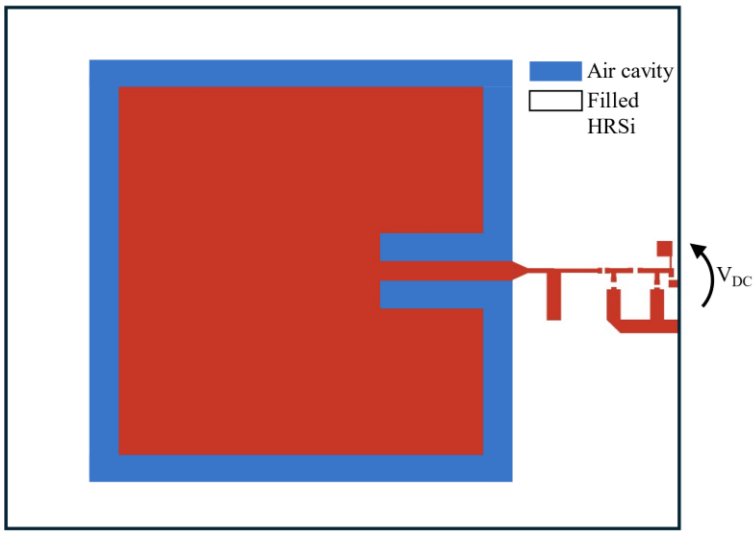

Fig. 4.10. Layout of the fabricated RF harvester operating at 2.45 GHz. The air cavity (blue) and the filled region (white) are highlighted in distinct colors.

(a) (b) (c)

Fig. 4.11. Picture of the fabricated rectenna on the (a) upper layer, (b) the bottom layer, and (c) the etched cavity.

Laboratory measurements are carried out to predict the performance of the prototype. Considering a free-space scenario, for the proposed experimental campaign the input power is swept between -30 dBm and -5 dBm. This dynamic range is constrained by the maximum output power of the RF source (25 dBm), the horn antenna gain adopted as a transmitter (10 dBi), the distance between the horn and the rectenna (1.5 m), and the gain of the patch antenna (4 dBi). Measurements of the open-circuit voltage are conducted and shown in Figure 4.12. In particular, a good agreement between measurement and simulations is found with a maximum output voltage of

about 800 mV when -5 dBm are present at the receiving antenna. Measurements demonstrate the validity of the multilayer HRSi solution both in simulations and measurements. Indeed, by further enlarging the air cavity both in height and in width an increment of the PCE is possible. Anyway, a trade-off between fragility, size and performance needs to be established in the design phase.

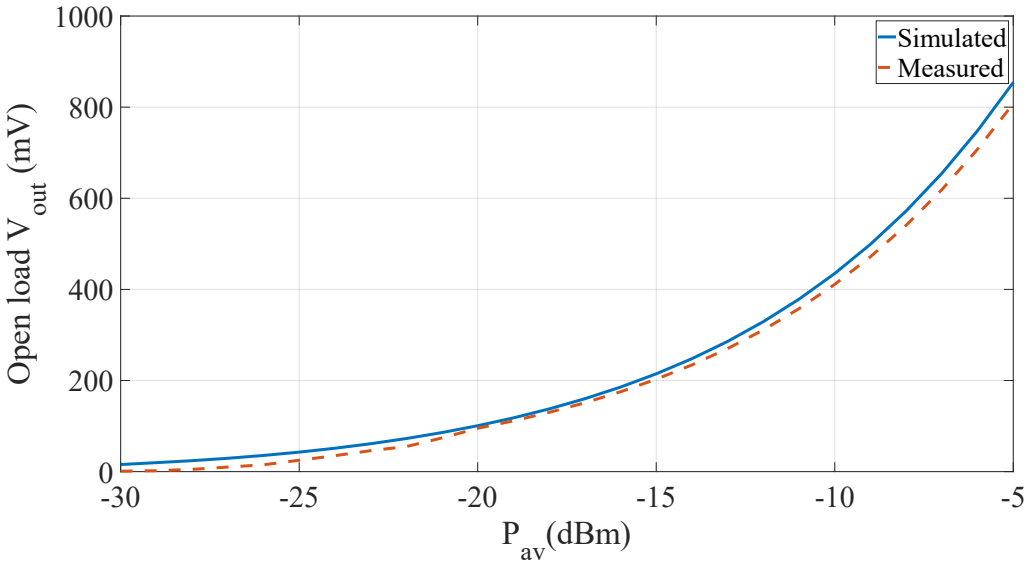

Fig. 4.12. Simulated and measured open circuit voltage of the 2.45 GHz rectenna.

A prototype working in the 27 GHz band is also designed to validate the proposed HRSi multilayer concept also for mmWave applications. This particular operating frequency is chosen due to the limitation of the available instrumentation in the laboratory. As for the 2.45 GHz rectenna, an investigation of the best dimension of the air cavity is conducted. Indeed, for higher frequencies, the optimal cross-section is downscaled. For this reason, 0.525 mm wafers are not taken into consideration. By means of EM simulation, the optimal cross-section that offers a good trade-off between mechanical stability and performance is found. By adopting two HRSi wafers of 0.2-mm-thickness each, and by removing 0.1 mm of material from both the wafers, a 0.2-mm-thick cavity is achieved, as shown in Figure 4.13.

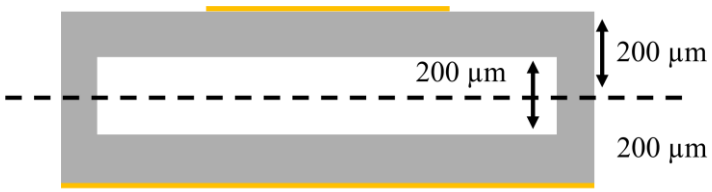

Fig. 4.13. 27 GHz antenna substrate cross-section.

With this solution, EM-simulations report a peak of the reflection coefficient of -36 dB at 27 GHz and a simulated gain of 4.6 dBi. Indeed, as the operating frequency increases, the width of the cavity also decreases, together with the thickness. As for the 2.45 GHz solution, the rectifier is designed on the filled HRSi substrate (in the case of the 27 GHz rectenna presents a 0.4 mm thickness), due to the high dielectric permittivity and low losses, for a high miniaturization of the device.

The performance of the rectenna is calculated as in Equations 3.1 to 3.3, where NL-EM co-simulations are performed, by importing the EM simulated patch antenna in ADS Keysight. Figure 4.14 shows the simulated PCE as a function of the input power at the antenna. A maximum of 48.5 % of PCE is found for an input power level equal to 13 dBm.

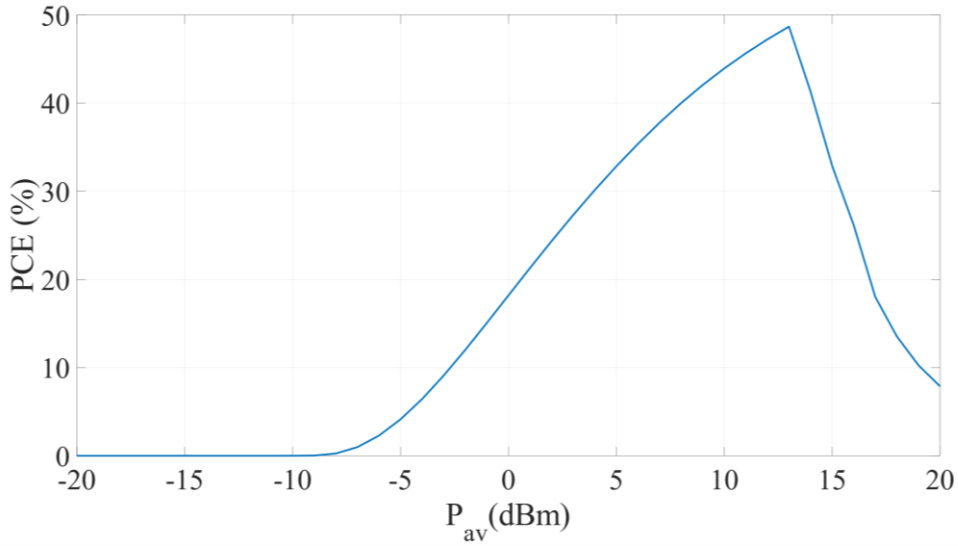

Fig. 4.14. Simulated PCE of the 27 GHz rectenna.

For the proposed rectenna, a voltage-doubler configuration is adopted for the rectifier design. At mmWave frequencies, the propagation of the fundamental tone and its harmonics to the output becomes a key factor limiting PCE, as it approaches the diode's cut-off frequency. Most commercially available silicon Schottky diodes have a junction cut-off frequency of around 20 GHz, which can be further reduced by packaging and mounting parasitic. As a result, Gallium Arsenide (GaAs) diodes, capable of switching beyond 100 GHz, are typically preferred for rectennas operating above 20 GHz. In particular, for the 27 GHz harvester, GaAs diodes from MACOM (MA4E1317) are adopted. To achieve the conjugate matching between the antenna and the rectifier, a microstrip matching network with an open stub is adopted. The final layout of the rectenna is shown in Figure 4.14, where the air cavity and the filled region are highlighted with distinct colors. The adoption of a selective etching of the air cavity ensures good miniaturization of the device. In particular, the occupied area of the 27 GHz rectenna is only 195 mm^2.

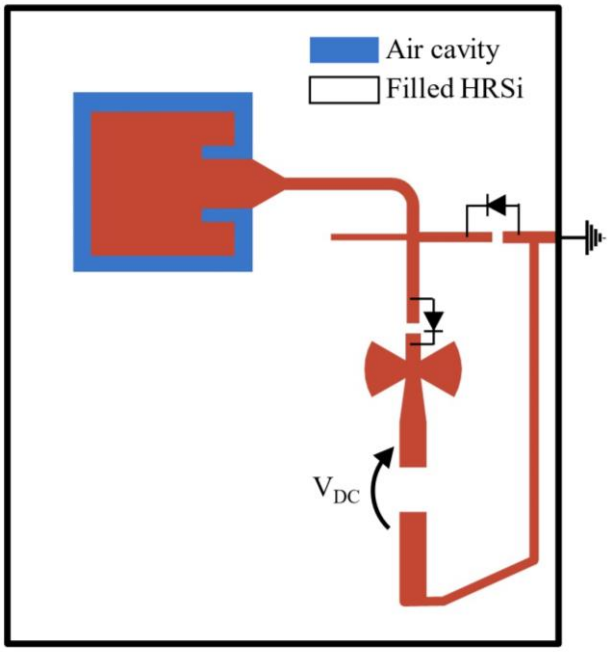

Fig. 4.14. Layout of the fabricated RF harvester operating at 27 GHz. The air cavity (blue) and the filled region (white) are highlighted in distinct colors.

Photos of the wafer with 28 demos and zoom on the one adopted for the measurements are shown in Figures 4.15. Experimental measurements are conducted analogously as to the 2.45 GHz, where a horn antenna is adopted as a transmitter. Given the operating frequency, the maximum RF source output power, and the gain of both antennas, the available power is swept from -20 dBm up to 0 dBm. A photo of the measurement setup is reported in Figure 4.16(a), while measurements of the DC open voltage are reported in Figure 4.16(b). A good agreement between simulation and measurement with a maximum of 830 mV was detected for an available power equal to 0 dBm at the antenna.

(a) (b)

Fig. 4.15. Photos of the (a) wafer with the 28 fabricated samples, and (b) zoom on the one adopted for the measurements.

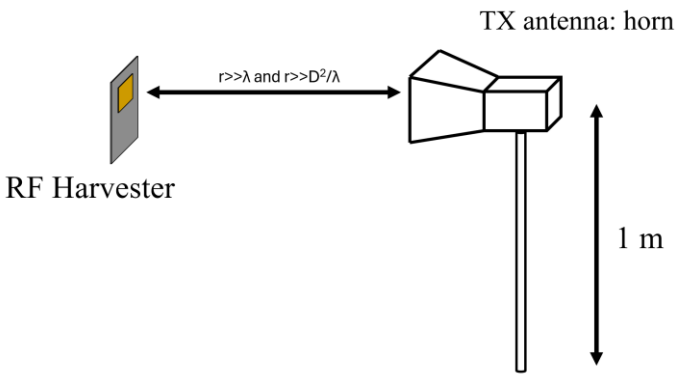

(a)

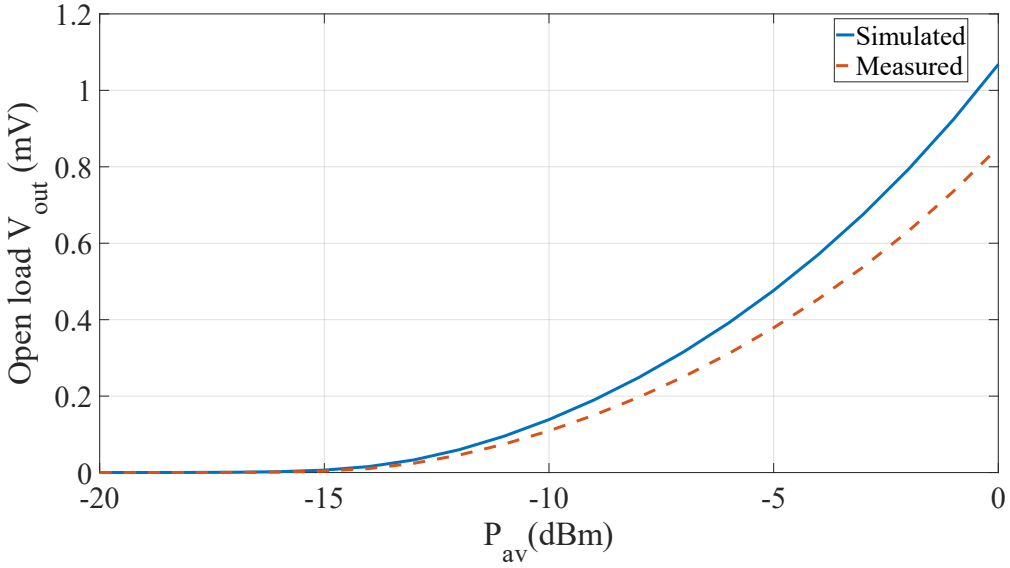

(b)

Fig. 4.16. (a) Rendering of the measurement setup, and (b) simulated vs measured open circuit voltage of the design 27 GHz rectenna.

Observing the obtained results, a high input power threshold is seen when the mmWave rectenna is adopted. This is probably due to the different fabrication technology and materials of the two rectifiers, and in particular due to the Silicon and GaAs diodes. Moreover, a higher discrepancy between measurement and simulations is found for the 27 GHz. Multiple factors can be responsible for this, in particular the circuital diode model for the MA4E1317 diode and the wire bonding for the ground connections. As anticipated for the 2.45 GHz solution, the drilling of via holes is not feasible in the HRSi substrate. For this reason, a wire connection is needed to shorten the ground metal plate on the bottom layer and shunt the diode. The connection, which cannot be predicted in a precise manner in terms of dimension, length, and soldering quality, can affect the connection, and create inductive parasitic which can dramatically decrease the overall performance of the rectenna.

4.4 Conclusion of the Chapter

In this chapter, a novel multilayer substrate based on HRSi wafer is proposed. By selectively etching the silicon wafer it is possible to create a low-permittivity cavity which is demonstrated to largely enhance the radiation performance of patch antennas deposited on silicon. A first batch of antennas, operating at 24 GHz is fabricated and tested, demonstrating good performance, overcoming the limitations of the state-of-the-art solution, where mechanical unstable solutions are reported. The multilayer concept is further validated by the fabrication of several antennas and the adoption of them in microwaves and mmWave circuits such as rectifiers operating at 2.45 GHz and 27 GHz, demonstrating the validity of the proposed technology. In particular, two different multilayer substrates are reported, each one specific for the frequency of interest. The selective etching is adopted for both the antennas, while the rectifying circuit is deposited in the filled region, for a higher miniaturization. The rectennas are then fabricated and tested in the free-space scenario, where the DC output voltage is observed. The comparison with the simulations demonstrates promising results, and the quality of the project.

Chapter 5

Non-Invasive Microwave Sensing System for Biological Monitoring

This chapter is based on the following publications:

S. Trovarello, O. Afif, A. Di Florio Di Renzo, D. Masotti, M. Tartagni,

and A. Costanzo, "A non-invasive, machine learning assisted skin hydration microwave sensor," in 54th European Microwave Conference (EuMC), Paris, France, Sep. 2024. © 2024 EuMA.

A. Di Florio Di Renzo et al., "A Stand-Alone Moisture Content Sensor Based on a Loaded Self-Oscillating Antenna," 2024 IEEE/MTT-S International Microwave Symposium - IMS 2024, Washington, DC, USA, 2024, pp. 284-287, © 2024 IEEE.

5.1 Introduction of the Chapter

In this chapter, the design of two microwave-based sensors for hydration monitoring is proposed. In particular, two different approaches for sensor design and applications are reported. Firstly, a non-invasive skin hydration sensor is proposed. The sensor, operating in the reactive near-field region, is assisted by a machine learning (ML) algorithm, for real-time detection. The near-field sensor is firstly designed by means of EM simulations and then fabricated by adopting a low-cost fabrication process. A large in-vivo experimental campaign is adopted to store a large dataset for the machine learning algorithm. The ML algorithm is then tested with the stored dataset, demonstrating high accuracy in the recognition of the skin hydration class.

Then, a moisture content sensor, for agriculture applications is reported. The latter, consisting of a self-oscillating antenna, loaded with a tree trunk in different moisture conditions, is able to detect the moisture levels by only observing the

nonlinear DC states of the active device. An extensive design procedure of the self-oscillating antenna is proposed, including the steady-state regime under different wood hydration levels.

5.2 Non-Invasive Skin Hydration Sensors Assisted by Statistical Machine Learning

This section is dedicated to the design of a resonator-based skin hydration sensor using a low-cost CSRR in the 2.4 GHz band which includes integration with ML models. The main goal of the research activity is to prove the integration of the results of a classification model algorithm with a low-cost, non-invasive, portable, and wearable microwave sensor probe made with CSRR. The algorithm is designed on a small dataset basis, performing a statistical analysis that will predict the status of hydration directly in the human body from skin-sensing measures. The microwave sensor operates using a CSRR in the 2.4 GHz industrial, scientific, and medical (ISM) band. Its working principle relies on the near-field interaction between the fringing electric field and the skin under varying hydration conditions. The interaction with the skin alters the electromagnetic field lines, which in turn affects the resonance frequency of the loaded CSRR, as it modifies the equivalent capacitance of the LC circuit accordingly.

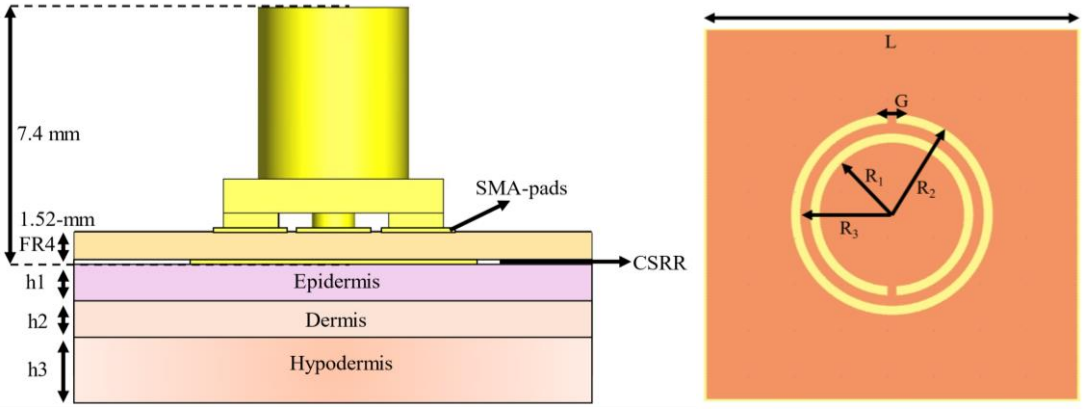

(a) (b)

Fig. 5.1. Lateral (a), and bottom (b) view of the proposed CSRR-based skin hydration sensor. h1, h2, and h3 are set to 1 mm, 1 mm, and 4 mm respectively [58] © 2024 EuMA.

Compared to the traditional split-resonator configuration, the complementary design can easily be implemented on an SMA connector. Indeed, the wide ground of the resonator allows an easy connection to the outer nut of the RF connector, while the hot wire is directly connected to the inner part of the resonator. The resonator is implemented on a low-cost FR4-PCB (ε_r=4.3, tanδ=0.025). Five via holes are located at the five pin positions of the SMA connector and are utilized for the connection between the top and bottom parts of the 1.52-mm-thick PCB. Therefore, high mechanical strength can be achieved, and the fabrication complexity of the resonator is relaxed. Figures 5.1 present the view of the designed resonator in both the lateral and bottom side, along with its geometric dimensions (G = 0.2 mm, R1 = 1.5 mm, R2 = 2.1 mm, R3 = 1.9 mm and L = 8 mm). An 8-µm polyethylene terephthalate layer is placed under the sensor to prevent direct contact between the metal layer and skin and, hence the sensor is taken as electrode-less. Human skin is electromagnetically modeled by three layers: epidermis, dermis, and hypodermis, with typical thickness and electrical properties from [56-57]. The design of the CSRR-based sensor is carried out by means of full-wave simulations in CST Studio Suite.

First, a preliminary estimation of skin penetration depth is done through electromagnetic simulation, highlighting the E-field density in the presence of CSRR. For comparison, similar calculations have been carried out for a patch antenna

operating at the same frequency. The skin-loaded patch antenna yields a much larger depth of penetration of the electric field compared to the CSRR. The fact that from 6 mm onwards the electric field for the patch antenna decreases only by 20%, enables the field to penetrate the biological tissues under the skin layer. For this reason, a radiative element is not feasible for low-depth sensing.

Moreover, the adoption of a patch antenna reduces the sensing capability of the resonator since most of the water content resides in the most superficial area of the skin. For this reason, a patch antenna, and in general a resonator operating in the near-field radiative region, are not suitable for skin sensing applications. The CSRR loaded with skin shows an electric field intensity reduction of 32% and 65% at 1- and 2-mm-depth, respectively. Hence, it is possible to confirm the choice of a CSRR operating in the non-radiative near-field region.

Figure 5.2 illustrates the simulated reflection coefficients at the SMA port of the loaded CSRR for three hydration levels: hydrated, normal hydrated, and dehydrated skin. The electromagnetic simulations indicate that changes in skin permittivity significantly impact the sensitivity of the resonator, thereby affecting variations in hydration states. For normal hydrated skin, a return loss of 17.6 dB is observed at 2060 MHz, while the peaks for hydrated and dehydrated skin shift to 2024 MHz and 2116 MHz, respectively.

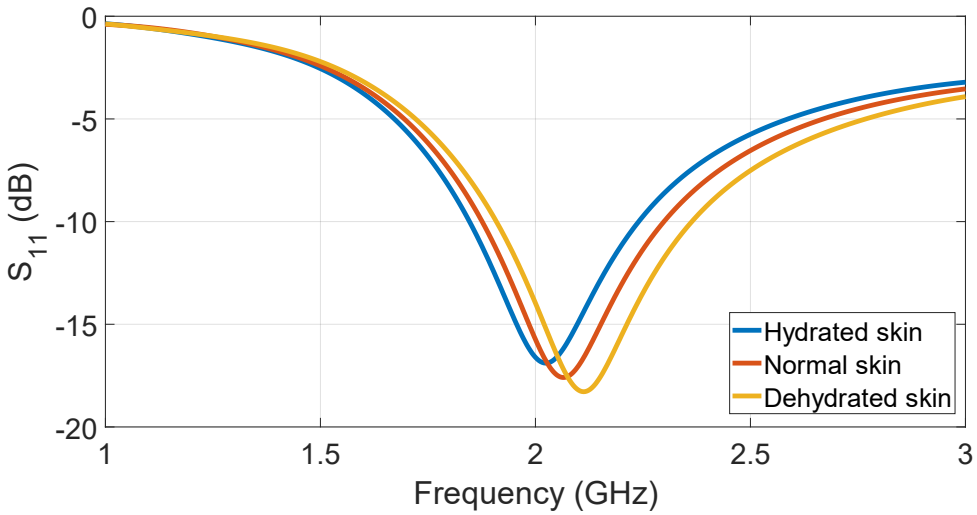

Fig. 5.2. Predicted reflection coefficient calculated at the SMA connector input port. A 92-MHz frequency shift is observed between the lowest and highest level of hydration simulated [58] © 2024 EuMA.

Figures 5.3 show the fabricated CSRR on the FR4 substrate. The total dimensions of the prototype are 1.4 cm x 1.4 cm x 0.74 cm.

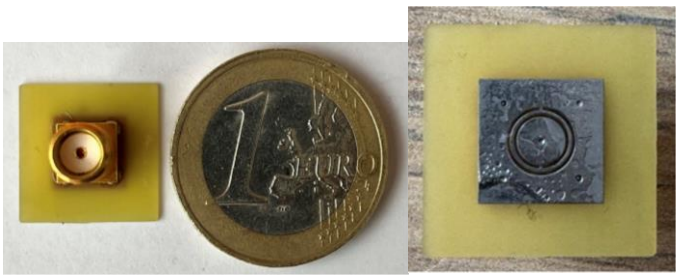

(a) (b)

Fig. 5.3. Top-view (a), and bottom-view (b) of the fabricated resonator for skin hydration sensing purposes [58] © 2024 EuMA.

Systematic spectral acquisitions carried out twice a day for several anatomic areas in the human body, are carried out. The measurements are performed using ad-hoc hardware made up of a low-cost nanoVNA that is controlled via a Raspberry Pi connected to the CSRR, thus allowing measurement in any body location [59]. The volunteer fasted for 12 hours, with no solid or liquid food and drink; the first measurement set is performed after 6 hours of fasting, t_1, and the second set after 14

hours, t_2, which means that almost 8 hours are between the two sets of measurements. This experimental campaign is repeated over two days. Investigations concern the degree of hydration within the thenar eminence, the proximal wrist crease of one hand, and the cheek. Such selection of the anatomical site provides the possibility to investigate the dynamic properties of skin hydration. In each of the selected sites, 2 × **N** measurements (**N** > 3) are carried out. Each acquisition takes about one minute in order to be deeply examined in spectral data for a comprehensive analysis. A classification model is developed able to classify hydration conditions from the amplitude of the reflection coefficient measured using a multivariate statistical analysis [60-61] for model generation. For the proposed scenario, a SIMulated Correlation Algorithm (SIMCA) is adopted. Model creation, cross-validation, and validation are the three steps involved in the process as in Figure 5.4.

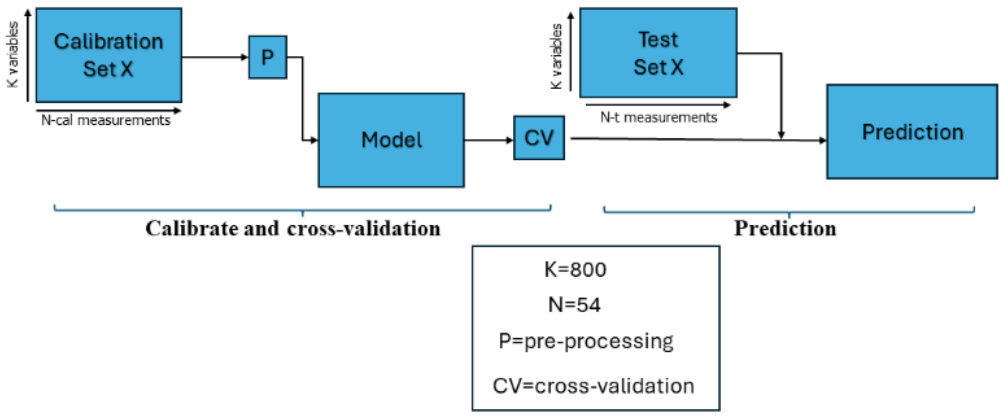

Fig. 5.4. Representation of the workflow used in the SIMCA algorithm [58] © 2024 EuMA.

Measurements from the selected areas on the volunteer body are adopted for the calibration sets. These independent variables are collected into a **K**=800 (spectrum points) times **N**=54 (measurements) matrix, which is called the dataset of **X**. This complete dataset is split into a training and test dataset where 80% was assigned for calibration, and the remaining portion for testing. This was done randomly and evenly distributed within all classes. These spectra are classified under various classes, and the predicted class labels are matched with the actual ones. A confusion matrix is thus produced, where each row represents the actual class of the measured results and

columns represent the predicted classification, besides several characterization parameters.

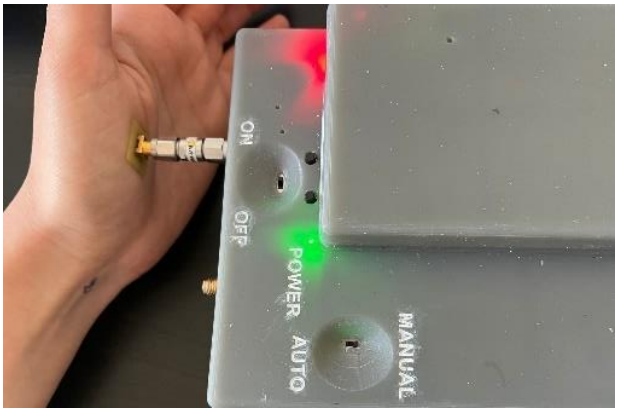

(a)

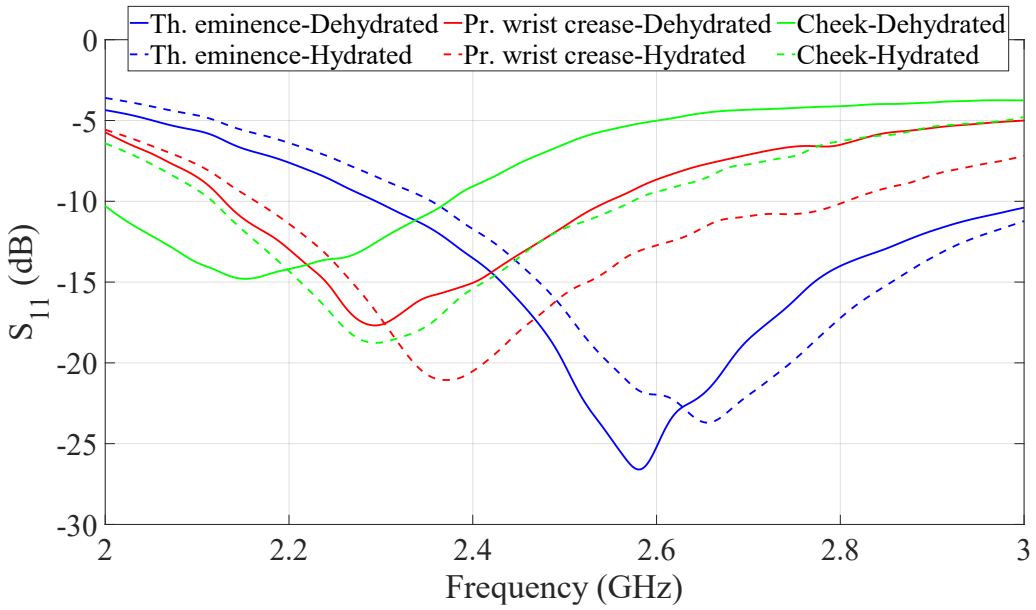

(b)

Fig. 5.5. (a) Measurement setup carried out with the ad-hoc acquiring system, and (b) measured reflection coefficient at t_1 and t_2 in different body positions (thenar eminence, proximal wrist creases, and cheek) [58] © 2024 EuMA.

Figures 5.5 show the measurement setup and the obtained spectra in the different time intervals and body positions. The measurements indicate that there is a significant frequency shift in all three tested body regions. It can be seen that the resonator's

resonant frequency has increased according to the measurements taken at t_1 and t_2. This proved to be a frequency shift of 75 MHz for the thenar eminence, 90 MHz for the proximal wrist crease, and 143 MHz for the cheek. The trend thus found forms a very promising basis for the development of statistical models. These measurements confirm the simulated reflection coefficients due to hydration obtained in Figure 40. Therefore, one can establish that t_1 is the state of skin hydration while t_2 is the dehydrated state of skin.

However, noise in both machine and human errors can affect the spectra measurements. These spectra are pre-processed by removing the outlier data before using them as inputs in the SIMCA analysis. This involved auto-scaling and the Savitsky-Golay preprocessing of the **X** dataset. It involves centering and scaling of each variable to unit standard deviation. Polynomial transformation and cross terms were used to model nonlinear trends in the data. In both the cross-validation and calibration, two kinds of errors can be defined: the Root Mean Square Error of Cross-Validation (RMSECV) and the Root Mean Square Error of Calibration (RMSEC). For t_1, the respective values are 0.3908 for RMSECV and 0.2397 for RMSEC, while for the t_2 condition, the RMSECV comes out to be 0.4359 with an RMSEC of 0.2511.

Table 5.1 shows the confusion matrix, which presents a comprehensive model performance view in predicting the classes of hydration levels at t_1 and t_2. The matrix allows for a detailed comparison between predicted and actual values to be made, laying out both areas of accuracy and discrepancy. This reflects, however, that the diagonal should be maximized to identify skin hydration classes with the model for the true value of accurate predictions. For t_1, all 27 instances were correctly predicted, which accounts for the perfect performance of the model regarding that time point. Similarly, at t_2, 24 instances were rightly predicted, which shows high accuracy. The off-diagonal values expose misclassifications; at t_1, there were no instances classified incorrectly, which again shows perfection regarding the accuracy of the model for that time. While at the time t_2, 3 instances were wrongfully predicted as t_1. This could be an indication that the performance of the model could be improved with more

measurements. Overall, the performance of the model describes satisfactory results despite using a small dataset, N=54, and least misclassification.

Further, in Table 5.2 below are some of the statistical parameters derived from the SIMCA model.

Table 5.1

Confusion Matrix

	Predicted hydrated in t_1	**Predicted hydrated in t_2**
Actual hydration in t_1	27	0
Actual hydration in t_2	3	24
Unsigned class	0	0

Table 5.2

Statistical Parameters Calculated from the Confusion Matrix

Class	**Err**	**F1**
Hydration in t_1	0.25926	0.80412
Hydration in t_2	0.25926	0.75000

The most important achievement is the low misclassification error (Err) along with the high F1 score. In particular, Err quantifies the proportion of incorrect predictions made by a classification model. It is an important indicator of a model's overall performance, providing a clear view of how often the model misclassifies data points. The error Rate can be calculated using the following formula:

$$Err = \frac{FP+FN}{TP+TN+FP+FN} \tag{5.1}$$

where FP (False Positives) are the instances incorrectly classified as positive, FN (False Negatives are instances incorrectly classified as negative, TP (True Positives) are instances correctly classified as positive, and TN (True Negatives) are the instances correctly classified as negative. A high error rate indicates that the model is making

many mistakes and is performing poorly in its classification task. Conversely, a low error rate indicates that the model is classifying most instances correctly. The ERR ranges from 0 to 1, where 0 indicates perfect accuracy (no misclassifications) and 1 indicates complete failure (all predictions are incorrect). The F1 score is a more nuanced metric that combines precision and recall, providing a single score that balances both. This metric is particularly valuable when dealing with unbalanced classes, where one class significantly outweighs the other. The F1 Score is calculated using the following formula:

$$F1 = 2 \times \frac{Precision \times Recall}{Precision + Recall} \tag{5.2}$$

where the precision is the proportion of positive predictions that are correct, calculated as the ratio between the true positives and the sum of the true positives and false positives. On the other hand, the recall is calculated as the radio between the true positives and the sum of true positives and false negatives.

The F1 score ranges from 0 to 1, with a score of 1 representing perfect precision and recall. It is particularly useful in unbalanced class scenarios, as it provides a more balanced view of model performance than accuracy alone. A high F1 score indicates that the model effectively balances false positives and false negatives, demonstrating competence in both detecting positive cases and avoiding false alarms. The F1 Score also ranges from 0 to 1. A score of 1 signifies perfect precision and recall, meaning the model accurately identifies all positive cases without any false positives. A score of 0 indicates the worst performance, where no positive cases are correctly identified.

This actually reflects strong classification performance, which-in spite of a limited dataset-demonstrates accuracy along with a good balance between precision and sensitivity of the two classes. Since the offline computation of the predictive model requires low computation, it can be easily implemented within embedded and/or autonomous systems together with the CSRR, the VNA, and other components. Overall, this machine learning algorithm enhances data processing in feature extraction

and dimensionality reduction to identify data trends and relationships. In addition, the capability to detect patterns and anomalies as well as providing decision support for interpretation will lead to much better decision-making.

5.3 Moisture Content Sensor Based On the Monitoring of the DC-States of a Self-Oscillating Antenna

As anticipated in Chapter 1, moisture content detectors based on microwave circuits find a wide circle of applications due to their high accuracy, low cost of production, and ease of production. The ability of electromagnetic waves to penetrate materials allows for the gathering of key information without destroying the samples, which is positioning microwave sensors as one of the hot topics of current research. Its main disadvantage relies on the dependence of bulk instruments, which are inappropriate in the context of IoT applications. The proposed device has tried to overcome these challenges based on the concept presented in [62]: it is a compact, lightweight, and stand-alone system, as depicted from the schematic block diagram in Figure 5.6.

The system consists of a self-oscillating antenna operating at 2.4 GHz, which is put in direct contact with the trunk of a tree, for detecting moisture content therein. The principle of operation depends on nonlinear dependences of steady-state regimes of an oscillator for different conditions of loading on its DC operating point. An investigation of the nonlinear oscillator steady states concerning different loading cases is performed, showing how RF steady-state regimes and the corresponding static DC bias conditions change with moisture variation inducing changes in the antenna's dispersive behavior. Initial NL and EM simulations of the overall system [63-64] have been performed characterizing antenna under loaded and unloaded conditions over a wide frequency range including all relevant oscillator harmonics. For sensing applications, this work proposes to use the loaded antenna directly as the dispersive load in the

oscillator feedback network instead of a conventional resonator. This antenna approach not only relaxes the oscillation conditions but also enhances the penetration of the oscillator's output RF power into the MUT. Extensive experimental tests show that the self-oscillating antenna stays distinguishable under varying loading (moisture) conditions solely from the observation of static drain current.

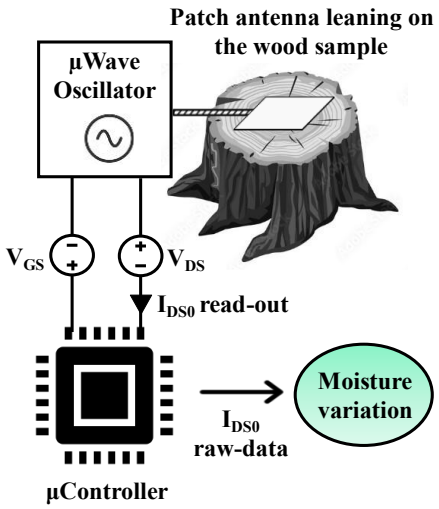

Figure 5.6: Overview of the proposed stand-alone moisture sensor detector. A microwave oscillator is loaded by a patch antenna in contact with the wood sample. The varying dispersive behavior of the load under different wood moisture conditions modifies the steady-state oscillatory regime of the self-oscillating loaded antenna.

The sensing element consists of an aperture-coupled patch antenna designed to resonate in the 2.4-GHz band. Electromagnetic simulations are performed in CST Studio Suite: A substrate of Isola FR408HR with ε_r=3.68 and tanδ=0.0092, 1.52 mm thick is used to present a 50-Ω input impedance at resonance for an area of 60 x 60 mm² dimensions of the finalized antenna. The aperture-coupled feeding technique allows for obtaining a double-layer configuration: the resonating antenna is placed on the upper layer, being in contact with the wood, while the active circuit will be placed on the lower layer and not interact with the sample. The antenna and the operating frequency band of the system are selected from preliminary simulations of the circuit that are not shown for brevity. These simulations show that the 2.4 GHz band provides

a particularly good compromise between circuit miniaturization and E-field strength in several millimeters of the wood sample. This frequency band is also widely adopted in RF architectures.

A 0.6-mm Rogers RO4360G2 substrate (ε_r=6.15) is considered for a microstrip oscillator in harmonic balance simulations. The active device selected for the above design is a depletion mode Pseudomorphic Highly Electron Mobility Transistor (pHEMT) SAV-331 from Mini-Circuits. Figure 5.7(a) shows the circuit schematic: the pHEMT is embedded in a microstrip circuit including a stub matching network connected to the drain port and two capacitive stubs connected to source terminals that take part of the feedback network with an inductive stub placed at the gate terminal. The design variables are the widths and lengths of the microstrip lines, the external gate, and drain biases. Frequency tuning can be obtained using open stubs between the gate and source, or by adjusting the gate bias. The output microstrip line is adopted to feed the EM-designed patch antenna, which is used as the dispersive load of the oscillator, as explained in the previous subsection. Attached to the wood trunk, the complex load varies indeed with its moisture content. The assembly layout is shown in Figure 5.7(b), while the perspective view of the entire system is given in Figure 5.7(c). From the combined use of HB simulations in ADS Keysight and EM simulations, the design of the steady-state oscillatory regimes, accounting for the dispersive loads at the relevant harmonics, is enabled.

The adopted patch antenna loaded with the wood sample, of dimension 95x95x150 mm^3, is measured in different moisture content conditions to better represent the dispersive behavior of the load. For the presented analysis, the wood sample is initially immersed in water for three days. After the first day, the patch antenna loaded with the tree sample is measured via a VNA in nine different moisture content conditions, including $t=t_0$ for the fully saturated sample, and $t=t_8$ for the completely dried sample.

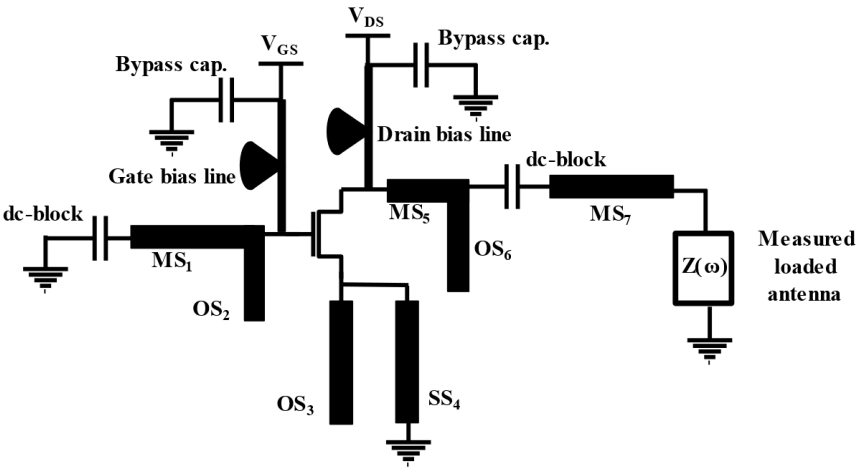

(a)

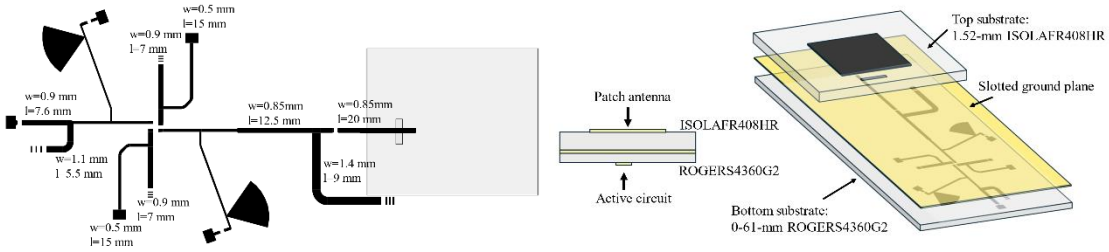

(b) (c)

Fig. 5.7. (a) Self-oscillating circuit, (b) layout view, and (c) 3D view of the proposed system. The antenna, placed on the top substrate, is aperture-coupled to the active circuit in the bottom substrate.

At each time interval, the complex input impedance of the antenna loaded by the fir wood sample is measured via a VNA. That would allow gathering a set of data corresponding to the scattering parameters that are going to be introduced to the NL-EM co-simulations. The measurements are performed not only on the fundamental frequency band, but the higher harmonics have also been extended up to 20 GHz. Figures 5.8 depict the measured real and imaginary parts of the antenna input impedance loaded by the wood sample for several values of the moisture content.

For clarity, only representative five curves are shown. It is important to note that, in unloaded conditions and for all the tested moisture states, the input impedance significantly differs from the ideal value of 50 + j0 Ω, both at the resonance frequency of 2.45 GHz and at higher harmonics: at $t = t_0$, $Z = 301 + j227.5$ Ω while at $t = t_8$, it is

72.8 + j100 Ω. This finding corroborates the previously simulated sensing capabilities of the loaded patch antenna for cm-thick materials such as tree trunks.

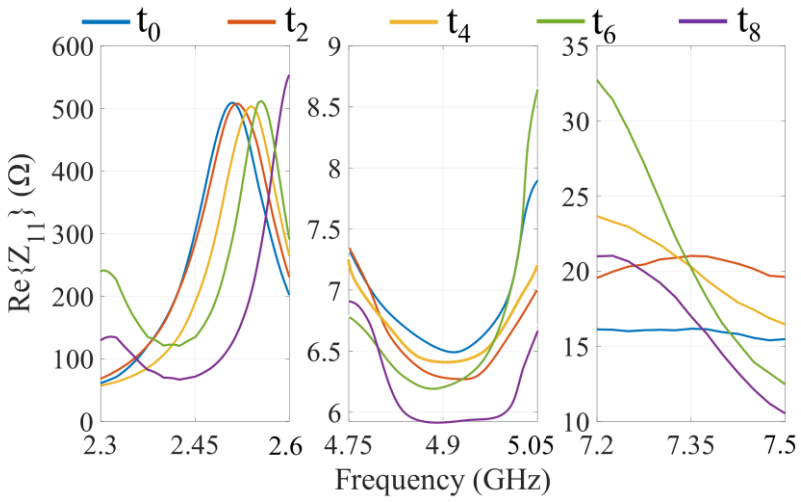

(a)

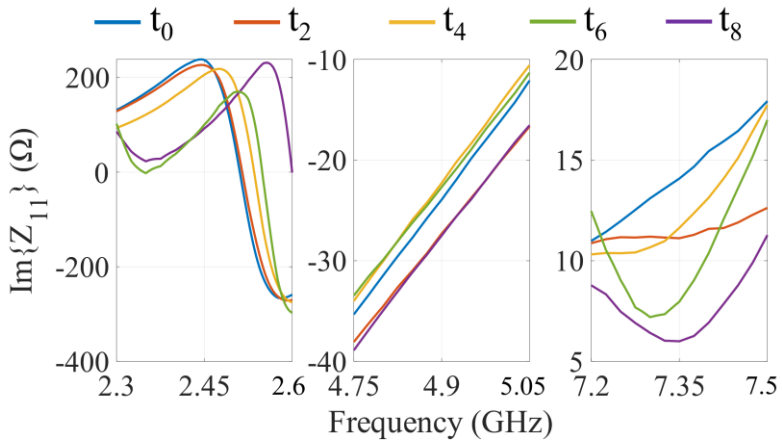

(b)

Fig. 5.8. (a) Real and (b) imaginary parts of the measured loaded-antenna input impedances over the bands centered around the first three harmonics of the oscillator. Measurements have been conducted for various time intervals during the drying process of the wood sample.

After a first design with a standard 50-Ω termination, the oscillator is analyzed using the antenna in free space as its (dispersive) load; 8 harmonics plus DC are considered in the HB simulation. The results of the bifurcation analysis for the system

are shown in Figure 5.9(a), where the two critical points, H1 and H2, correspond to Hopf bifurcations of the DC bias conditions [66-67]. Since the bifurcation at H1 is supercritical and at H2 is subcritical, all RF states along the branch H1-A-H2 are stable, including the nominal operating point A corresponding to gate-source voltage (V_{GS}) = -0.1 V, whereas the drain-source voltage (V_{DS}) is kept fixed at 2.5 V. On the other hand, all DC states between H1 and H2 are unstable due to the existence of a pair of complex conjugate natural frequencies with positive real parts that are solutions of the system characteristic equation. This instability ensures the growth of oscillations if the drain voltage is fixed at 2.5 V, while the gate voltage is swept from -3.1 V to 1.8 V. In the case under study, the estimated maximum output power-antenna input power reaches a value of about 16.4 dBm for a gate bias voltage of -0.1 V. Other bifurcation diagrams for different drain bias conditions are omitted here for brevity. Figure 5.9(b) shows the predicted tuning range of the self-oscillating antenna for the unloaded case, exhibiting monotonic behavior for any negative V_{GS}. This is driven by the strong nonlinear relation between the gate-source capacitance C_{GS} and V_{GS}. Oscillation is still feasible at weak positive values of V_{GS}, but the trend changes since it is now supported by nonlinear reactive effects beyond C_{GS}.

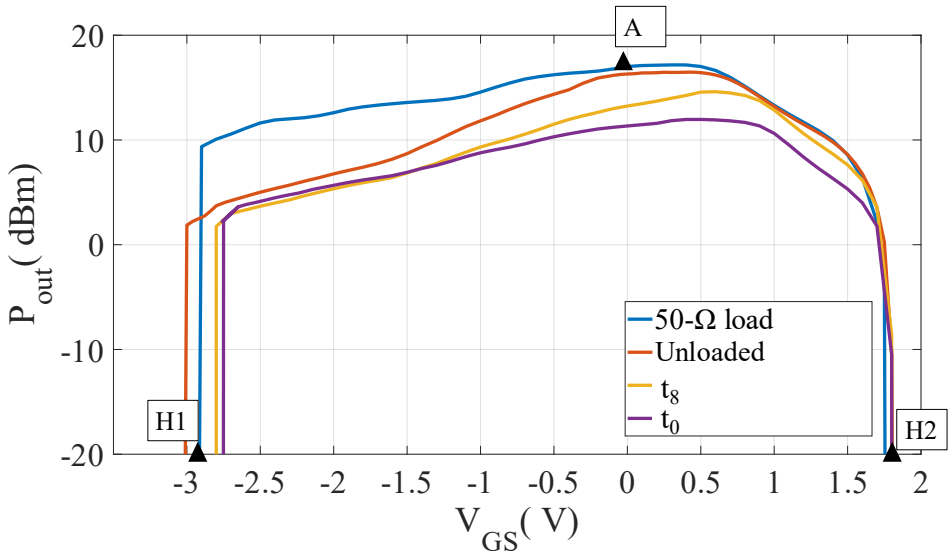

(a)

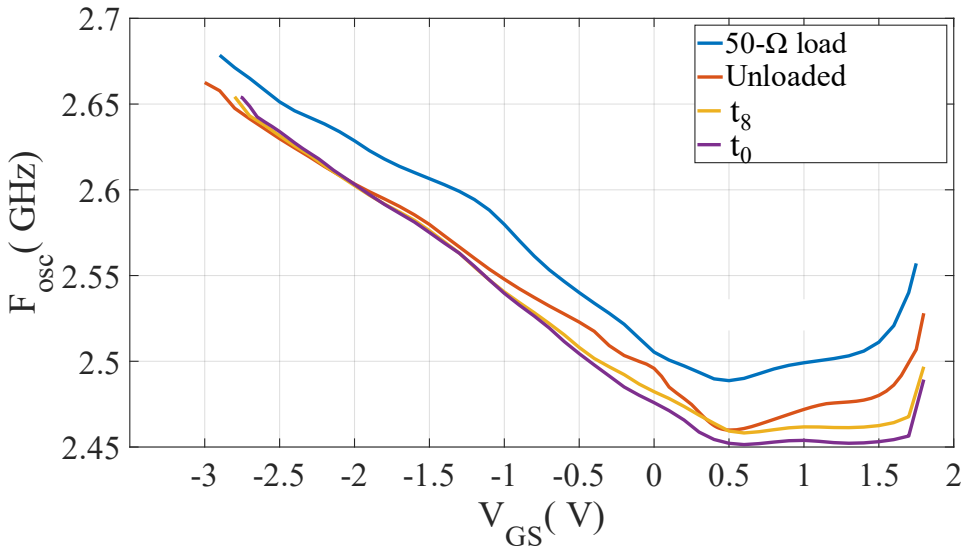

(b)

Fig. 5.9. (a) Predicted bifurcation diagrams, and (b) oscillating frequency in the steady-state regimes, for a 50-Ω load and three different loading conditions: unloaded, t_8, and t_0. Simulations are based on the t_0 and t_4 measurements of Fig.5.9.

The measured antenna data are used to realistically represent the oscillator load (dispersive behavior at all the harmonics of interest, far from an ideal 50-Ω load) within the nonlinear design procedure. The oscillatory behavior was calculated in various real-world conditions where moisture levels range from t_0 to t_8. For brevity's sake, only the extreme cases (t_0 and t_8) are shown in Figure 5.8, which presents the HB-simulated bifurcation diagrams and the steady-state oscillating frequencies. These results are compared with the unloaded antenna and the ideal 50-Ω load cases. In the simulations, V_{DS} is set to 2.5 V while V_{GS} is adjusted. For V_{GS} = -0.1 V, the RF power levels through the antenna are 16.3 dBm, 13.2 dBm, and 11.3 dBm for the unloaded, t_8, and t_0 scenarios, respectively. When using an ideal 50-Ω load, the power is noticeably overestimated, especially at lower V_{GS} values. As moisture increases, the antenna's dispersive behavior and the losses caused by higher humidity reduce the RF power of the self-oscillating antenna.

As expected, the oscillation frequency (F_{osc}) is strongly influenced by the

antenna's input impedance, which depends on the moisture levels. For example, with V_{DS} at 2.5 V and V_{GS} at -0.1 V, the predicted F_{osc} is 2.498 GHz, 2.48 GHz, and 2.47 GHz for the unloaded, t_8, and t_0 cases, respectively, while for a 50-Ω load, F_{osc} is 2.52 GHz. This shows that taking dispersive loads into account over the relevant harmonics allows for identifying distinct oscillatory behaviors, enabling the system to function as a moisture sensor. Additionally, under a given bias condition, the DC operating point varies depending on the dispersive loads. For instance, Figure 5.10 illustrates the predicted DC drain current, I_{DS0}, for varying V_{GS} at V_{DS} = 2.5 V, with the antenna loaded from t_0 to t_8 moisture levels, while the unloaded and 50-Ω load cases are shown for comparison. The nonlinear simulations across a wide V_{GS} range reveal that varying levels of I_{DS0}, and consequently different amounts of DC power, are required depending on the moisture content. In particular, for the case of V_{DS}=2.5V and V_{GS}=-3V, the predicted current is 16 mA and 21 mA for t_0 and t_8, respectively. The gap between the two moisture content cases increases as the V_{GS} increases. In particular, for the highest values of simulated V_{GS} (-0.1 V), the predicted I_{DS0} is 71 mA and 100 mA for t_0 and t_8, respectively.

The NL/EM simulations confirm the key idea of the proposed stand-alone solution and suggest that by keeping track of the DC states of the self-oscillating antenna, valuable insights can be gained about the antenna's loading conditions, and consequently the actual moisture content level of the tree sample under test.

5.4 Conclusion of the Chapter

In this chapter, two microwave-based solutions for hydration monitoring are proposed. In particular, a CSRR for skin hydration monitoring is presented, assisted by machine learning algorithms for the real-time identification of the hydration levels. The device presents a miniaturized structure and uses a low-cost and custom acquisition circuit, which controls the VNA for the measurements and performs the machine learning predictions.

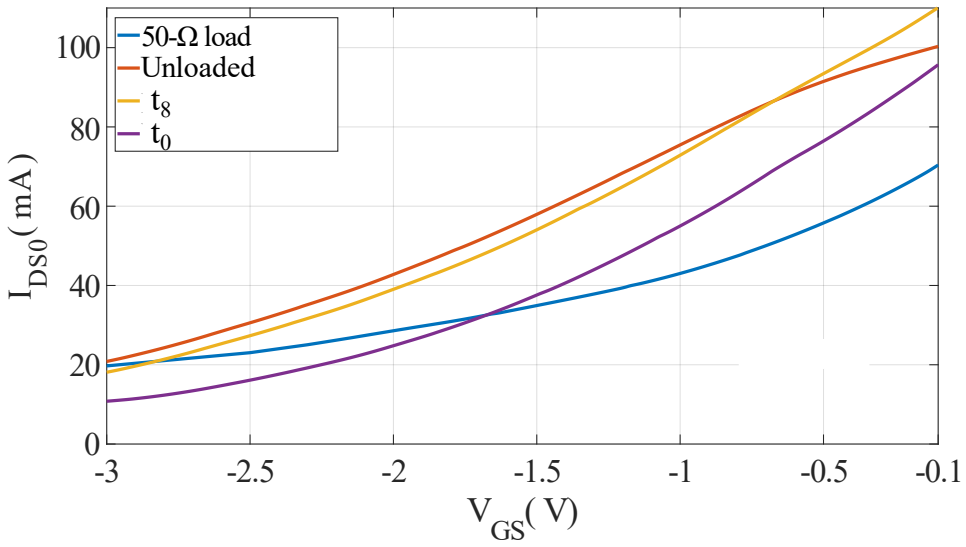

Fig. 5.10. Predicted dc drain current, I_{DS0} at V_{DS} = 2.5 V, with varying V_{GS} and for different loading conditions.

With respect to literature, the proposed sensor is miniaturized, lightweight, and offers real-time predictions, allowing the sensor to be exploited in portable medical applications.

In the second section of the chapter, a stand-alone moisture content sensor based on a self-oscillating antenna is proposed. The wood-loaded antenna is first measured, in different moisture content conditions. Then the self-oscillating antenna is designed by means of NL/EM co-simulations, and the key idea of exploiting only the DC information is validated. With respect to the state-of-the-art, the novel approach of monitoring only the DC states of the active device allows the removal of costly, bulky RF instrumentations that are commonly adopted in oscillator-based sensors. In particular, the solution is capable of retrieving the actual moisture content in the tree, in a compact design, which can be easily adopted for in-vivo measurements.

Chapter 6

Antenna System for Train Integrity and Positioning

This chapter is based on the following publications:

G. Paolini, E. Fazzini, S. Trovarello, D. Amato, D. Masotti and A. Costanzo, "A 2.4 GHz Modular Antenna System for Train Integrity and Localization Purposes," 2023 IEEE 13th International Conference on RFID Technology and Applications (RFID-TA), Aveiro, Portugal, 2023, pp. 221-224, doi: 10.1109/RFID-TA58140.2023.10290279

G. Paolini, E. Fazzini, S. Trovarello, D. Amato, D. Masotti and A. Costanzo, "An Innovative Multi-Port LoRa-Based Wireless Node for Railway Signaling and Positioning," in IEEE Journal of Radio Frequency Identification, vol. 8, pp. 618-626, 2024

6.1 Introduction of the Chapter

This chapter is dedicated to the presentation of the external activity carried out with industry partner in the railway industry, carried out together by the research group guided by Prof. Alessandra Costanzo. In particular, it describes the design and verification of a compact wireless node setup with a wireless system comprising a modular setup and three antennas operating in the 2.4 GHz band for positioning applications on secondary railway lines where the ERTMS is not available. Figure 6.1 shows the common scenario for high-speed networks that adhere to the ERTMS, where both Global System Mobile Communications in Railways (GSM-R) and Radio Block Center (RBC) are adopted.

An omnidirectional antenna, cross-polarized to the other two, permits the transfer of positioning data between the train and intelligent poles placed along the railway. Furthermore, it also contains two back-to-back directional antennas, enabling wagon-to-wagon communication to ensure the integrity of trains. LoRa systems outline data communication with low-power, long-range capability with acceptable latency for this application. In order to be insensitive as much as possible to possibly adverse environmental conditions, such as dust or ice, the system is designed to be as electromagnetically transparent as possible. Laboratory tests and field tests on a moving train, inside and outside the wagon, showed communications between wagons and with the poles along the railway.

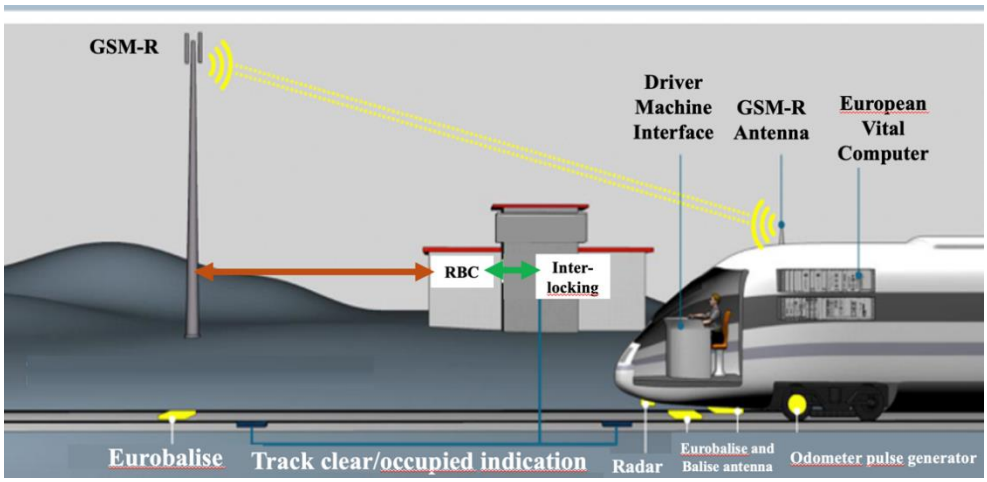

Fig. 6.1. Common scenario for high-speed networks in railway signaling and positioning adheres to the ERTMS ETCS [69] © 2024 IEEE.

6.2 Design of the Three-Antenna System

The primary objective of the project is to propose a network architecture that can correctly track the trains running on secondary lines, able to ensure their integrity. The proposed scenario foresees, for each car of every train, low-power low-cost sensor nodes spread along the intelligent poles on single-track railway lines at every 250

meters. In this scenario, the train convoy may have between one and four wagons. Since the railway has a length of approximately 30 km, an intelligent pole may be inserted every 250 meters, for a total of 120 poles for localization, each having the same type of node as that on the wagons. The main motivation is to allow the operation of two or more trains at the same time on the same secondary railway. Such would suppress the bottleneck situation whereby only one can operate at any given time, due to lack of adequate information on the exact location of these. LoRa protocol at 2.4 GHz is chosen for its power consumption, and it is pretty resilient due to the high sensitivity that allows detectable input signal levels to be as low as -129 dBm. It enables, on one hand, communication between wagons for train integrity (Network 1), and on the other hand between the train and intelligent poles along the railway (Network 2A), and among distinct kinds of intelligent poles for localization (Network 2B). A scheme of the network adopted in the study is reported in Figure 6.2.

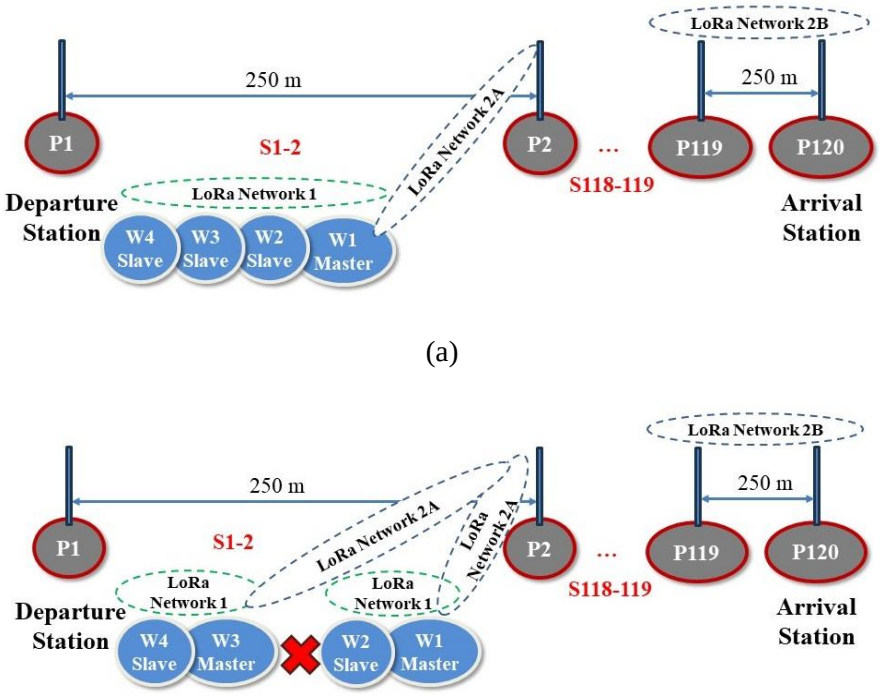

Fig. 6.2. (a) Scheme of the architecture of Network 1, 2A, and 2B in normal conditions, and (b) in case of train integrity loss between W2 and W3, with consequent generation of a new Network 2A with two Masters [69] © 2024 IEEE.

To ensure train integrity, Network 1 allows for communications among wagons that belong to the same train. The first wagon will be equipped with a LoRa node acting as the "Master"; the rest of the wagons will be assigned as "Slaves." The ISM band at 2.4 GHz is selected for operating the LoRa protocol. Operation in such a band will allow a further decrease in the overall dimensions of the prototype and especially of its radiating components.

For radiating elements of Network 1, on each wagon, two horizontally polarized directional patch antennas-named WWDAs -Wagon-Wagon Directive Antennas- are connected to ports P2 and P3. One antenna serves for communication with the previous wagon, the other antenna serves to connect to the next wagon. The antennas can be installed inside or outside the train. Network 2A provides the communication between a Master device, placed inside the first wagon W1, and all type-A Intelligent poles equipped with LoRa nodes to track the position of the train. Since the direction of the train is unknown in advance, an omnidirectional antenna must be installed on both devices, which for instance is connected to port P1, in order to assure sufficient communications performance such as a BER less than 10^{-3}. For the purpose of this experiment, a monopole antenna vertically polarized and cross-polarized relative to WWDAs is going to be used. This antenna, named WPOA -Wagon-Pole Omnidirectional Antenna- has an omnidirectional radiation pattern in the XY plane according to the layout shown in Figure 6.3 and will share the same LoRa frequency band of the antennas of Network 1. In case of separation between the wagons, the leading one of the separated parts will become the Master, and it will communicate with the intelligent poles. For example, as shown in Figure 6.2, if W2 and W3 get separated, then W3 and W4 would fall out of the main Master in W1. W3 would now behave like a Master for the second convoy, and it would communicate with the type-A poles of intelligent poles. The layout of the proposed three-antenna system, together with the adopted multilayer stack-up, is reported in Figure 6.3.

Copper	(L1)	Thickness: 0.035 mm
Rogers RO4350B	(Inner Layer #1)	Thickness: 1.52 mm
Copper	(L2)	Thickness: 0.035 mm
FR4	(Prepreg)	Thickness: 0.035 mm
Copper	(L3)	Thickness: 0.035 mm
Rogers RO4350B	(Inner Layer #2)	Thickness: 1.52 mm
Copper	(L4)	Thickness: 0.035 mm

(a)

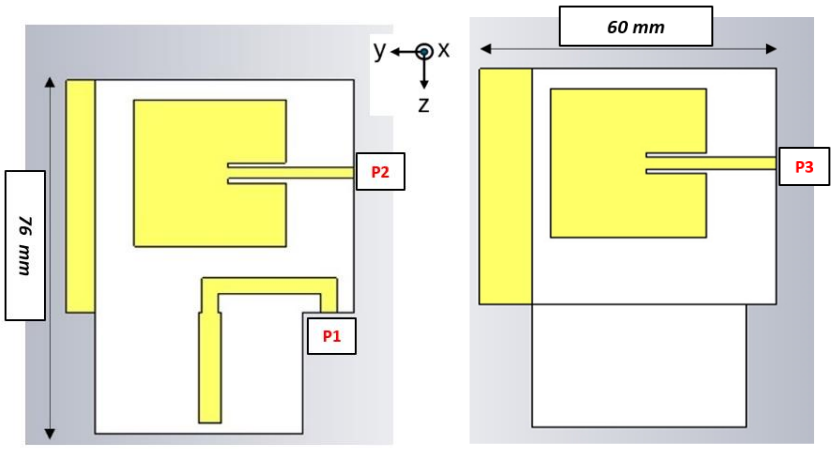

(b) (c)

Fig. 6.3. (a) Stack-up of the proposed multilayer solution, the layout of the (b) front and (c) back layers [69] © 2024 IEEE.

6.3 Experimental Validation of the System

S-parameters characterization and radiation pattern measurements were carried out in free space to validate the design, and the simulations were performed using the EM simulation software CST Studio Suite. In particular, a back-to-back configuration of the two patch antennas (P2 and P3) was selected to maximize decoupling between the two horizontally polarized antennas operating at the same frequency. The maximum measured value of the S_{23} transmission coefficient was -20 dB at 2.46 GHz, as shown in Figure 6.4.

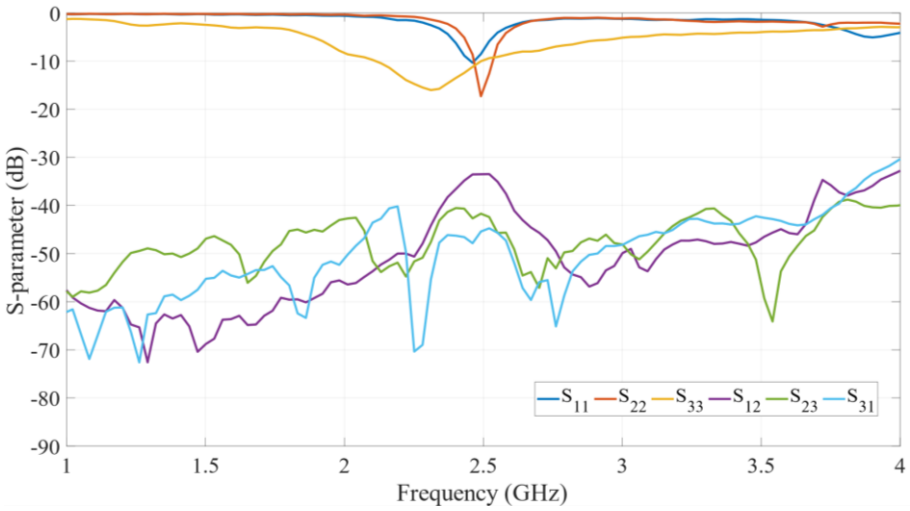

Fig. 6.4. Measured S-parameters of the three-antenna system in free space scenario [69] © 2024 IEEE.

Given this application, the most interfering factor with the ideal performance of the radiating elements would be metallic plates simulating the train wagons. Since the monopole antenna is ungrounded, it would be expected to be most affected by this interference. In this respect, as a complementing approach, the patch antennas are expected to be less affected by the wagon walls due to the presence of the metallic ground plane serving as a shield and hence provide a more robust solution. For a qualitative and quantitative estimation of the effect introduced above, simulations of the tri-port antenna module have been performed considering the presence of metallic layers simulating the wagon walls. A PEC plate was used in two configurations: (a) the module placed on top of the wagon and the plate placed underneath, and (b) the module mounted on the side wall of the wagon, with the plate placed beside it. Figure 6.5 shows the simulation setup of the two case studies.

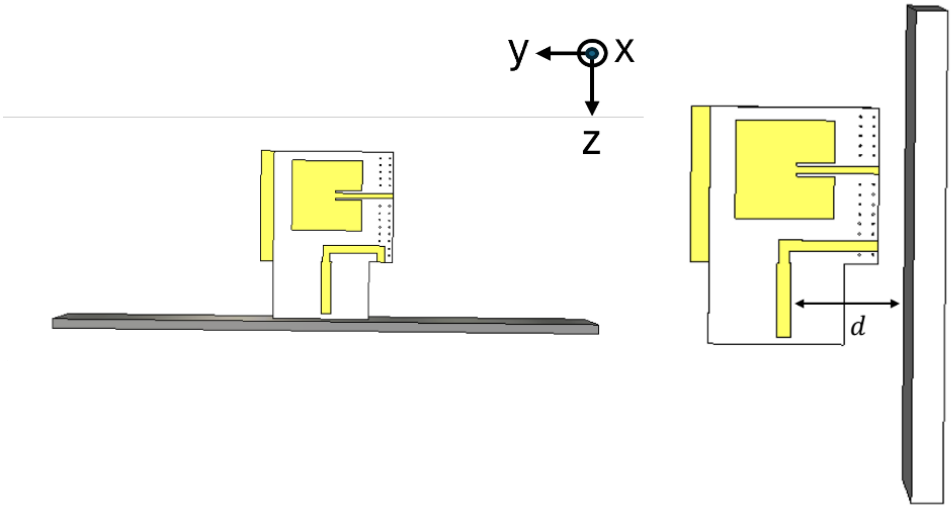

Fig. 6.5. (a) Simulation setup of the module on the top of the wagon, and (b) next to the wagon [69] © 2024 IEEE.

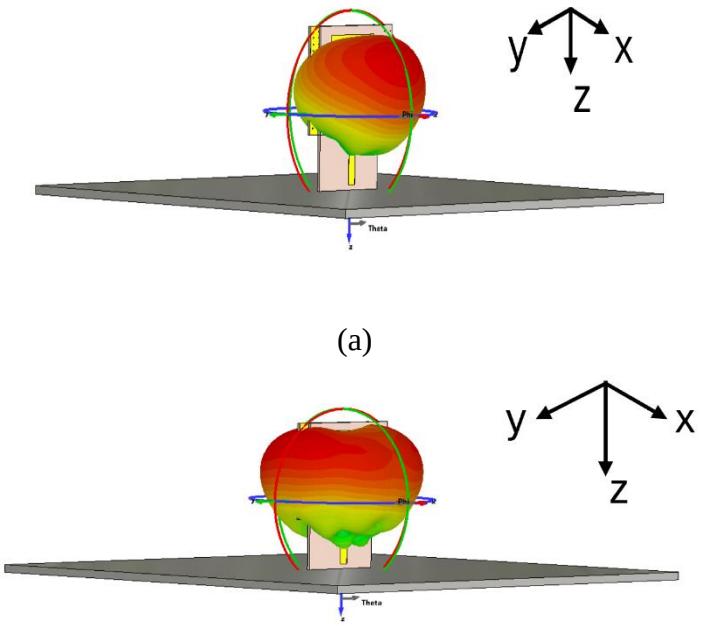

(a)

(b)

Fig. 6.6. Gain pattern of the (a) WWDA, and (b) for the case in which the plate is placed below the antenna system [69] © 2024 IEEE.

The simulation results for the setup presented in Figure 6.5 show that for patch antennas (WWDAs) in Network 1, the presence of the PEC plane causes a 30° deflection in the elevation of the radiation surface's peak, as shown in Figure 6.6 (a),

away from the metal plate. The radiation exhibits a maximum gain of 8 dBi with a half-power beam width (HPBW) of 50°, making it an efficient solution for train integrity. In the broadside direction, where the line-of-sight (LoS) link is established, the gain is approximately 5.3 dBi, which is higher than the ideal case described in [70].

Figure 6.7(a) and (b) show the results of the EM simulation for the case scenario reported in Figure 6.5(b).

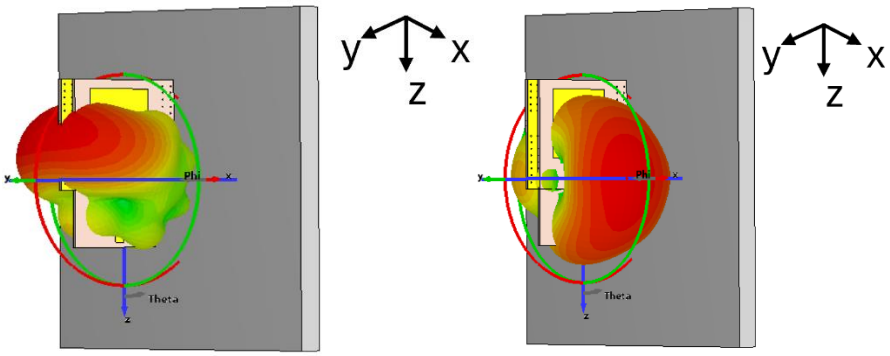

(a) (b)

Fig. 6.7. Gain pattern of the (a) WWDA, and (b) for the case in which the plate is placed on the side of the antenna system [69] © 2024 IEEE.

Studies on the layout of the WPOA with the variations of distance *d* separating the module from the lateral wall of the wagon have been undertaken. This is especially critical for the monopole antenna because a PEC plate perpendicular to the vertical axis of the WPOA can cause considerable obstruction unless appropriately placed. As is known from the EM theory, it has been verified that the best setup and performance occurs when this distance is fixed to a quarter of wavelength (d = λ/4) such that the wall behaves as a perfect reflector halving the radiation pattern of the WPOA in the useful half-plane where the link is meant to be established. The radiation surface, presented in Fig. 6.7(a), presents a deflection in the elevation plane of approximately 30° (particularly useful considering the nature of Network 2), with a maximum gain of

8.8 dBi and an HPBW of 44◦. Modeling of the patch antennas from Network 1 coupled with simulation results indicates that the PEC plane is irrelevant to the 3D radiation pattern of the network. In particular, they present a standard radiation orthogonal to the patch plane with a maximum gain of 6.3 dBi and HPBW of 97°, as shown in Figure 6.7(b). In particular, observing the simulated results, in the case of the WWDAs, which are responsible for train integrity and using two directional patch antennas facing each other, the best option remains with lateral positioning of the boot module onto the wagon wall. This allows a high positive radiation pattern broadside but in a favorable direction. As for WPOA, which interfaces with an intelligent pole on top of the wagon, the middle and top poses are both efficient and robust. However, the first solution is adopted for ease of measurement.

Outdoor placement of the antennas exposes them to atmospheric agents like rain, dust, and ice, which can degrade antenna performance by affecting their matching with the LoRa device and altering the radiation patterns of the modular tri-antenna. To prevent this, a protective plastic case made from polylactic acid (PLA), commonly used in 3D printing, was designed using an Ultimaker 3 Extended printer. The case's electromagnetic properties were characterized using the T-resonator technique, with a dielectric constant of 2.64 and tanδ of 0.018 at 2.4 GHz [71]. A thickness of 3 mm was chosen to balance mechanical strength with minimal impact on antenna performance.

The case, measuring 68 x 90 x 39 mm^3, protects the antenna system without affecting performance and features interlocking joints for easy access and holes for RF cable connections. Antenna measurements, taken with the Agilent N9923A FieldFox VNA, showed minor differences between the simulated and measured reflection coefficients. The patch antenna presents a reflection coefficient peak of -14 dB at 2.45 GHz, while the monopole antenna showed a 140 MHz shift but maintained a return loss greater than 10 dB within the target band. Gain degradation was minimal, with 0.2 dB for the WPOA and 0.4 dB for the WWDA. Radiation patterns were measured in free space and matched well with simulations, showing a maximum gain of 4.2 dBi for the WPOA at 25° and 5.4 dBi for the WWDA in the broadside direction. To validate

the design, the case was also analyzed under different atmospheric conditions, including dust accumulation and ice buildup. Both the dust and ice electrical properties are extracted from the literature [72-73].

Simulation results are presented in case of dust or ice build-ups. The maximum amounts of dust and ice were 2 mm and 5 mm respectively, which are realistic cases where the antenna module is mounted on the outside part of the train wagon exterior. Results of the simulations demonstrate quite clearly that any deterioration of the radiating performance of the antenna module due to dust or ice buildup is under control. For the omnidirectional antenna case, in the worst scenario (5 mm of ice) the return loss peak shifts from a frequency of 2.42 GHz to 2.37 GHz, and at the same time good matching conditions are offered with the reflection coefficient of around -15 dB at a frequency of 2.45 GHz. In general, patch antennas are less affected by atmospheric agents, where the peak of the reflection coefficient remains at 2.45 GHz, while the magnitude shifts from -28 dB for the no-agents scenario to -15 dB for the most critical scenario. The predicted reflection coefficients of both WWDA and WPOA antennas affected by atmospheric agents are shown in Figure 6.8.

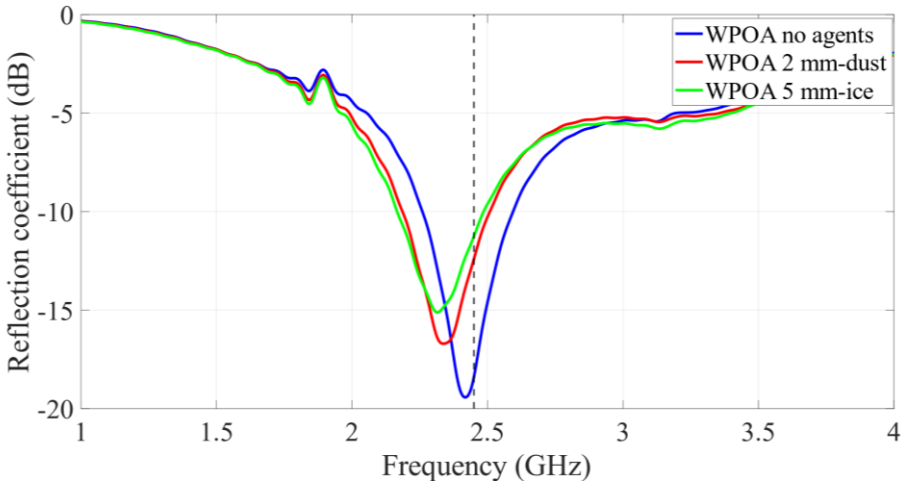

(a)

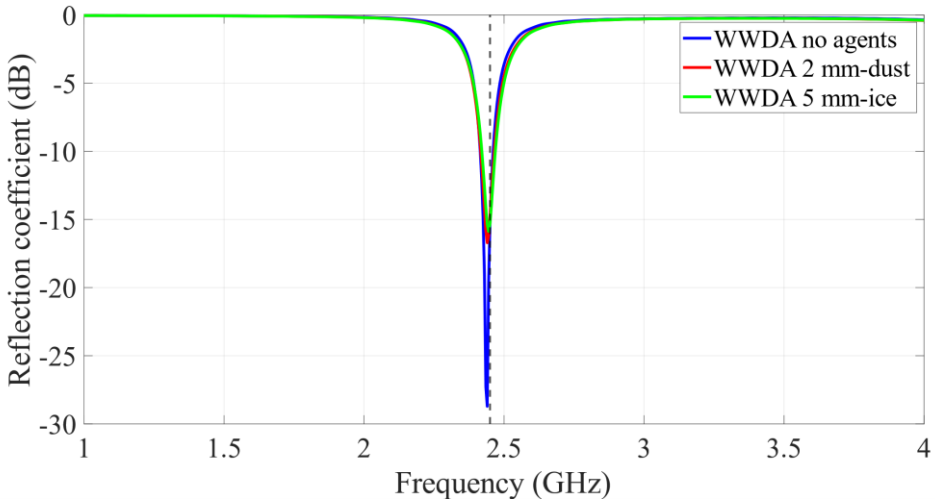

(b)

Fig. 6.8. Simulated $|S_{ii}|$ of the (a) monopole antenna, and (b) patch antennas, whether there are dust or ice agents deposited on the surface of the case [69] © 2024 IEEE.

Similar analysis can also be undertaken for tri-ports transmission coefficients, but for the sake of brevity are not shown. However, there is a slight change in gain performance when ice or snow thickness varies. The most significant reduction of 0.52 dB in the gain occurs with patch antennas with a deposited 5 mm layer of ice.

An experimental measurement campaign was carried out for Network 1 (wagon-to-wagon communication) and Network 2 (type-A intelligent pole-train) communication by using the tri-port module after the design and simulation stages. Both networks were set up with antennas acting as transmitter and receiver, respectively, connected to LoRa modules operating at a frequency of 2.45 GHz, one of which was used as a Gateway. In this way, the performance of the RSSI values concerning distance and environmental conditions could be tested. The measurements were carried out on the Modena-Sassuolo railway line, precisely on the subsection between Modena and Formigine.

Fig. 6.9. Photo of the designed three-antenna system mounted outside the train cockpit [69] © 2024 IEEE.

The tests had been performed on an electric train owned by Alstom Ferroviaria, composed of three wagons for a total length of about 75 meters. During the first run from Modena to Formigine, two prototypes were arranged outside the front and rear cockpit windows shown in Figure 6.9, to verify the train integrity over the run. The devices were constantly powered by a DC supply on board the train. The measurements proved the feasibility of the link; over the about 29-minute test, 276 packets were detected with an average RSSI of -69.1 dBm, and 3 packets lost. The return trip from Formigine to Modena was devoted to the analysis of the communication between wagons, taking into consideration the presence of passengers.

Three application scenarios were tested and proved all effective in providing train integrity:

(a) Three-wagon distance: Duration of 260 seconds, Packets detected: 49, Packets lost: 2, Average RSSI: -84.8 dBm.

(b) Two-wagon distance: Duration of 198 seconds, Packets detected: 50, Packets lost: 0, Average RSSI: -77.2 dBm.

(c) One-wagon distance: Duration of 197 seconds, Packets detected: 51, Packets lost: 0, Average RSSI: -58.3 dBm.

For Network 2 communication, the 2.45 GHz antenna module of Gateway is set outside the front cockpit window for the second Formigine to Modena journey. Regarding testing the communication with a type A Intelligent pole, the end device is equipped with the Network 2 monopole antenna fixed on a pole 2 meters high in Baggiovara station.

Table 6.1
Average RSSI, SNR, PER, and BER for Network 1 [67] © 2024 IEEE

Communication Link	Antennas Position	Average RSSI (dBm)	SNR (dB)	PER	BER
Network 1 (3 wagons)	Outside Train	–69.1	50.9	0.0109	$5.69 \cdot 10^{-5}$
Network 1 (3 wagons)	Inside Train	–84.8	35.2	0.0392	$2.08 \cdot 10^{-4}$
Network 1 (2 wagons)	Inside Train	–77.2	42.8	0	0
Network 1 (1 wagon)	Inside Train	–58.3	61.7	0	0

According to the test results, the packets of the Gateway can be tracked for a length of up to 350 meters of the distance between the driver and the station pole, with the minimum received RSSI of -86 dBm. The average RSSI is -58.9 dBm while the vehicle driving away from the station, whereas it is -56.7 dBm approaching the station. Table 6.1 summarizes the performed measurement together with other performance characterizations such as the packet error rate (PER) and bit error rate (BER). In particular, the BER is calculated as:

$$BER = 1 - \left(1 - PER^{1/n}\right) \tag{6.1}$$

where n is the number of bits per packet (192 bits), each packet containing a 4-byte payload and overhead (12 bytes for addressing, preamble, and LoRa synchronization). With these parameters, the time on air is 690.64 ms if the spreading factor is 12, the frequency band has a bandwidth of 200 kHz, and the coding rate is 4/5. The SNR values

are also presented in Table VI, where the user is assumed to use an SNR noise floor of the Semtech SX1280 device equal to -120 dBm. The journey measurements are characterized by flat terrain, a maximum speed of 59 km/h, and an average speed of 21.8 km/h. Three different environments have been considered during the trip, i.e., urban area, extra-urban area, and tunnel; in that sense, Figure 6.10 represents the RSSI retrieved concerning the different environments that have been crossed by the train during the first run (antennas positioned outside the train with 3-wagon distance). Measurements show that the system can guarantee the train integrity, where communication between wagons can be achieved even with the antennas placed inside or outside the train. Moreover, the LoRa Radio frequency bands (at 2.4 GHz) for Network 2 are equivalent for proper links to the displaced inductive signaling units and the cheap distance determination between any two trains on the sidetrack system. In particular, the possibility of simultaneous tracking of many trains on the same rail line has emerged as another potential application.

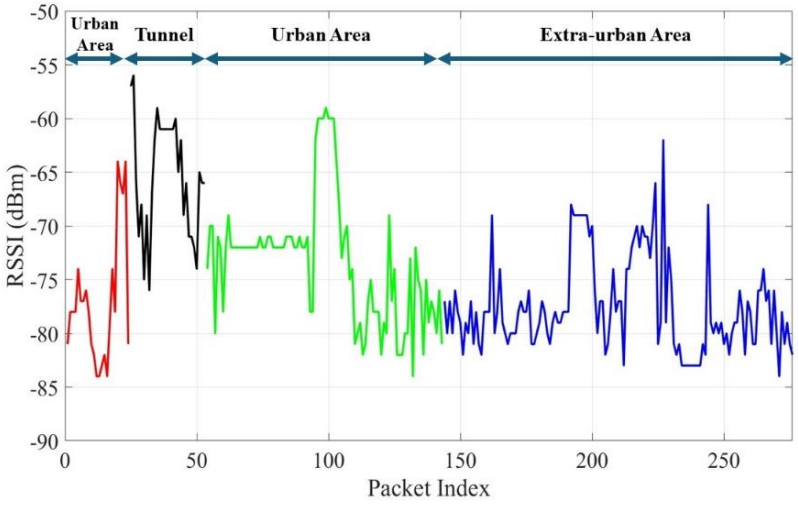

Fig. 6.10. Measured RSSI in different scenarios that have been encountered by the train, with the two modules placed outside it at a distance of about 75 m [69] © 2024 IEEE.

6.4 Conclusion of the Chapter

In this chapter, the design and validation of a compact wireless system, which uses a modular setup consisting of three co-located antennas operating in the 2.4 GHz band, is discussed. This system is specifically designed for positioning purposes on secondary railway lines where the ERTMS is unavailable. The system uses LoRa technology to enable low-power communication with sufficient latency performance for this application. Given potential environmental challenges, such as dust or ice, the system is housed in an enclosure designed to be as electromagnetically transparent as possible. The system is tested both in the lab and in real-world conditions on a moving train, both inside and outside the wagons. The tests confirmed successful communication between wagons and the trackside poles. The highest observed bit error rate during testing was 2.08×10^{-4} in the most challenging conditions.

Conclusion

In this thesis, the design, fabrication, and testing of several microwave and mmWaves circuits are presented. Firstly, the topic of reconfigurable devices is covered by proposing novel nonlinear models for ferroelectric-based phase shifters. The models are derived from experimental measurements and validated by HB simulations, demonstrating a low error between the measured and simulated device. Moreover, an in-depth study on the effects of nonlinearities of the ferroelectric material on the device performance is presented, focusing on the power-handling capabilities of the devices.

Then, a study on rectifier topologies and fabrication technologies for a wide dynamic range and silicon-integrated solutions is provided. Firstly, the 45-dB dynamic range and modular rectifier is discussed. The concurrent use of floating-gate HEMTs and the power-selective optimization of the rectifying branches allows to extend the common limitation of state-of-the-art rectifiers, which can work efficiently only in certain power operating regions. Moreover, the feasibility of the realization of integrated rectennas on silicon is discussed by highlighting the common issues of on-chip antennas and a possible solution to overcome their poor radiation performance. In particular, a multilayer technology and fabrication process is presented which demonstrated to increase the radiation efficiency of planar on-chip antennas. Given the need for power-autonomous solutions for the next generation of IoT devices, the multilayer technology is also validated by designing two different rectennas. The latter solutions, operating at microwaves and mmWaves, can be exploited to harvest RF waste energy in the ambiance, to power low-energy sensors and devices.

Given the interest in stand-alone solutions, two microwave-based solutions for biological monitoring are presented. Firstly, a non-invasive skin hydration sensor, based on a near-field resonator and custom acquisition circuit is presented. The sensor, assisted by a machine learning algorithm stored in the acquisition circuit, can provide a real-time classification of the skin hydration level. Moreover, a moisture content

sensor adopting a self-oscillating antenna is proposed. The main goal of the activity is to overcome the limitation of common oscillator-based devices, which usually retrieve the information of the material under test, by adopting external equipment, making the sensor bulky and costly. The proposed concept, which is based on the monitoring of the DC states of the self-oscillating antennas, as the moisture content condition of the wood sample changes, allows the sensor to be stand-alone, compact, lightweight, and cheap to manufacture.

In Chapter VI, the design and characterization of an innovative and low-cost architecture designed for poorly equipped secondary railway lines is presented. The activity, carried out with the industry, is dedicated to train signaling and positioning purposes, and is based on the LoRa protocol at 2.4 GHz. A modular system comprising three different antennas is conceived and realized. This allows each wagon to communicate with the previous and following one(s), as well as to establish a connection between the train and the intelligent poles up to a distance of 350 m. Also, several weather conditions have been considered, and for this purpose, an ad-hoc case in plastic 3D printable material is conceived and realized to protect the antenna module against harsh environmental conditions. Measurements on the field are proposed, including the observation of parameters such as BER, in different scenarios across the train journey, always demonstrating a stable and reliable connection between the wagon-wagon and wagon-intelligent poles networks.

References

[1] Y. Jia, G. Jiang, Y. Liu and Y. Zhong, "Beam Scanning for Dual Polarized Antenna With Active Reflection Metasurface," in IEEE Antennas and Wireless Propagation Letters, vol. 21, no. 9, pp. 1722- 1726, Sept. 2022.

[2] M. Sazegar et al., "Beam Steering Transmitarray Using Tunable Frequency Selective Surface With Integrated Ferroelectric Varactors," in IEEE Transactions on Antennas and Propagation, vol. 60, no. 12, pp. 5690-5699, Dec. 2012.

[3] M. Nikfalazar et al., "Beam Steering Phased Array Antenna With Fully Printed Phase Shifters Based on Low-Temperature Sintered BST Composite Thick Films," in IEEE Microwave and Wireless Components Letters, vol. 26, no. 1, pp. 70-72, Jan. 2016.

[4] M. Aldrigo et al., "Low-Voltage Permittivity Control of Coplanar Lines Based on Hafnium Oxide Ferroelectrics Grown on Silicon," in IEEE Access, vol. 7, pp. 136686- 136693, 2019.

[5] M. Dragoman, M. Modreanu, I.M. Povey, S. Iordanescu, M. Aldrigo, C. Romanitan, D. Vasilache, A. Dinescu and D. Dragoman., "Very large phase shift of microwave signals in a 6 nm HfxZr1-xO2 ferroelectric at ±3 V". Nanotechnology, 2017.

[6] Zulfi, J. Suryana and A. Munir, "Characterization of Capacitor-Loaded Transmission Line for Phase Shifter Application," 2022 International Workshop on Antenna Technology (iWAT), Dublin, Ireland, 2022, pp. 17-20.

[7] Lei Zhu and K. Wu, "A general-purpose circuit model of interdigital capacitor for accurate design of low-loss microstrip circuit," 1998 IEEE MTT-S International Microwave Symposium Digest (Cat. No.98CH36192), Baltimore, MD, USA, 1998, pp. 1755-1758 vol.3.

[8] R. Correia, N. Borges Carvalho, and S. Kawasaki, “Continuously power delivering for passive backscatter wireless sensor networks,” IEEE Trans. Microw. Theory Techn., vol. 64, no. 11, pp. 3723–3731, Nov. 2016.

[9] S. Yoshida, G. Fukuda, T. Noji, S. Tashiro, Y. Kobayashi, and S. Kawasaki, "Wide power range operable 3-stage S-band microwave rectifier with automatic selector based on input power level," in *IEEE MTT-S Intern. Microw. Symp. Digest (MTT)*, 2013, pp. 1-4.

[10] X. Wang and A. Mortazawi, "Rectifier Array With Adaptive Power Distribution for Wide Dynamic Range RF-DC Conversion," in *IEEE Trans. Microw. Theory Techn*, vol. 67, no. 1, pp. 392-401, Jan. 2019.

[11] P. Wu, Y. Chen, W. Zhou, Z. H. Ren, and S. Y. Huang, "A Wide Dynamic Range Rectifier Array Based on Automatic Input Power Distribution Technique," in *IEEE Microw. Wireless Compon. Lett.*, vol. 30, no. 4, pp. 437-440, April 2020.

[12] S. Y. Zheng, S. H. Wang, K. W. Leung, W. S. Chan, and M. H. Xia, "A High-Efficiency Rectifier With Ultra-Wide Input Power Range Based on Cooperative Structure," in *IEEE Trans. Microw. Theory Techn*, vol. 67, no. 11, pp. 4524-4533, Nov. 2019.

[13] J. Yamazaki, R. Ishikawa, and K. Honjo, "Input-Power-Synchronous Adaptively Biased Wide-Dynamic-Range High-Efficiency Rectifier with Zero-Threshold GaAs HEMTs," in *50th European Microw. Conf. (EuMC)*, 2021, pp. 436-439.

[14] N. N. Mai-Khanh and K. Asada, "Integrated On-Silicon and On-glass Antennas for Mm-Wave Applications: (Invited)," 2020 7th NAFOSTED Conference on Information and Computer Science (NICS), 2020, pp. 384-387.

[15] W. A. Ahmad, M. Kucharski, A. Di Serio, H. J. Ng, C. Waldschmidt and D. Kissinger, "Planar Highly Efficient High-Gain 165 GHz OnChip Antennas for Integrated Radar Sensors," in IEEE Antennas and Wireless Propagation Letters, vol. 18, no. 11, pp. 2429-2433, Nov. 2019.

[16] Hyung Suk Lee, Jeong-Geun Kim, Songcheol Hong and Jun-Bo Yoon, "Micromachined CPW-fed suspended patch antenna for 77 GHz automotive radar applications," The European Conference on Wireless Technology, 2005.

[17] G. P. Gauthier, A. Courtay and G. M. Rebeiz, "Microstrip antennas on synthesized low dielectric constant substrates," in IEEE Transactions on Antennas and Propagation, vol. 45, no. 8, pp. 1310-1314, Aug. 1997.

[18] A. Pourafzal, T. Roi-Taravella, M. Cheffena and S. Y. Yayilgan, "A Low-Cost and Accurate Microwave Sensor System for Permittivity Characterization," in IEEE Sensors Journal, vol. 23, no. 2, pp. 1234- 1248, 15 Jan.15, 2023.

[19] F. Benassi, G. Paolini, D. Masotti and A. Costanzo, "A Wearable Flexible Energy-Autonomous Filtenna for Ethanol Detection at 2.45 GHz," in IEEE Transactions on Microwave Theory and Techniques, vol. 69, no. 9, pp. 4093-4106, Sept. 2021.

[20] A. M. Albishi and O. M. Ramahi, "Microwaves-Based High Sensitivity Sensors for Crack Detection in Metallic Materials," in IEEE Transactions on Microwave Theory and Techniques, vol. 65, no. 5, pp. 1864-1872, May 2017.

[21] R. Chandra, H. Zhou, I. Balasingham and R. M. Narayanan, "On the Opportunities and Challenges in Microwave Medical Sensing and Imaging," in IEEE Transactions on Biomedical Engineering, vol. 62, no. 7, pp. 1667-1682, July 2015.

[22] C. -H. Pai and C. -H. Tseng, "A New Microwave Oscillator-Based Microfluidic Sensor for Complex Permittivity Measurement," 2023 IEEE/MTT-S International Microwave Symposium - IMS 2023, San Diego, CA, USA, 2023, pp. 967-970.

[23] A. Ebrahimi, J. Scott and K. Ghorbani, "Ultrahigh-Sensitivity Microwave Sensor for Microfluidic Complex Permittivity Measurement," in IEEE Transactions on Microwave Theory and Techniques, vol. 67, no. 10, pp. 4269-4277, Oct. 2019.

[24] S. M. Kleiner, “Water: An essential but overlooked nutrient,” J. Amer. Dietetic Assoc., vol. 99, no. 2, pp. 200–206, Feb. 1999.

[25] B. Benelam and L. Wyness, “Hydration and health: A review,” Nutrition Bull., vol. 35, no. 1, pp. 3–25, Mar. 2010.

[26] D. R. Thomas et al., “Understanding clinical dehydration and its treatment,” J. Amer. Med. Directors Assoc., vol. 9, no. 5, pp. 292–301, Jun. 2008.

[27] L. Peng et al., "A Fused Learning and Enhancing Method for Accurate and Noninvasive Hydration Status Monitoring With UWB Microwave Based on Phantom," in IEEE Transactions on Microwave Theory and Techniques, vol. 71, no. 9, pp. 4027-4036, Sept. 2023.

[28] A. Cataldo et al., "Portable Microwave Reflectometry System for Skin Sensing," in IEEE Transactions on Instrumentation and Measurement, vol. 71, pp. 1-8, 2022.

[29] S. Bing, K. Chawang and J.-C. Chiao, "A Flexible Tuned Radio-Frequency Planar Resonant Loop for Noninvasive Hydration Sensing," in IEEE Journal of Microwaves, vol. 3, no. 1, pp. 181-192, Jan. 2023.

[30] Marina Vera Zambrano, Baishali Dutta, Donald G. Mercer, Heather L. MacLean, Marianne F. “Touchie, Assessment of moisture content measurement methods of dried food products in small-scale operations in developing countries: A review” Trends in Food Science & Technology, Volume 88, 2019, Pages 484-496.

[31] G. Paolini, M. Shanawani, D. Masotti, D. M. M. . -P. Schreurs and A. Costanzo, "Respiratory Activity Monitoring by a Wearable 5.8 GHz SILO With Energy Harvesting Capabilities," IEEE Journal of Electromagnetics, RF and Microwaves in Medicine and Biology, vol. 6, no. 2, pp. 246-252, June 2022.

[32] C. -H. Tseng and C. -Z. Wu, "A Novel Microwave Phased- and Perturbation-Injection-Locked Sensor With Self-Oscillating Complementary Split-Ring Resonator for Finger and Wrist Pulse Detection," IEEE Transactions on Microwave Theory and Techniques, vol. 68, no. 5, pp. 1933-1942, May 2020.

[33] T. Sokoll and A. F. Jacob, "Self-Oscillating Measurement System for In Situ-Monitoring Moisture in Buildings," IEEE Transactions on Instrumentation and Measurement, vol. 63, no. 12, pp. 2911-2918, Dec. 2014.

[34] C. -H. Pai and C. -H. Tseng, "A New Microwave Oscillator-Based Microfluidic Sensor for Complex Permittivity Measurement," 2023 IEEE/MTT-S International Microwave Symposium - IMS 2023, San Diego, CA, USA, 2023, pp. 967-970.

[35] Z. Cao, Z. Lu, P. Liu and J. Tan, "Nondestructive Microwave Self-Oscillating Sensor Based on Complementary Spiral Resonator for Defect Evaluation of Metallic Mesh," IEEE Transactions on Microwave Theory and Techniques, vol. 72, no. 3, pp. 1754-1765, March 2024.

[36] O. G. Crespillo et al., “Local GNSS threat detection methods for virtual balise placement in railway applications,” in Proc. 16th ITST, 2018, pp. 1–7.

[37] J. Mendizabal, J. Goya, G. De Miguel, L. Valdivia, S. Arrizabalaga, and I. Adin, “Virtual testing of the on-board ETCS with GNSS based Train integrity determination,” in Proc. 15th ITST, 2017, pp. 1–7.

[38] S. Oh, Y. Yoon, K. Kim, and Y. Kim, “Design of train integrity monitoring system for radio based train control system,” in Proc. 12th ICCAS, Jeju, South Korea, 2012, pp. 1237–1240.

[39] A. Schütz, D. E. Sánchez-Morales, and T. Pany, “Precise positioning through a loosely-coupled sensor fusion of GNSS-RTK, INS and LiDAR for autonomous driving,” in Proc. IEEE/ION PLANS, 2020, pp. 219–225.

[40] Y. Zhou, Q. Chen, and X. Niu, “Kinematic Measurement of the Railway Track Centerline Position by GNSS/INS/Odometer Integration,” IEEE Access, vol. 7, pp. 157241–157253, 2019.

[41] G Y. Li, S. Han, L. Yang, F.-Y. Wang, and H. Zhang, “LoRa on the move: Performance evaluation of LoRa in V2X communications,” in Proc. IEEE IV Symp., 2018, pp. 1107–1111.

[42] P. A. Torres, C. B. D. Silva, and H. T. Filho, “An experimental study on the use of LoRa technology in vehicle communication,” IEEE Access, vol. 9, pp. 26633–26640, 2021.

[43] J. Gozalvez, M. Sepulcre, and R. Bauza, “IEEE 802.11p vehicle to infrastructure communications in urban environments,” IEEE Commun. Mag., vol. 50, no. 5, pp. 176–183, May 2012.

[44] D. Bri, M. Fernandez-Diego, M. Garcia, F. Ramos, and J. Lloret, “How the weather impacts on the performance of an outdoor WLAN,” IEEE Commun. Lett., vol. 16, no. 8, pp. 1184–1187, Aug. 2012.

[45] S. Trovarello, A. Di Florio Di Renzo, M. Aldrigo, D. Masotti, M. Dragoman and A. Costanzo, "Nonlinear circuit model of IDCs on ferroelectric nanomaterial for reconfigurable applications," 2022 52nd European Microwave Conference (EuMC), Milan, Italy, 2022, pp. 175-178.

[46] V. Rizzoli and A. Costanzo, “An accurate bilateral FET model suitable for general nonlinear and power applications,” Int J. RF Microw. Comput.-Aided Eng., vol. 10, no. 1, pp. 43–62, Jan. 2000.

[47] S. Trovarello, A. D. F. D. Renzo, M. Aldrigo, D. Masotti, M. Dragoman and A. Costanzo, "Nonlinear Modelling of Steerable Antenna Array by Ferroelectric Capacitors Based on Nanoscale Layers of HfZrO," 2023 53rd European Microwave Conference (EuMC), Berlin, Germany, 2023, pp. 524-527.

[48] H. Ishida *et al.*, "A high-power RF switch IC using AlGaN/GaN HFETs with single-stage configuration," in *IEEE Trans. Electron. Devices*, vol. 52, no. 8, pp. 1893-1899, Aug. 2005.

[49] S. Trovarello, G. Paolini, D. Masotti and A. Costanzo, "A Modular System of Rectifiers for Energy Harvesting with Wide Dynamic Input-Range," in *6th International Conference on Smart and Sustainable Technologies (SpliTech)*, 2021, pp. 1-4.

[50] S. Trovarello, G. Paolini, D. Masotti and A. Costanzo, "Cascaded Rectifiers for Energy Harvesting With a Wide Dynamic Power Range," in IEEE Journal of Radio Frequency Identification, vol. 7, pp. 64-73, 2023.

[51] H. Aliakbari, A. Abdipour, A. Costanzo, D. Masotti, R. Mirzavand and P. Mousavi, "Far-Field-Based Nonlinear Optimization of Millimeter-Wave Active Antenna for 5G Services," in IEEE Transactions on Microwave Theory and Techniques, vol. 67, no. 7, pp. 2985-2997, July 2019.

[52] https://www.topsil.com/en/silicon-wafer-products/fz-hires/

[53] S. Trovarello, D. Masotti, M. Aldrigo, M. Modreanu and A. Costanzo, "Design of a 24-GHz dual-polarized rectenna integrated on silicon," 2021 51st European Microwave Conference (EuMC), London, United Kingdom, 2022, pp. 684-687.

[54] S. Trovarello, M. Aldrigo, D. Masotti, M. Dragoman and A. Costanzo, "Design of an Integrated Rectenna on Multi-layer High-Resistivity Silicon Substrate," 2023 XXXVth General Assembly and Scientific Symposium of the International Union of Radio Science (URSI GASS), Sapporo, Japan, 2023, pp. 1-4.

[55] S. Trovarello, D. Masotti, M. Aldrigo, M. Modreanu and A. Costanzo, "Design of a 24-GHz dual-polarized rectenna integrated on silicon," 2021 51st European Microwave Conference (EuMC), London, United Kingdom, 2022, pp. 684-687.

[56] . Kilpijärvi, J. Tolvanen, J. Juuti, N. Halonen and J. Hannu, "A Non-Invasive Method for Hydration Status Measurement With a Microwave Sensor Using Skin Phantoms," in IEEE Sensors Journal, vol. 20, no. 2, pp. 1095-1104, 15 Jan.15, 2020.

[57] Hasgall PA, Di Gennaro F, Baumgartner C, Neufeld E, Lloyd B, Gosselin MC, Payne D, Klingenböck A, Kuster N, “IT’IS Database for thermal and electromagnetic parameters of biological tissues,” Version 4.1, Feb 22, 2022.

[58] S. Trovarello, O. Afif, A. Di Florio Di Renzo, D. Masotti, M. Tartagni and A. Costanzo, " A Non-Invasive, Machine Learning Assisted Skin-Hydration Microwave Sensor," 2024 54th European Microwave Conference (EuMC), Paris, France, 2024.

[59] Afif, O.; Franceschelli, L.; Iaccheri, E.; Trovarello, S.; Di Florio Di Renzo, A.; Ragni, L.; Costanzo, A.; Tartagni, M. A Versatile, Machine-Learning-Enhanced RF

Spectral Sensor for Developing a Trunk Hydration Monitoring System in Smart Agriculture. *Sensors* 2024, *24*, 6199.

[60] S. Wold, K. Esbensen, and P. Geladi, “Principal component analysis,” Chemometrics and intelligent laboratory systems, vol. 2, no. 1-3, pp. 37–52, 1987.

[61] L. Franceschelli et al., “Non-intrusive microwave technique for direct detection of concrete compressive strength monitoring by multivariate modeling,” Measurement, vol. 206, p. 112332, Jan. 2023.

[62] A. Di Florio Di Renzo et al., "A Stand-Alone Moisture Content Sensor Based on a Loaded Self-Oscillating Antenna," 2024 IEEE/MTT-S International Microwave Symposium - IMS 2024, Washington, DC, USA, 2024, pp. 284-287.

[63] V. Rizzoli, A. Costanzo, D. Masotti, A. Lipparini and F. Mastri, "Computer-aided optimization of nonlinear microwave circuits with the aid of electromagnetic simulation," *IEEE Transactions on Microwave Theory and Techniques*, vol. 52, no. 1, pp. 362-377, Jan. 2004.

[64] A. Costanzo, D. Masotti, M. Fantuzzi and M. Del Prete, "Co-Design Strategies for Energy-Efficient UWB and UHF Wireless Systems," *IEEE Transactions on Microwave Theory and Techniques*, vol. 65, no. 5, pp. 1852-1863, May 2017.

[65] Razafindratsima, S., Sbartaï, Z.M. & Demontoux, F. “Permittivity measurement of wood material over a wide range of moisture content”, *Wood Sci Technol*, 51, 1421–1431 (2017).

[66] V. Rizzoli, A. Costanzo, F. Mastri, C. Cecchetti, “Harmonic-balance optimization of microwave oscillators for electrical performance, steady-state stability, and near-carrier phase noise,” *(1994) IEEE MTT-S IMS*, pp. 1401 – 1404, 1994.

[67] V. Rizzoli, D. Masotti and A. Costanzo, "Behavioural Models of Injection-Locked Self-Oscillating Microstrip Antennas for Multimedial Communications Systems," *2003 33rd European Microwave Conference*, Munich, Germany, 2003, pp. 499-502, 2003.

[68] Dietsch, P., Franke, S., Franke, B. *et al.* Methods to determine wood moisture content and their applicability in monitoring concepts. *J Civil Struct Health Monit* **5**, 115–127 (2015).

[69] G. Paolini, E. Fazzini, S. Trovarello, D. Amato, D. Masotti and A. Costanzo, "An Innovative Multi-Port LoRa-Based Wireless Node for Railway Signaling and Positioning," in IEEE Journal of Radio Frequency Identification, vol. 8, pp. 618-626, 2024.

[70] G. Paolini, E. Fazzini, S. Trovarello, D. Amato, D. Masotti, and A. Costanzo, "A 2.4 GHz Modular Antenna System for Train Integrity and Localization Purposes," in *IEEE 13th RFID-TA*, Aveiro, Portugal, 2023, pp. 221-224.

[71] G. Battistini, G. Paolini, D. Masotti and A. Costanzo, "Wearable Coplanar-Fed 2.45 GHz-Rectenna on a Flexible 3D-Printable Low-Cost Substrate," 2022 52nd European Microwave Conference (EuMC), Milan, Italy, 2022, pp. 72-75.

[72] X.-Y. Dong, H.-Y. Chen, and D.-H. Guo, "Microwave and Millimeter-Wave Attenuation in Sand and Dust Storms," *IEEE Antennas Wireless Propag. Lett.*, vol. 10, pp. 469-471, May 2011.

[73] A. M. Semmling et al., "Sea-Ice Permittivity Derived From GNSS Reflection Profiles: Results of the MOSAiC Expedition," *IEEE Geosci. Remote Sens. Mag.*, vol. 60, Art no. 4302416, pp. 1-16, 2022.